High Harmonic Generation and Attosecond Light Pulses

An introduction for newcomers

THIERRY RUCHON

thierry.ruchon@cea.fr
http://iramis.cea.fr/LIDYL/Pisp/thierry.ruchon/

FOREWORD

This lecture is issued from courses given at Institut d'Optique Graduate School in Palaiseau (France). It was initially directed towards Master students, and served as a support during the slides-based lecture. However, I also posted it on the web, mainly to please funding agencies which value this kind of dissemination action. After a few years, I got surprised to be approached, during laboratory visits or conferences, by a few persons who had found it, read it, and were asking questions. Indeed this lecture was ranking high in google search for attosecond science. I got also ashamed as the first version had been quickly and dirtily put together for a local use, with plenty of errors that I was usually correcting during the lecture. However, this repeated experience made me realized that an introduction for newcomers was missing in the field. Excellent reviews, numerous PhD dissertations, advanced tutorials treating many aspects in depth all exist. But for a person arriving in the lab, as an intern, PhD, or PostDoc moving out from another research field, a very basic tutorial was not available. I finally decided to turn the initial document into a more polished one, and you have the result in hand.

This foreword is also an opportunity to state that the approach is deliberately over-simplified. Refinements are left to the other sources listed above. However, I have the ambition to not write false statements either. So please, if you find errors, or have comments, I will be happy to consider them carefully to improve this document. And if you find this lecture useful, I will be happy to hear from you as well!

Many chapters are missing: HHG in solids or liquids, applications for measuring photoionization time delays or charge transfer in molecules, band structure dynamics in solids... Plenty of them would probably be equally useful. But I will probably never write them. If you want them as well, you should urge people who know the topic to write them down!

Finally, I would like to acknowledge together the first readers of this lecture and recent errors hunters from my laboratory, who all participated to improve it: Antoine Camper, Romain Géneaux, Lou Barreau, Aura-Ines Gonzalez-Angarita, Céline Chappuis, Christiana Alexandridi, Dominique Platzer, Alice Autuori, Margarita Turconi, David Bresteau, Martin Luttmann, Mekha Vimal ...

CONTENTS

SUMMARY OF THE LECTURE

1 attosecond (1 as) = 10^{-18}

.

- By focusing an intense laser pulse, usually with femtosecond duration, in a gas target, one may observe the generation of a discrete spectrum of high harmonics of the laser. It was first observed in Chicago and Saclay in 1987/1988 (with picosecond laser pulses).
- It is an extremely nonlinear laser-matter interaction process. Like for any non linear optical process, both the individual response of atoms and phase matching play crucial roles.
- The radiation may be shaped to form light pulses with attosecond duration.
- One can measure the temporal profile of the pulses since 2001. The two first measurement methods were called RABBITT and Streaking (also called FROG-CRAB).
- Attosecond pulses may be used in pump-probe experiments to resolve electronic dynamics. However, to date, most of the applications only put at play one attosecond pulse, the second being a left over of the driving femtosecond laser.

CHAPTER 1

ATTOSECOND LONG LIGHT PULSES: WHAT FOR? WHAT IS NEEDED?

1.1 Which systems may show attosecond dynamics?

The definition of multiples and submultiples of a given unit, is only useful if it is adapted to a physical system. For instance, whilst meter are adapted to human sizes, light-years are adapted to astronomical distances and nanometers to atomic/molecular sizes. When it comes to time, fraction of seconds, up to years are adapted to human capabilities and perception. However, millisecond (1 ms=10^{-3} s), microsecond (1 μs=10^{-6} s), nanosecond (1 ns=10^{-9} s), picosecond (1 ps=10^{-12} s), femtosecond (1 fs=10^{-15} s), attosecond (1 as=10^{-18} s) and even zeptosecond (1 zs=10^{-21} s) have all been defined. They are all relevant to some specific dynamics. To give a few very coarse examples

- **Milliseconds** are the typical time scale of fluid dynamics, of exchanges in cells, of air vibrations associated to grave sound, of very light mechanical parts. For instance, a mechanical shutter of a camera is opened for shorter than a fraction of a ms. A turbomolecular vacuum pump is typically rotating one turn per millisecond. 1 ms is also the decay time of a regular phosphor screen.

- **Microseconds** are typical time scale of air vibrations associated to acute sound, of access time to electronic memories, of "electronic shutters" of cameras. It is also the time scale of fast camera light flashes. For instance, pictures of bullets exploding an apple, or patterns of droplets raising up after a main drop falls in a

water bucket were taken by E. H. Edgerton who invented a discharge Xenon flash delivering 1 μs long flashes.

- **nanoseconds** is the realm of commutation of electronic junctions, of the cycle time of computers, of the period of electric fields used for communication networks, of the highest trading frequency on stock exchanges.... 200 ns is the decay time of a fast phosphor screen, and a typical scale for long photo-luminescence decays. It is also the typical timescale of rearrangements of proteins parts.

- **picoseconds** time scales are the fastest transient in integrated electronic devices. It is also the typical rotation time scale of reasonably large molecules (few tens of atoms), and of some of their vibrations. The range of a few picosecond, to hundreds of femtoseconds is thus the playground for objects not larger than reasonably sized molecules (few tens of atoms).

- **femtoseconds** is the time scale of atomic movements in molecules. For instance, the fundamental mode of vibration of molecular dihydrogen has a period of 8 fs. Other molecules and other modes fall in the 10 fs/hundreds of femtosecond range. Femtosecond time scale is thus typical of nuclei dynamics, i.e. fundamental chemistry.

As apparent from the list above, the lighter the elements the faster the dynamics. It goes all the way to the next step:

- **Attoseconds** is the time scale of the most elementary electronic dynamics in atoms, molecules, but also solid state. Indeed, in the very first atomic model of Bohr, describing atomic hydrogen as an electron riding an orbit around a proton, the period of the first Bohr orbit is 150 as = 150 10^{-18}s. *"Attophysics"* is thus mainly the investigation of dynamical properties of electron wave packets at attosecond time scale. It should be noted that *"Attochemistry"* is also used to describe the same kind of physics, when the electronic wave packets are part of a rearranging molecule.

- **Zeptoseconds** time scale should be the typical time scale of intra-nucleus dynamics. This still remains a theoretical prospect.

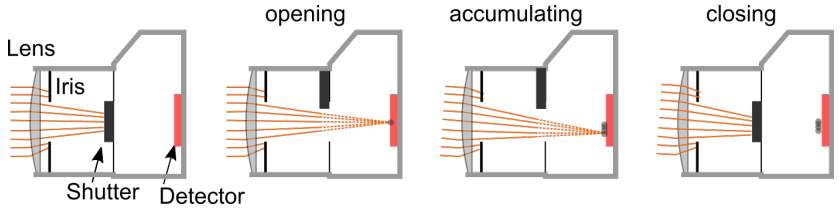

FIGURE 1.1: Sketch of a camera at four instants during the acquisition of a picture.

FIGURE 1.2: Illustration of the importance of the opening time of the shutter of a camera: left: 0.016 s, right: 0.16 s. On the left, details of the waterfalls are apparent (and even rain drops in the foreground), while it is all blurred on the picture on the right.

1.2 Why would we need attosecond light pulses?

1.2.1 Animated photography

To illustrate the need of attosecond long light pulses to record electronic dynamics, let us make a small detour through the history of time resolved imaging. For this, as a prerequisite, the basic elements of a regular camera should be recalled (Fig. 1.1). A minimal camera is made of a focusing element, forming the image of the scene on a detector, e.g. a CCD or CMOS sensor. In between, an iris and a shutter are mounted. The iris is here to regulate the amount of light impinging on the sensor and/or the depth of field of the image. It is of little interest in this introduction to attosecond physics. In regular cameras, the shutter is a mechanical "curtain" that gets lifted when the trigger is pressed, at t_0. It is lowered at t_0 plus the exposure time (t_1). During this time interval, light from the scene impinges on the detector. If an element of the scene evolves during the opening time interval, several pixels will receive light from this single element and it will appear blurred (Fig. 1.2). Recording fast movements thus require i) a shutter opening interval adapted to its time scale, and ii) a sensitive enough detector to record enough light during the short opening time.

It is precisely progress in the sensitivity of photographic plates that allowed the first dynamics to be imaged. They are usually attributed to Eadweard Muybridge who, in 1878, solved a long lasting controversy. The question was "do galloping horses have the four feet off the ground when they are extending their legs". This was widely represented

FIGURE 1.3: Illustration of the making of a movie: pictures taken every half second. "Storm at Pointe des poulains", Belle-Ile-En-Mer, Brittany, France. Rfaire

in classical paintings but debated. For instance, another pioneer of scientific photography, Etienne-Jules Marey was convinced of the contrary, as he stated it in his book from 1872 “La machine animale”. In 1878, supported by a rich horse owner, former gover-

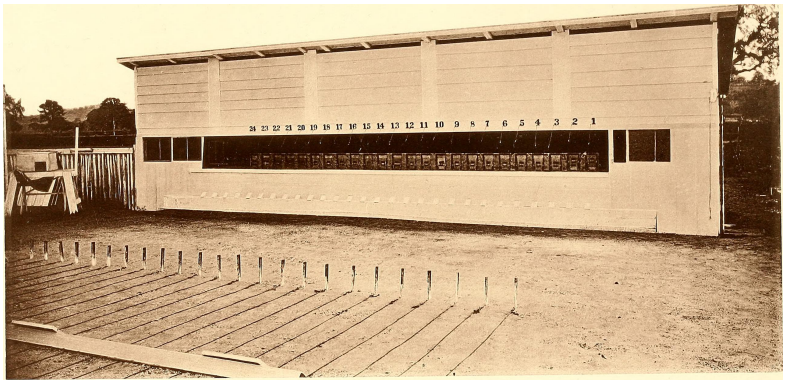

FIGURE 1.4: (left) Arrangement of the cameras used to record so called “instantaneous images” of a galloping horse, by E. Muybridge. The series of cameras are the numbered wooden boxes in the hutch in the back. The track is on the foreground, with the series of wires triggering the cameras holding on the series of posts in the ground. From the book “Horse in motion as shown by instantaneous photography with a study on animal mechanics”, by J. D. B. Stillman (Boston, 1882).

nor of California, Muybridge could invest in a series of 24 cameras that were regularly positioned along a track on which a horse could gallop. The shutters of the cameras were triggered by a series of wires, that the horse would progressively break, giving 24 pictures at different instants (Fig. 1.4). The experiment was made possible due to progress in the sensitivity of silver plates, allowing short enough exposure time. Putting 16 pictures in a sequence gives the first “movie” of a dynamics (Figs. 1.5 & 1.6). Many details of this fascinating story can be found on the internet, including a reconstitution of the experiment (http://www.grumbach-photography.fr/post-la-chronophotographie/ in French, https://timeline.com/see-how-eadweard-muybridge-stopped-time, but many others exist). With the progress of photographic films, and today of CMOS and CCD sensors, the limiting factor became the speed at which the shutter can be opened and closed (Fig. 1.3). Currently, due to their inherent weight, a limit of a fraction of a millisecond may be achieved. To get below, electronic gating of the detector should be used. Or alternatively, a stroboscopic approach.

1.2.2 Stroboscopy

When shutters get too slow to “freeze” the movement to be captured, a solution is to place the scene in the dark, leave the shutter opened and flash very short bursts of light at given times. The scene sends light back to the camera only during a time lapse of the order of the light burst duration. Progress in electronics in the 30’s-50’s allowed H. E. Edgerton to get flashes down to 10μs, recording a series of impressive and popular

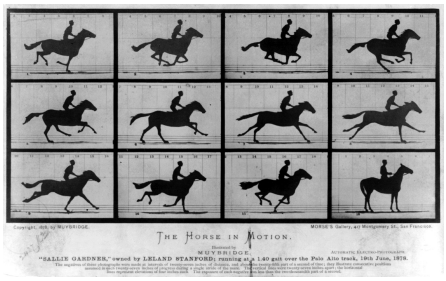

FIGURE 1.5: Series of pictures of Sally Gardner galloping, taken by E. Muybridge. The shutter opening time is 1/2000 s, and pictures are approximately taken at time intervals of 1/25 s.

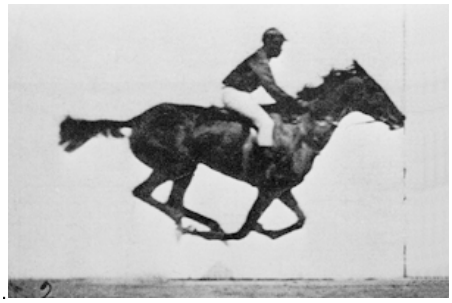

FIGURE 1.6: Reconstitution of the movie as an animated gif (playing in some popular pdf viewers).

photographs (Fig. 1.7). To record the dynamics, a series of flashes, shortly spaced in

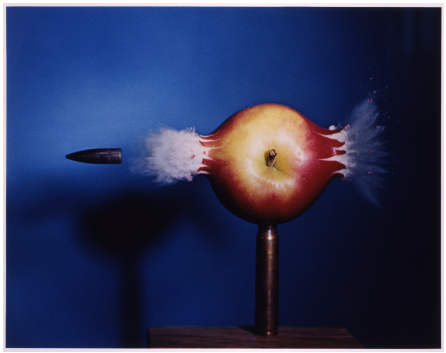

FIGURE 1.7: Harold E. Edgerton, Bullet through Apple, 1964, printed 1984, dye transfer print, Smithsonian American Art Museum, Gift of Mr. and Mrs. Richard F. Young, 1991.89.14. Data Source: Smithsonian American Art Museum

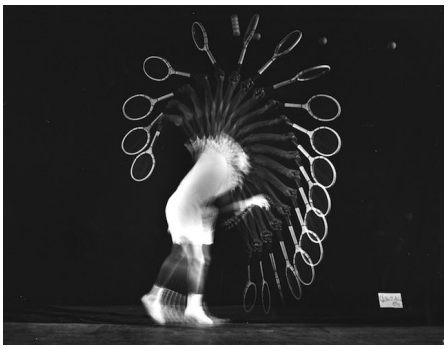

FIGURE 1.8: Harold E. Edgerton, Reference to be given.

time are needed, as illustrated in Fig. 1.8. The fastest movements that can be resolved now depend on the time lapse between two flashes, which cannot be made so short. Indeed, flashes need a discharge of a capacitor that inherently takes time to charge, or a series of synchronized capacitors and flashes. However, if the phenomenon is not reproducible at will, it remains the most efficient time resolving method.

1.2.3 From the stroboscope to pump-probe records

In physics and chemistry, processes under investigation can often be triggered at will, through a specific knob. To be illustrative, let us consider the experiment of the bullet exploding an apple displayed in Fig. 1.7. The camera was triggered after shooting the bullet at a time t_0. If we have a series of identical apples and a gun shooting bullets on demand, we can then replace the apple by one of its twins, shoot a new bullet, and take a new picture at $t_0 + \delta t$, and continue with the series of apples and bullets. By the end of the day, we would have a series of pictures forming the movie of an exploding apple. This is the principle of pump-probe experiments. In this example the pump is the action of triggering the bullet, while the probe is the triggering of the light flash. It is illustrated in a more scientific context for instance at www.toutestquantique.fr(in English – Misleading address). There, the trigger, which launches the dynamics is a first light pulse, while the probe is a second light pulse. The time resolution of the movie will be of the order of the longer out of the pump and probe pulse durations. In summary, to implement a pump-probe scheme, one needs to have

1. a reproducible phenomenon that can be triggered at will by a first light pulse
2. a second short light pulse that allows to "freeze" the dynamics at an instant later.

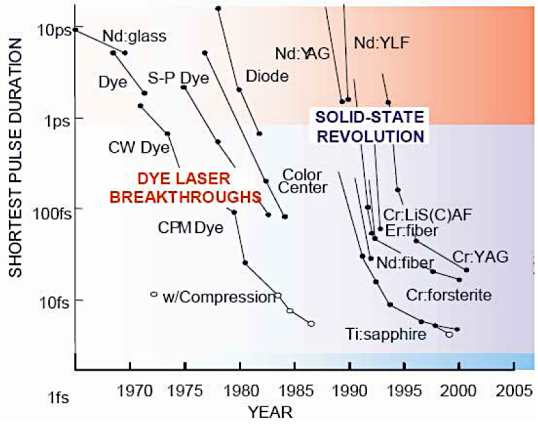

FIGURE 1.9: Record duration of light pulses from lasers, and associated technology vs. years. From Eichenholz et al. [2006].

It took only a few years from the invention of the laser (1960) to the demonstration of picosecond lasers (Nd:glass, mid 60's), and another 10 years to reach the femtosecond level (dye lasers, mid 70's) (Fig. 1.9). With the advent of femtosecond lasers, the atomic dynamics could be probed with such scheme, launching the blossoming field of "femtochemistry". Naturally, the advent of attosecond long pulses is a promise of monitoring electronic dynamics. But breaking the "femtosecond barrier" and getting to the attosecond regime took another 25 years, with the first observation of attosecond light pulses in 2001, simultaneously in Saclay/Palaiseau and Garching. Why it was so difficult will become apparent in this lecture.

1.3 What does it take to make attosecond light pulses?

1.3.1 Anatomy of a short pulse

Mathematical interlude that can be skipped for a first reading – The grayed boxes show the most important results.

This paragraph is freely inspired by the excellent lecture on non linear optics of Manuel Joffre, École Polytechnique (Palaiseau, France)(Link here).

Analytical representation of the field.

We consider the real valued electric field of a light pulse, $E(t)$. The first question is to define an amplitude and a phase for this real-valued field. As we will see towards the end of this subsection, when dealing with fields showing some complexity, it is not always so obvious; making useful the procedure that we detail here. It is also a good opportunity to precisely define important notions for short pulse optics, such as group delay dispersion, chirp, time-frequency bandwidths products.... To get started, we move to the Fourier domain and define

$$\tilde{E}(\omega) = \mathcal{F}\left[E(t)\right](\omega).$$

Since the field is real we have

$$\tilde{E}^*(\omega) = \tilde{E}(-\omega), \tag{1.1}$$

which is a basic property of the Fourier transform. It is therefore redundant to keep all the definition of the field. For instance, the positive side of the angular frequency axis is sufficient. We use the Heaviside function $\Theta(\omega)$, which is 0 on the left half axis and 1 elsewhere, and define

$$\tilde{\mathcal{E}}(\omega) = 2\Theta(\omega)\tilde{E}(\omega) \tag{1.2}$$

The analytical representation of the real-value field $E(t)$ is then defined as (cf. Fig.1.10)

$$\mathcal{E}(t) = \mathcal{F}^{-1}\left[\tilde{\mathcal{E}}(\omega)\right](t). \tag{1.3}$$

It is also called the complex amplitude since the initial field, $E(t)$, is nothing but its real part:

$$\begin{aligned}
\mathcal{R}(\mathcal{E}(t)) &= \frac{\mathcal{E}(t) + \mathcal{E}^*(t)}{2} && (1.4)\\
&= \frac{1}{2}\mathcal{F}^{-1}\left[\tilde{\mathcal{E}}(\omega)\right](t) + \frac{1}{2}\mathcal{F}^{-1}\left[\tilde{\mathcal{E}}^*(-\omega)\right](t) && (1.5)\\
&= \frac{1}{2}\mathcal{F}^{-1}\left[\tilde{\mathcal{E}}(\omega) + \tilde{\mathcal{E}}^*(-\omega)\right](t) && (1.6)\\
&= \mathcal{F}^{-1}\left[\Theta(\omega)\tilde{E}(\omega) + \Theta(-\omega)\tilde{E}^*(-\omega)\right](t) && (1.7)\\
&= \mathcal{F}^{-1}\left[\Theta(\omega)\tilde{E}(\omega) + \Theta(-\omega)\tilde{E}(\omega)\right](t) && (1.8)\\
&= \mathcal{F}^{-1}\left[\tilde{E}(\omega)\right](t) = E(t) && (1.9)
\end{aligned}$$

Finally, we define the

$$\text{Temporal intensity } I(t) = |\mathcal{E}(t)|^2 \tag{1.10}$$
$$\text{Temporal phase } \phi(t) = arg(\mathcal{E}(t)) \tag{1.11}$$
.

For instance, we can consider a light pulse with a central angular frequency ω_0 and a gaussian amplitude $A(t) = e^{-\sigma^2 t^2}$. We denote "$\otimes$" the convolution operation. The real-valued electric field reads

$$E(t) = A(t) \cdot \cos(\omega_0 t) = \frac{A(t)}{2} \cdot \left(e^{i\omega_0 t} + e^{-i\omega_0 t}\right)$$

and its Fourier transform

$$\tilde{E}(\omega) = \frac{1}{2}\tilde{A}(\omega) \otimes \left(\delta(\omega - \omega_0) + \delta(\omega + \omega_0)\right) \tag{1.12}$$
$$= \frac{1}{2}\left(\tilde{A}(\omega - \omega_0) + \tilde{A}(\omega + \omega_0)\right) \tag{1.13}$$

We then get the associated analytical representation of the field as (the integration limits take into account the Heaviside function)

$$\mathcal{E}(t) = \frac{1}{\sqrt{2\pi}} \int_0^{+\infty} d\omega \left(\tilde{A}(\omega - \omega_0) + \tilde{A}(\omega + \omega_0)\right) e^{i\omega t} \tag{1.14}$$

The Fourier transform of the Gaussian reads

$$\tilde{A}(\omega) = \frac{1}{\sqrt{2}\sigma} e^{-\frac{\omega^2}{4\sigma^2}}. \tag{1.15}$$

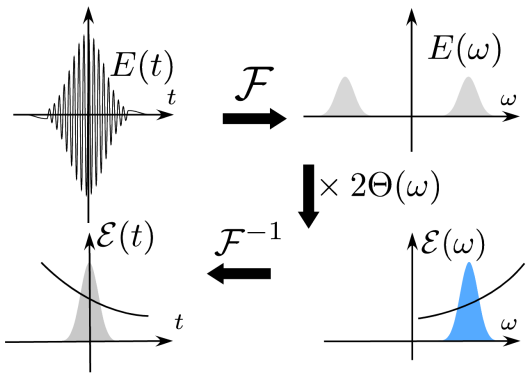

FIGURE 1.10: Definition of the analytical representation of a real valued field. Top left: Electric field of the pulse vs. time. Top right: amplitude of its complex Fourier transform (phase not represented). Bottom right: selection of the positive half of the spectrum, amplitude in blue, spectral phase as a line. Bottom left: associated analytical signal vs. time; amplitude in grey shaded area, phase as a line.

We consider its width to be small compared to ω_0. In that case, the second integrand remains very small on the positive side of the ω axis. Also, the first integrand would not contribute on the negative part of the ω axis, and the lower integration limit can be extended to $-\infty$. We thus get the analytical representation as

$$\mathcal{E}(t) = A(t) \cdot e^{i\omega_0 t} \tag{1.16}$$

and the temporal intensity and phase read

$$I(t) = e^{-2\sigma^2 t^2} \tag{1.17}$$

$$\phi(t) = \omega_0 t \tag{1.18}$$

which is the expected result. However, if A(t) shows some complex features, such as for instance, a very irregular envelope, a mixture of two central frequencies, or if its spectrum extends over a very large range covering the null frequency, the above approximation is not valid and defining this amplitude and phase would be nothing like obvious. In such a case, this mathematical procedure very useful.

Arrival time, central frequency, duration, spectral width.

We now define for this pulse its:

$$\text{Arrival time} \qquad t_0 = \langle t \rangle = \int t|\mathcal{E}(t)|^2 dt, \tag{1.19}$$

$$\text{Central frequency} \qquad \omega_0 = \langle \omega \rangle = \int \omega|\mathcal{E}(\omega)|^2 dt\omega, \tag{1.20}$$

$$\text{Duration} \qquad \Delta t = \sqrt{\langle t^2 \rangle - \langle t \rangle^2} \tag{1.21}$$

$$\text{Spectral width} \qquad \Delta\omega = \sqrt{\langle \omega^2 \rangle - \langle \omega \rangle^2}. \tag{1.22}$$

The classical properties of the Fourier transform remain valid for the analytical signal and its Fourier transform. In particular, the Parseval-Plancherel theorem for intensity gives the energy per unit surface of the light pulse:

$$\int I(t)dt = \int |\mathcal{E}(t)|^2 dt = \int |\mathcal{E}(\omega)|^2 d\omega = \int I(\omega)d\omega. \tag{1.23}$$

In other words, the integration over time of the "temporal intensity", $I(t)$, or over the angular frequencies of the "spectral intensity", $I(\omega)$, give the same result, which is the spatial density of energy in the pulse. Integrating over the transverse profile would give the energy in the pulse.

The Cauchy-Schwarz inequality, adapted to this case gives:

$$\Delta t \Delta\omega \geq \frac{1}{2} \tag{1.24}$$

The demonstration is not very complicated but a bit lengthy . It is given in Appendix A.4 of the Non linear optics lecture by M. Joffre (in French but only equations are written in this paragraph) or at Cauchy-Schwarz inequality on Wikipedia. Note that for a Gaussian pulse, we have exactly the equality $\Delta t \Delta\omega = \frac{1}{2}$. This equality is given for the **variances** of the time and angular frequencies. If we use the more common FWHM, we have, for a Gaussian pulse

$$\Delta t_{\mathrm{FWHM}} \Delta\omega_{\mathrm{FWHM}} = 4 \ln 2 \simeq 2.77 \qquad \text{for a Gaussian pulse} \tag{1.25}$$

Influence of the temporal phase on the temporal profile.

The temporal phase, and its counterpart the spectral phase of a light pulse play a crucial role in the construction of the temporal profile of a pulse. To highlight this point, we may use the Parseval theorem:

$$\int_{-\infty}^{\infty} dt f(t) g^*(t) = \int_{-\infty}^{\infty} d\omega \tilde{f}(\omega) \tilde{g}^*(\omega) \tag{1.26}$$

and the following property of the Fourier transform:

$$\mathcal{F}[t^n f(t)] = i^n \frac{d^n \tilde{f}(\omega)}{d\omega^n} \tag{1.27}$$

which is demonstrated by integration by parts. If we apply it to the arrival time of the pulse, we get:

$$t_0 = \langle t \rangle = \int t |\mathcal{E}(t)|^2 dt = i \int \mathcal{E}^*(\omega) \frac{d\mathcal{E}(\omega)}{d\omega} \frac{d\omega}{2\pi} \tag{1.28}$$

Introducing the phase and the amplitude of the analytical representation in the spectral domain

$$\mathcal{E}(\omega) = |\mathcal{E}(\omega)| e^{i\varphi(\omega)} \tag{1.29}$$

we get

$$\frac{d\mathcal{E}(\omega)}{d\omega} = \left(\frac{d|\mathcal{E}(\omega)|}{d\omega} + i|\mathcal{E}(\omega)| \frac{d\varphi(\omega)}{d\omega} \right) e^{i\varphi(\omega)}.$$

and

$$\begin{aligned} t_0 &= i \int |\mathcal{E}(\omega)| \frac{d|\mathcal{E}(\omega)|}{d\omega} \frac{d\omega}{2\pi} - \int \frac{d\varphi(\omega)}{d\omega} |\mathcal{E}(\omega)|^2 \frac{d\omega}{2\pi} \\ &= i[|\mathcal{E}(\omega)|^2]_{-\infty}^{\infty} - \left\langle \frac{d\varphi}{d\omega} \right\rangle \\ &= - \left\langle \frac{d\varphi}{d\omega} \right\rangle \end{aligned} \tag{1.30}$$

We define the

Group delay	$\tau_g(\omega) \hat{=} -\dfrac{\partial\varphi}{\partial\omega}$,
Arrival time of the pulse:	$\langle t\rangle = \left\langle \tau_g(\omega)\right\rangle$,
Group Delay Dispersion:	$\text{GDD} \hat{=} \dfrac{\partial\tau_g}{\partial\omega} = \dfrac{\partial^2\varphi}{\partial\omega^2}$

For the pulse duration we find

$$\begin{aligned}\langle t^2\rangle &= \int t^2|\mathcal{E}(t)|^2dt \\ &= -\int \left|\frac{d\mathcal{E}(\omega)}{d\omega}\right|^2 \frac{d\omega}{2\pi} \\ &= -\int \left(\frac{d\,|\mathcal{E}(\omega)|}{d\omega}\right)^2 \frac{d\omega}{2\pi} + \int \left(\frac{d\varphi(\omega)}{d\omega}\right)^2 |\mathcal{E}(\omega)|^2 \frac{d\omega}{2\pi}\end{aligned}$$

Introducing the case in which the spectral phase is zero $\langle t^2\rangle_{\varphi=0}$, which correspond to the first term on the right hand side; and the mean of the square of the group delays $\langle \tau_g(\omega)^2\rangle$, we get

$$\langle t^2\rangle = \langle t^2\rangle_{\varphi=0} + \langle \tau_g(\omega)^2\rangle.$$

Using the definitions in Eq. (1.21), and $\langle t\rangle_{\varphi=0} = 0$, we get

$$\Delta t^2 = \langle t^2\rangle - \langle t\rangle^2 \tag{1.31}$$

$$= \langle t^2\rangle_{\varphi=0} - \langle t\rangle^2_{\varphi=0} + \langle \tau_g(\omega)^2\rangle - \langle \tau_g(\omega)\rangle^2 \tag{1.32}$$

$$= \Delta t^2_{\varphi=0} + \Delta\tau_g^2 \tag{1.33}$$

No phase can make the pulse shorter than the pulse obtained when the spectral phase is zero. If the group delay is constant, i.e. the spectral phase is linear with the frequency, it can be verified that $\Delta\tau_g^2 = 0$ (Non linear optics lecture by M. Joffre). This is also apparent graphically in Fig. 1.11, where the two pulses with a linear phase difference are just offset temporally from one another, hence sharing the same temporal width. We thus come to the important conclusion that

A pulse is all the shorter as its spectral phase does not show any quadratic or higher order non zero terms in its Taylor expansion. If such a term exists, it correspond to unperfectly synchronized spectral components. This is called Group Delay Dispersion (GDD) in the spectral domain. It corresponds to a chirp in the temporal domain, i.e. a frequency that changes with time like a bird song.

This is the reason why much care is taken to control the spectral phase of femtosecond lasers. To illustrate this point, a few examples of light pulses with identical spectra but different spectral phases are displayed in Fig. 1.11, together with their temporal

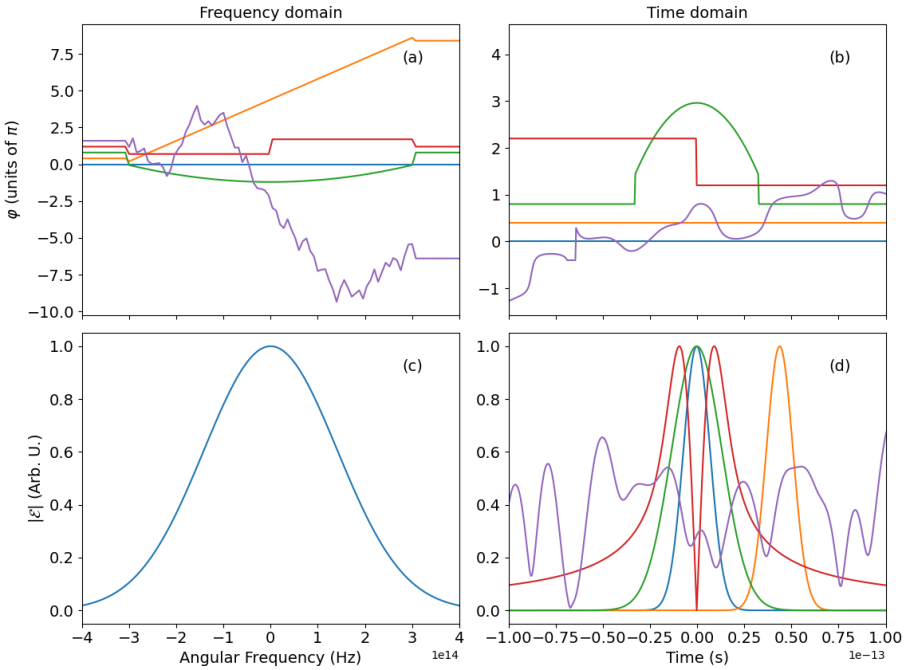

FIGURE 1.11: Fourier transforms examples. The same amplitude is used in the frequency domain, while five different phases are defined (displayed in the top left panels). The corresponding amplitude and phase of the Fourier transforms are displayed in the right column against time.

profile. In particular, for a random phase in the spectral domain, no well defined light pulse is obtained. However, as detailed in the next paragraph, this spectral phase can be partially handled through propagation in matter.

Managing the pulse temporal profile through propagation in matter

The group delay can be partly controlled by reflexion off specific materials, or propagation in matter to approach the shorter accessible duration given a certain spectrum. To keep things simple, we may consider the linear propagation of a light pulse in a dispersive medium (in transmission, e.g. a foil, or reflexion, i.e. mirror), with a wave vector $k(\omega) = \frac{2\pi}{\lambda} n(\omega)$ along axis z; where $n(\omega)$ is the optical index. By linear propagation, we mean that each frequency component is propagating with its own refractive index, independently of others. At the exit of the medium, at abscissa z, the complex field reads

$$\tilde{\mathcal{E}}(z,\omega) = \tilde{\mathcal{E}}(0,\omega)e^{ik(\omega)z} = |\tilde{\mathcal{E}}(0,\omega)|e^{i\varphi(0,\omega)+ik(\omega)z}$$

We thus have

$$\begin{aligned}\varphi(z,\omega) &= \varphi(0,\omega) + k(\omega)z \\ &\simeq \varphi(0,\omega_0) + \frac{dk(\omega)}{d\omega}\left(\omega-\omega_0\right)\cdot z + \frac{1}{2}\frac{d^2k(\omega)}{d\omega^2}\left(\omega-\omega_0\right)^2\cdot z + \dots \end{aligned} \tag{1.34}$$

where we have indicated the Taylor expansion of the phase. The arrival time of the ω component reads

$$\tau_g(z,\omega) = \frac{\partial\varphi(z,\omega)}{\partial\omega} = \tau_g(0,\omega) + \frac{dk}{d\omega}z \tag{1.35}$$

It follows that the "arrival time" of the pulse reads

$$\langle t\rangle_z = \langle\tau_g(z,\omega)\rangle_\omega = \langle t\rangle_{z=0} + \langle\frac{dk}{d\omega}\rangle z \tag{1.36}$$

If $\frac{dk}{d\omega} = 1/v_g(\omega)$ is a constant, called "Group velocity", the pulse envelope propagates at speed v_g. In general $v_g(\omega)$ will be frequency dependent, giving a "Group Velocity Dispersion" (GVD).

Getting back to the duration of the pulse (Eq. (1.33)), we may write

$$\Delta t^2(z) = \Delta t^2_{\varphi=0} + \Delta\tau_g^2(z) \tag{1.37}$$

$$= \Delta t^2_{\varphi=0} + \left\langle\left(\tau_g(z,\omega) - \left\langle\tau_g(z,\omega)\right\rangle\right)^2\right\rangle \tag{1.38}$$

$$= \Delta t^2_{\varphi=0} + \left\langle\left(\tau_g(0,\omega) - \left\langle\tau_g(0,\omega)\right\rangle + \left[\frac{dk}{d\omega} - \left\langle\frac{dk}{d\omega}\right\rangle\right]\cdot z\right)^2\right\rangle \tag{1.39}$$

As it propagates, the spectral components change their synchronization due to the term in the largest angular brackets in Eq. 1.34. In $z = 0$, the pulse has a certain duration (determined by $\tau_g(0,\omega) - \left\langle\tau_g(0,\omega)\right\rangle$) which gets progressively modified by $\left[\frac{dk}{d\omega} - \left\langle\frac{dk}{d\omega}\right\rangle\right]\cdot z$. Depending on the relative signs of these two terms, it may compensate one another or add up, either compressing temporally the pulse or spreading it in time.

Upon manipulations of this formula and using Eq. (1.34), it can be shown that the duration of the pulse scales as [Non linear optics lecture by M. Joffre]

$$\Delta t(z) = \sqrt{\Delta t_{\varphi=0}^2 + \left(\frac{d^2k}{d\omega^2}\right)^2 \cdot \Delta\omega^2 \cdot z^2}, \tag{1.40}$$

$$= \Delta t_{\varphi=0}\sqrt{1 + \left(\frac{d^2k}{d\omega^2} \cdot \frac{\Delta\omega}{\Delta t_{\varphi=0}} \cdot z\right)^2}, \tag{1.41}$$

where $\Delta\omega$ is the spectral width of the pulse (Eq. (1.22)). To be specific, let us consider gaussian pulses, for which $\Delta t_{\varphi=0}\Delta\omega = 1/2$. Formula (1.21) reads

$$\Delta t(z) = \Delta t_{\varphi=0}\sqrt{1 + \left(\frac{d^2k}{d\omega^2} \cdot \frac{z}{2\Delta t_{\varphi=0}^2}\right)^2} \tag{1.42}$$

$$\tau(z) = \tau_{\varphi=0}\sqrt{1 + \left(4\ln 2\frac{d^2k}{d\omega^2} \cdot \frac{z}{\tau_{\varphi=0}^2}\right)^2} \tag{1.43}$$

$$\tag{1.44}$$

where we introduced the FWHM of a Gaussian pulse $\tau = 2\sqrt{2\ln 2}\Delta t$.

At the lasing wavelength of the popular Ti:Sapphire laser, around λ=800 nm, all materials add a positive dispersion, e.g. $\frac{d^2k}{d\omega^2}$ =+20 fs^2/m for air, +36 fs^2/mm for fused silica. Pulses with respective durations of 30 fs, 20 fs, 10 fs and 5 fs will get out of a 1 mm thick plate of fused silica with durations of 30.2 fs, 20.6 fs, 14.1 fs and 20.6 fs. We note here the great difficulty to manipulate very short pulses. In general, with this kind of ultrashort light pulses, a precompensation has to be set, to reach on target, after focusing, the minimum duration.

As a final word, it should be kept in mind that we have only treated the second order derivative. Higher order dispersion also come into play, especially with ultra short light pulses (see e.g Lukas Gallmann and Ursulla Keller Lectures notes) that will modify the pulse shape as it propagates in a medium.

End of the interlude

1.3.2 Ingredients for an attosecond light pulse

As it will be apparent shortly, attosecond pulses have a central frequency in the Extreme Ultra Violet (XUV) domain, which roughly spans the wavelength range

$$5 \text{ nm} \lesssim \lambda \lesssim 120 \text{ nm}. \tag{1.45}$$

The definition is not uniform among different fields and disciplines. We chose the 120 nm limit because it is the shortest wavelength beyond which no massive material

is transparent. It corresponds to the edge of magnesium fluorure, from which windows and lenses can be manufactured. On the short wavelength side, we chose the K-edge of carbon, lying at about 5 nm. Beyond this limit is the spectral range of soft X-rays. The XUV range thus corresponds to photon energies

$$10\,\mathrm{eV} \lesssim E(eV) = \frac{hc}{e\lambda} \lesssim 250\,\mathrm{eV}, \tag{1.46}$$

with h the Planck constant, c the speed of light in vacuum and e the elementary charge.

From Cauchy-Schwarz inequality (Eq. (1.24)), the temporal and spectral widths are connected. To be specific, let us consider a gaussian light pulse in the temporal domain, whose envelope of the electric field reads $A(t) = A_0 e^{-\sigma^2 t^2}$. Its intensity will be $I(t) = A_0^2 e^{-2\sigma^2 t^2}$, and the Full Width at Half Maximum (FWHM) of the intensity $\Delta t_{\mathrm{FWHM}} = \sqrt{2\ln 2}/\sigma$, while the variance of time reads $\Delta t = 1/2\sigma$. It spectral power will have an envelope given by $I(\omega) \propto e^{-\frac{\omega^2}{2\sigma^2}}$, whose FWHM reads $\Delta\omega_{\mathrm{FWHM}} = 2\sqrt{2\ln 2}\sigma$ and variance $\Delta\omega = \sigma$. We thus have $\Delta t \cdot \Delta\omega = 1/2$, as expected for a Gaussian, and $\Delta t_{\mathrm{FWHM}} \cdot \Delta\omega_{\mathrm{FWHM}} = 4\ln 2$, which can be rewritten

$$\Delta E(eV)_{\mathrm{FWHM}} \Delta t_{\mathrm{FWHM}} \geq 4\ln 2 \cdot \frac{\hbar}{e} = 1.8\ 10^{-15}\mathrm{eV.s} \tag{1.47}$$

For instance, to obtain a gaussian pulse of 100 as FWHM, one needs a spectrum of at least 18 eV FWHM. Depending on the exact form of the pulse, and definition of the widths, these values may be a bit different, but the important conclusions will remain. In particular, the bandwidth of the visible spectrum extends from 400 nm $\lesssim \lambda \lesssim$ 800 nm, corresponding to photon energies from 1.5 eV to 3 eV. The available bandwidth is thus limited to 1.5 eV and visible pulses to about 1 fs. One can find enough spectral room to accommodate attosecond pulses only in the XUV domain or further up in energy.

Conclusion:

To get attosecond pulses one needs

1. An XUV source (Eq. (1.47))
2. A spectrum several tens of eV's wide (Eq. (1.47))
3. A well controlled spectral phase. (Fig. 1.11)

This has very important consequences on practical grounds. In particular, in the XUV range (from its definition), all solid state materials are absorbant, and gases, including air at atmospheric pressure have an absorption length below the millimeter. As a consequence all experiments should be done under vacuum, and no transmissive optics but extremely thin ones may be used. A noticeable exception are metallic foils of a few hundred nanometer thickness, which can, in some spectral ranges, transmit significant amount of XUV light (Fig. 5.5).

CHAPTER 2

HIGH HARMONIC GENERATION IN GASES (HHG): A SINGLE HALF CYCLE OF THE LASER PULSE, A SINGLE ATOM

In the 80's, the shortening of the duration of laser pulses made achievable extremely high intensities on target, in the 10^{14} W/cm^2. It opened the door to the strong field interaction regime: the laser field becomes comparable to the Coulomb field of atoms or molecules. Two phenomena are discovered: Above Threshold Ionization (ATI, P. Agostini et al., 1979, at CEA-Saclay) and High Harmonic Generation (HHG). The first publication is usually attributed to McPherson et al. [1987], who published a graph showing 6 harmonics of a λ=248 nm, picosecond laser installed in Chicago. Soon later, a team led by Anne L'Huillier in CEA-Saclay published a graph showing harmonics of a Nd:YAG, 30 ps, λ=1064 nm laser extending up to 33rd order (Ferray et al. [1988]).

For ATI, a gas target submitted to a strong laser field emits electrons having energy matching an integer number of photons energies. In the second case, photons having energies limited to odd multiples of the energy of the laser photon are emitted. The spectrum can be very large (see Figs. 2.1 & 2.2) in the XUV. Generally, two zones of the spectrum can be distinguished: the low energy side of the spectrum, where the amplitude of the harmonics decreases slightly with the order, which is called **plateau**,

and the high energy side, where the decay is fast, called **the cutoff**[1]. It was quickly realized that this radiation was very promising to make attosecond pulses. However, a question remained unresolved experimentally up to 2001: is the phase controlled?

Theoretically, from 1992-1993 on, which corresponds to the elaboration of the three-step model of HHG [Kulander et al. [1993]&Corkum [1993]], the prediction was promising. This three-step model is described below, together with an introduction to its quantum version, the "Strong Field Approximation", elaborated by M. Lewenstein and coworkers and published in 1994 [Lewenstein et al. [1994]].

2.1 Three step model

There is a bit of a discussion about the origin of the very popular three-step model, with two almost concomitant publications (Refs. Kulander et al. [1993]; Corkum [1993]), the former being a proceeding of SILAP conference held 8-14 January 1993 in Belgium, the latter a paper submitted on 9th February and published in September 1993. Interestingly, in a different context, another publication is giving very similar insights and was published six years before Kuchiev [1987].

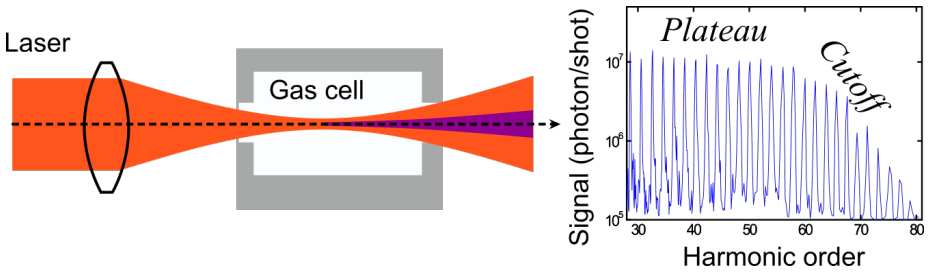

FIGURE 2.1: Sketch of an HHG setup and typical harmonic spectrum. The abscissa is scaled in multiples of the energy of the driving photon (harmonics orders).

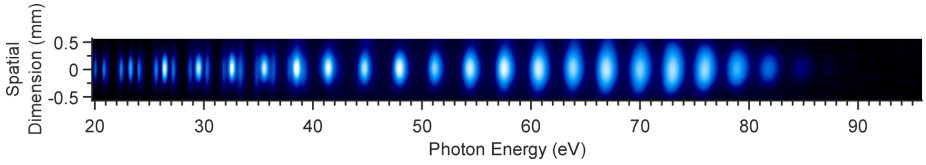

FIGURE 2.2: Typical HHG spectrum recorded on a Ti:Sapphire laser at λ =800 nm, duration of 50 fs, using Neon as a generation gas. The horizontal dimension gives the spectrum, while the vertical one gives the divergence of the harmonics. At the beginning of the spectrum, 2nd order diffraction of the grating of the spectrometer give secondary peaks.

[1] The lower part of the spectrum, i.e harmonics 3, 5…is not represented here, while it is dominant in magnitude. They are generated in the perturbative regime, making successive harmonics of very different magnitude from one to the next. The FWHM of the spectrum, when taking these dominant harmonics into account is too narrow to make attosecond pulses. They should therefore be filtered out.

2.1.1 General description

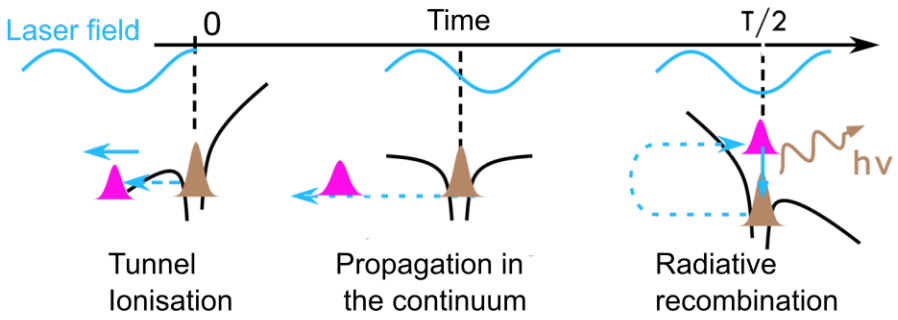

FIGURE 2.3: Three step model of high harmonic generation. T is the period of the laser. Exact timings are discussed later.

An atom is submitted to an extremely intense oscillating laser field, generally with IR wavelength. At the maxima of the field, the Coulomb potential is so distorted that it becomes possible for the most weakly bound electrons, to tunnel out into the continuum. The electronic wave packet emitted is then guided by the field and can, under certain conditions, pass close to the parent ion later, with a high speed. It then has a nonzero probability to recombine with the ion, emitting its kinetic energy in the form of photons. So to summarize, three successive steps:

1. Step 1: Tunnel ionization
2. Step 2: Excursion in the continuum
3. Step 3: Recombination.

In the following, we will successively describe these steps. To make derivations easier, we will use the atomic units that are recalled in Sec. 2.1.2.

2.1.2 Atomic units

Tables 2.1-2.2 are largely copied from Lene Raymond Abdul notes and Vasile Chis notes. The atomic units make the fundamental electron properties all equal to one atomic unit. ($m_e = 1, e = 1, \hbar = h/2\pi = 1, a_0 = 1\ldots$) Other quantities should be multiplied, at the end of the derivation, by the values in Table 2.2 according to their units.

2.1.3 Tunnel ionization

Saturation intensity

We simply model the potential of the ionic core by a coulombic potential, $1/|x|$ (Fig. 2.5). We consider an electron lying on an orbital at energy I_p from the ionization level

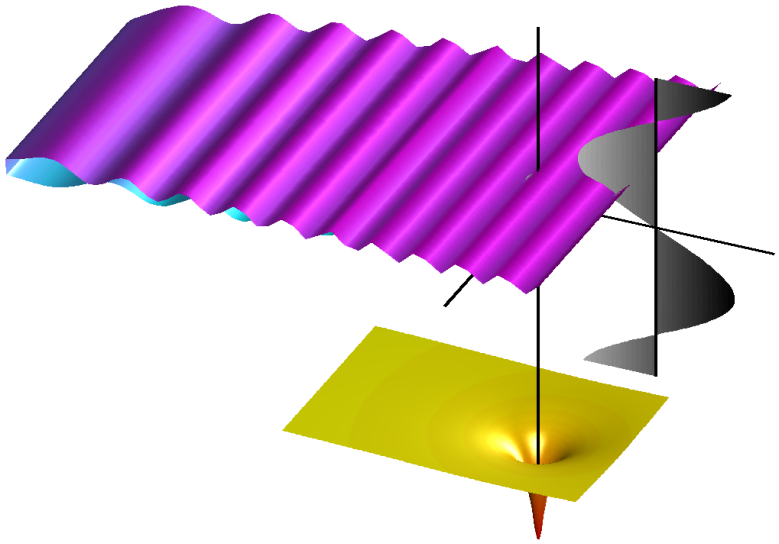

FIGURE 2.4: Animation (playing in some popular pdf viewers), showing the synchronization between the electric field of the laser, and the emission of an electronic wave packet. The periodicity of the wave is linked to its energy. In yellow is the sum of the coulombic potential and of the laser field.

Quantity	Unit	Physical significance	Value in SI-units
Mass	m_e	Electron mass	9.11×10^{-31} kg
Charge	e	Absolute value of electron charge	1.60×10^{-19} C
Angular momentum	$\hbar$	Planck's constant divided by 2π	1.05×10^{-34} Js
Electrostatic constant	$4\pi\epsilon_0$	4π times the permittivity of free space	1.11×10^{-10} Fm^{-1}

TABLE 2.1: Basic quantities for the atomic unit system (from Lene Raymond Abdul notes).

Quantity	Unit	Physical significance	Value in SI-units
Length	$a_0 = \frac{4\pi\epsilon_0\hbar^2}{m_e e^2}$	Bohr radius for atomic hydrogen	5.29×10^{-11} m
Energy	$E_h = \hbar^2/m_e a_0^2$	Twice the ionisation potential of atomic hydrogen	4.36×10^{-18} J
Time	$\tau_0 = \hbar/E_h$	Time required for electron in first Bohr orbit to travel one Bohr radius	2.42×10^{-17} s
Velocity	$v_0 = a_0/\tau_0$	Magnitude of electron velocity in first Bohr orbit	2.19×10^6 ms^{-1}
Angular frequency	$\omega_0 = \frac{v_0}{2\pi a_0}$	Angular frequency of electron in first Bohr orbit	6.58×10^{15} s^{-1}
Electric field	$F_0 = \frac{e}{(4\pi\epsilon_0)a_0^2}$	Strength of the Coulomb field experienced by an electron in the first Bohr orbit of atomic hydrogen	5.14×10^{11} Vm^{-1}

TABLE 2.2: Derived quantities for the atomic unit system (from Lene Raymond Abdul notes).

(I_p stands for Ionization Potential). The laser electric field, $E(t) = E_0 \cos(\omega t)$ is supposed to be homogeneous on the relevant size scales around the atom. The associated potential reads $E_0 \cdot x$ at the time origin. The total electric potential seen by the electron is thus

$$V(x) = -\frac{1}{|x|} + E_0 \cdot x \tag{2.1}$$

In Fig. 2.5 we note that, when the electric field is zero, the electron cannot escape the ionic core. On the contrary, when the laser E-field is raising up, a barrier is formed,

whose height decreases as the laser E-field increases. The value of the maximum of the barrier is denoted $V(x_m)$ and is obtained at abcissa x_m. If the laser E-field is so high that $V(x_m) < I_p$ the electron can directly escape the potential and the atom gets ionized. If $I_p < V(x_m) < 0$. the electron should not classically escape the potential of the ionic core. However, in the quantum world, it may still tunnel ionize out of this barrier, the rate of tunneling depending on the width of the barrier, and its height.

We consider a case in which the barrier is lowered on the x > 0 side ($E_0 < 0$). We look for the coordinated $(x_m, V(x_m))$. Deriving Eq. (2.1) we get

$$\frac{\partial V}{\partial x} = \frac{1}{x^2} + E_0 \tag{2.2}$$

which gets null at [2]:

$$x_m = 1/\sqrt{-E_0} \tag{2.3}$$

$$V(x_m) = -2\sqrt{-E_0} \tag{2.4}$$

We define the saturation field E_{sat} as the laser field above which, at some time, the barrier is fully open. In that instance, the height of the barrier equals the ionization potential, and we get

$$V(x_m) = I_p \;\Leftrightarrow\; E_0 \hat{=} E_{sat} = \frac{I_p^2}{4}. \tag{2.5}$$

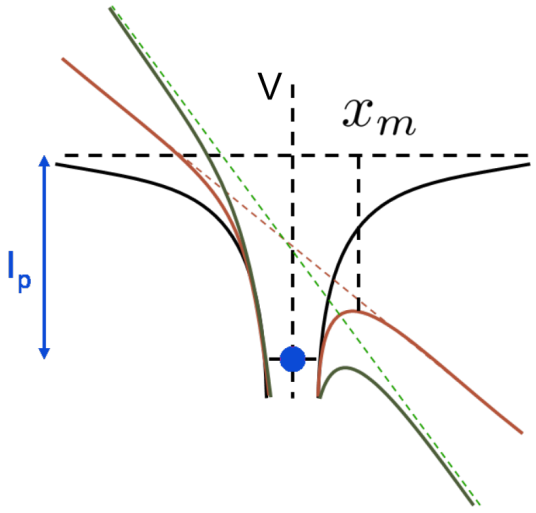

FIGURE 2.5: Sketch of a field driven ionization. We consider a 1D atom with a single active electron. The black line represents the potential of the ionic core, experienced by the electron when the laser is off. The dark green curve corresponds to a suppression of the ionic barrier by the electric potential of the laser. The orange curve is the intermediate situation, in which tunnel ionization is possible.

[2] watch out in getting the second equation that due to its sign $E_0 = -(\sqrt{-E_0})^2$

	I_p	I_{sat}	E_{sat}
He	24.58 eV	14.6×10^{14} W/cm^2	10.49×10^{10} V/m
Ne	21.55 eV	8.62×10^{14} W/cm^2	8.06×10^{10} V/m
Ar	15.75 eV	2.46×10^{14} W/cm^2	4.31×10^{10} V/m
Kr	14.00 eV	1.53×10^{14} W/cm^2	3.40×10^{10} V/m
Xe	12.13 eV	0.87×10^{14} W/cm^2	2.55×10^{10} V/m

TABLE 2.3: Ionization potential and saturation intensities of noble gases

In practice, it is more convenient to express it as a light pulse intensity. In S.I units, we get (see tables 2.2)

$$E_{sat} = \frac{4\pi\varepsilon_0}{e^3} \cdot \left(\frac{I_p}{2}\right)^2 \tag{2.6}$$

$$I_{sat} = \frac{c\varepsilon_0}{2} E_{sat}^2 = \frac{c\pi^2\varepsilon_0^3}{2e^3} \cdot \left(\frac{I_p}{e}\right)^4 \tag{2.7}$$

$$I_{sat}(\text{in W/cm}^2) = 0.4 \times 10^{10} \cdot \big(I_p(\text{in eV})\big)^4 \tag{2.8}$$

Numerical applications for the noble gases, which are often used for HHG, are given in table 2.3. Values are in the high 10^{13} W/cm^2 to the low 10^{15} W/cm^2 range, from the heaviest (Xe) to the lightest (He) atom.

Lighter atoms/elements with higher ionization potential can stand more laser intensity.

These values of intensities correspond to electric fields ranging from 0.25×10^{11}V/m to 1.05×10^{11}V/m, comparable to the atomic unit of field (tables 2.2).

Keldysh parameter – ionization regime

It is beyond the scope of this lecture to give much insight into the process of tunelling. This is still hotly debated in the community, in particular by the groups of ETH Zurich (U. Keller et al., Landsman and Keller [2015]), of Weizmann Institute (Dudovich et al., Shafir et al. [2012]) and of Heidelberg (Moshammer et al., Camus et al. [2017]). The question (fig. 2.6) is how long does it take for an electron to escape accross the barrier.

However, without entering the debate, we can make a few elementary enlightening considerations, by stating that it is necessary that the electron has time to cross the barrier while it is lowered. It can be estimated from the width of the barrier and the speed of the electron under the barrier. As for the width of the barrier, let us look for the locations where $V(x) = -I_p$:

$$\frac{1}{x} + E_0 x = -I_p \tag{2.9}$$

$$E_0 x^2 + I_p x + 1 = 0 \tag{2.10}$$

The discriminant of this second order polynomial equation reads $\Delta = I_p^2 - 4E_0$, and the difference between the roots is

$$\Delta x = \frac{\sqrt{I_p^2 - 4E_0}}{E_0} = \frac{I_p}{E_0}\sqrt{1 - \frac{E_0}{E_{sat}}} \tag{2.11}$$

For the speed of the particle under the barrier, thorough discussions could arise. However, an order of magnitude is given by the energy of the particle equals to its kinetic energy: $v \simeq \sqrt{2I_p}$. The time the particle spends through the barrier thus reads

$$\tau = \frac{\Delta x}{v} \simeq \sqrt{\frac{I_p}{2E^2}} \tag{2.12}$$

The criterion should be: is this time short or long compared to the laser period. It reads:

$$\gamma = \frac{\tau}{T_0} = \sqrt{\frac{I_p}{2E^2T_0^2}} \propto \sqrt{\frac{I_p}{2U_p}} \tag{2.13}$$

where U_p is the ponderomotive energy associated to the field. It is defined in atomic

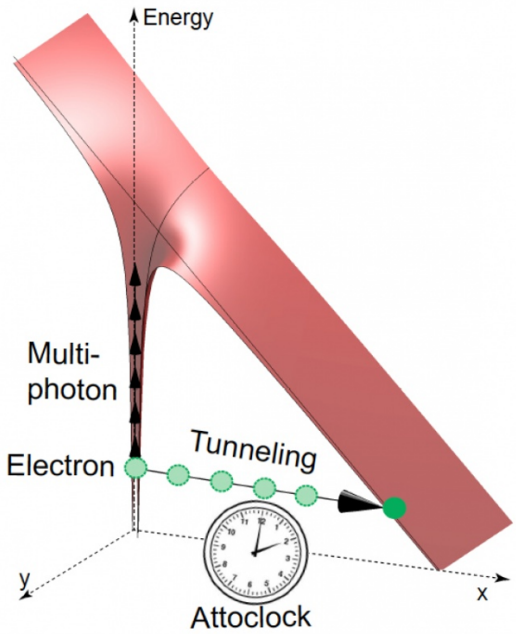

FIGURE 2.6: Sketch of tunnel ionization, from Landsman and Keller [2015]; Kheifets [2020].

and SI units as

$$U_p = \frac{I}{4\omega^2} = \frac{e^2 E_0^2}{4m\omega^2} \tag{2.14}$$

γ is called the **Keldysh parameter**. We are in the tunnel regime if γ is small.

Numerical applications: For example, for argon with an intensity of the order of 10^{14} W / cm ^{2}, a λ=800 nm laser, we get $E_0 \simeq 4\ 10^{10}$ V/m , or else $U_p = 12$ eV and $\gamma = 0.8$. It is rather in the tunnel regime. With the same parameters but a wavelength $\lambda = 3.2\ \mu$m, $\gamma = 0.2$ and it is even more towards the "tunnel regime"; while on the contrary for a UV-driving wavelength such as the third harmonic $\lambda = 266\ n$m, $\gamma = 2.4$ and it is the ATI/multiphoton regime that dominates.

Parenthesis The ponderomotive potential associated with the field is the energy that the laser field can give to an electron which oscillates in this field. Let us again consider the field $E(t) = E_0 \cos(\omega t)$, and write up Newton's equation:

$$m\ddot{x} = -eE(t) = -eE_0 \cos(\omega t), \tag{2.15}$$

We get

$$m\dot{x} = -\frac{eE_0}{\omega} \sin(\omega t) + v_0, \tag{2.16}$$

We find, for the oscillatory part, that the average kinetic energy reads

$$\left\langle \frac{m}{2} \dot{x}^2 \right\rangle = \frac{e^2 E_0^2}{4m\omega^2} = U_p, \tag{2.17}$$

which is exactly the ponderomotive energy.

> The ponderomotive energy associated to an oscillatory electric field is the mean quivering energy of an electron placed in this field.

Ionization rate: the ADK formula

The discussion above gives clues about the possibilities of the different photoionization processes. For HHG, tunnel ionization is looked for. However, it does not tell how much of the electronic wavepacket is photoionized by a given field. The theory of field induced photoionization has received a lot of interest since the 50s. In particular, in Landau and Lifshitz [1981], one can find a derivation of the photoionization rate in static fields. It was successively refined by Perelomov et al. [1966], Ammosov et al. [1986] and Tong et al. [2002] (for molecules). It is way beyond the scope of this introductory lecture to reproduce this difficult derivation. However, we reproduce the result written in Tong and Lin [2005]. For a single level with given orbital and magnetic quantum numbers (l, m), the ionization rate reads:

$$w = \frac{C_l^2}{2^{|m|}|m|!} \frac{(2l+1)\,(l+|m|)!}{2\,(l-|m|)!} \frac{1}{\kappa^{2Z_c/\kappa-1}} \cdot \left(\frac{2\kappa^3}{F}\right)^{2Z_c/\kappa-|m|-1} \cdot e^{-\frac{2\kappa^3}{3F}} \cdot e^{-\alpha \frac{Z_c^2}{I_p} \frac{F}{\kappa^3}} \tag{2.18}$$

where

- F is the electric field strength (of the laser),
- C_l is a gas dependent coefficient, ($C_l = 3.13$ for He (1s), $C_l = 2.10$ for Ne (2p),$C_l = 2.44$ for Ar (3p),$C_l = 2.49$ for Kr (4p), $C_l = 2.57$ for Xe (5p)),
- α is also a gas dependent coefficient ($\alpha = 6.0$ for He, $\alpha = 9.0$ for other rare gases),
- Z_c is the effective charge (charge seen by the active electron, set to 1 for all rare gases),
- l, m are the orbital angular momentum and magnetic quantum numbers,
- $\kappa = \sqrt{2I_p}$.

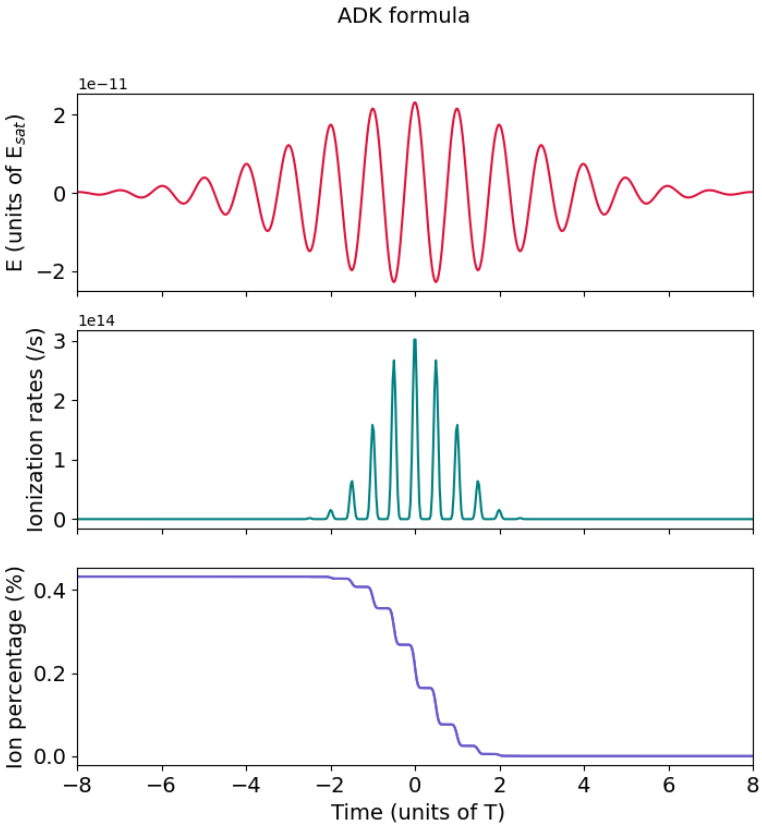

FIGURE 2.7: (top) Electric field of a laser pulse peaking at the saturation field for Argon. (middle) Instantaneous ionization rates calculated with Eq. 2.18 in Argon. (bottom) Integrated ionization, from Eq. (2.19)

The last exponential is here empirically added to model the barrier suppression regime and can be left out of the discussion in the tunneling regime. The remaining of the

formula is the so called ADK formula of ionization rates, after Ammosov, Delone and Krainov who first published it (Ammosov et al. [1986]). It is a refined version of the formula found in Perelomov et al. [1966]. The important point for HHG is the high non linearity of the function. The ionization rate is much increased for a small field increase, as apparent for instance in Fig. 2.7. So the emission will be localized around the maxima of the field. Finally, the ionization of the medium will read

$$P(t) = 1 - e^{-\int_{-\infty}^{t} w(|F(t')|)\, dt'} \tag{2.19}$$

which is also plotted in Fig. 2.7.

It is the high non linearity of the photoionization process with respect to the field amplitude that turns a field with a period in the femtosecond range in electronic bursts with attosecond durations.

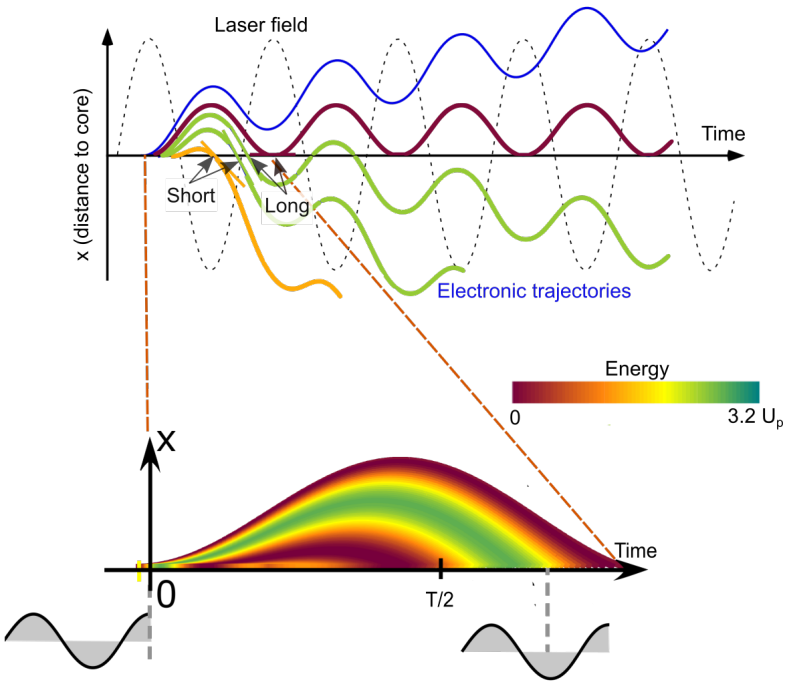

FIGURE 2.8: (Top) A few classical trajectories, for a sequence of t_i close to a maximum of the electric field of the laser (dotted line). The vertical axis is the distance from the ionic core. Four trajectories are highlighted in colors encoding their slope when they cross the x=0 axis, i.e. the energy of the corresponding electron. (Bottom) Zoom in the first laser period, with many more initial times computed, and color encoding the energy of the electrons at the time of recombination.

2.1.4 Excursion of the electron in the continuum

The electron in the continuum evolves under the effect of the laser field which, as a first approximation may be described using Newton's equation:

$$m\ddot{x} = -eE(t) = -eE_0\cos(\omega t), \tag{2.20}$$

Here we neglect the effect of the ionic potential, once the electron has tunneled out (at t_i). We also consider that the initial conditions are $(x(t_i) = 0, \dot{x}(t_i) = 0)$. It should be noted that this is probably inconsistent with the discussion on ionization, but it is sufficient as a first step. The position reads

$$m\dot{x} = -\frac{eE_0}{\omega}\left(\sin(\omega t) - \sin(\omega t_i)\right) \tag{2.21}$$

$$x(t) = \frac{eE_0}{m\omega^2}\left[\cos(\omega t) - \cos(\omega t_i)\right] + \frac{eE_0}{\omega}\sin(\omega t_i)\left[t - t_i\right]. \tag{2.22}$$

These trajectories are the sum of two main terms (within brackets). The first term is oscillatory, while the second is a line, whose slope may be positive or negative, depending on $\sin t_i$. Some of them are plotted in Fig. 2.8. In particular, for some values of t_i they pass back by the ionic core at x=0 for $t > t_i$. The slope at this time ($\dot{x}$) determines the kinetic energy at the instant of recollision. Fig. 2.9 shows that these kinetic energies vary depending on the ionization time. An important point is that it is all deterministic: a given time of birth corresponds to a given energy at a given time of recombination. An outcome of this recollision is the radiative recombination, in which the electron gives back its kinetic energy as a photon.

More precisely, scrutinizing Fig. 2.8, it is observed that two trajectories, recombining at different times have the same energy [3]. While these are experimentally observable (see Fig 3.10), higher order trajectories, which theoretically exist (Fig. 2.8), have never been reported. These two first trajectories are so called the "*short*" and the "*long*" trajectories.

The electrons are going really "far" from the ionic core. If we evaluate the leading term in Eq. (2.22), we have, for a wavelength λ=800 nm and a field equal to the saturation field, the order of magnitude of the excursion given by $\frac{eE_{sat}}{m\omega^2}$. It is equal to 3.3 nm for Helium, and 0.8 nm for Xenon. For Helium, it is tens of times the classical "size" of the atom. This distance scales as λ^2, so for a λ=3.2 μm laser, they respectively get 53 nm and 13 nm. To see how "large" this distance is, let us compare it to the mean distance between two particles in a gas cell. For a pressure of gas of 10 mbars=100 Pa, at a temperature of 300 K, we have roughly a density of atoms of $n = P/kT = 2.4\times10^{22}$ atoms/m^3. The "mean distance" between atoms will be roughly given by $\frac{1}{n^{1/3}}$=34 nm. At P=100 mbar, it gets down to 16 nm. We see that for visible lasers, atoms are playing their parts independently (the electrons are not going that far), while for midIR lasers, electrons might go so far that they "explore" neighboring atoms.

The instant at which the electron passes by the core is the instant at which it may recombine and emit a photon. We call it the recombination time, or emission time. From Fig. 2.8, one may deduce the emission time as a function of the energy of the

[3] If we focus on Fig. 2.8, there are more, but the other (longer ones) are usually completely negligible.

photon. This is reported in Fig. 2.9. To build this figure progressivelly, let us start from trajectories close to the orange one in Fig. 2.8 (top). We see in Fig. 2.8 (bottom) that in this region of the short trajectories, as the emission time increases, so does the energy. Spanning the short trajectories thus gives the lower branch of Fig. 2.9. About 2T/3, the energy gets stationary, while finally decreasing as the recombination time increases. This part, the long trajectory, builds the upper branch of the curve in Fig. 2.9.

Two behaviors may be identified:

- The plateau range, where the group delay dispersion (GDD) is constant (group delay (GD) linear)
- The cutoff range, where the GDD is zero (constant GD), and the short and long trajectories merge together.

The second important observation is that all energies are not obtained. There is a maximum which is obtained numerically (cutoff law)

$$E_{\text{cutoff}} = (1.3)I_p + 3.17U_p \tag{2.23}$$

This is one of the most famous and important rule when dealing with HHG. It says that the more intense the laser field is, the higher the energies of the harmonics may be. But for a given gas, intensity is limited by the saturation intensity of this gas, which increases as the gas gets lighter.

Numerical application : if we set $U_p = 12\,\text{eV}$, which corresponds to the saturation electric field in argon at a wavelength of 800 nm, the cutoff is about 40 eV above the I_p. With a photon of 1.5 eV, it yields a cutoff about harmonic 27 above the threshold,

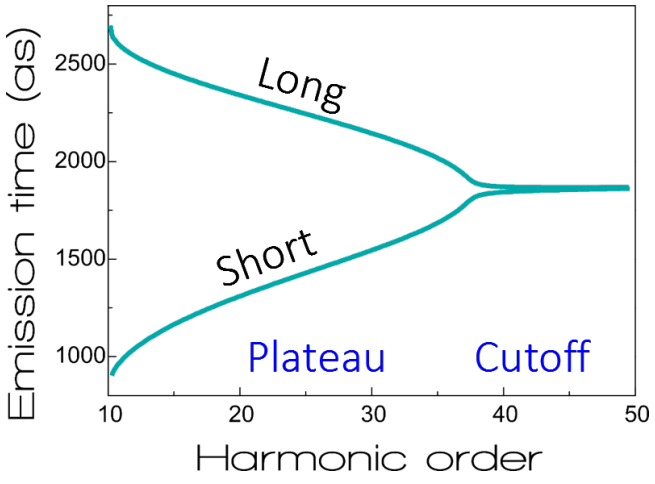

FIGURE 2.9: Correspondance between recombination time and energy at this time, expressed in multiple of the driving laser photon's energy, which can be deduced from Fig. 2.8.

i.e. H37 for argon, or an energy of 58 eV. For Neon, we may reach about 100 eV at saturation intensity.

To increase the cutoffs, the alternative is to change the wavelength towards longer wavelengths. This is a very active current research area, where HHG is studied with lasers in the 3-4 μm wavelength range. This is very attractive since it is a quadratic law. However the yield is dramatically reduced, as a $\simeq \lambda^{-7}$ law.

Note that the last initial question raised page 17 is implicitly resolved: there is a well defined phase relationship between successive harmonics. The phase should be controlled, although not flat.

2.2 Elements of the strong field approximation (SFA)

To get insights into the last step – the recombination step, we now discuss the results of the quantum version of the three step model. It was proposed by M. Lewenstein et al. in 1994 and is called the "strong field approximation" (SFA, Lewenstein et al. [1994]). It is based on a perturbative method and yields the following expression of the position of the electron while the laser perturbs it:

$$\vec{x}(t) = -i \int_0^t dt_i \int d\vec{p} \underbrace{\vec{d}^*_{\vec{p}+e\vec{A}(t)}}_{\text{recombination}} \underbrace{e^{i\frac{S(\vec{p},t_i,t)}{\hbar}}}_{\text{excursion}} \underbrace{\vec{E}(t_i)\cdot\vec{d}_{\vec{p}+e\vec{A}(t_i)}}_{\text{ionization}} \tag{2.24}$$

where

$$S(\vec{p},t_i,t) = -\int_{t_i}^t dt \left(I_p + \left(\vec{p}+e\vec{A}(t)\right)^2/2 \right) \tag{2.25}$$

is the action integral. Reading equation 2.24 from right to left, we successively recognize three terms corresponding to each step of the three-step model. t_i is the ionization time and t is the recombination time. A very nice introduction to this, including hints to make your own code for sufficiently long pulses is available in Smirnova and Ivanov [2013].

The Fourier transform of the position, that is to say, the induced dipole, gives the radiated spectrum. It reads

$$\vec{x}(\omega_q) = \int_{-\infty}^{+\infty} dt\ \vec{x}(t) e^{i\omega_q t} \tag{2.26}$$

The computation of this quantity is not straightforward. In particular the phase varies rapidly, requiring convoluted integration methods. However the stationary phase principle (Fermat principle) may be applied in such a situation. The derivation may be carried out against each variable successively : $\vec{p}, t_i, t$. Deriving against t, it reads

$$\frac{\partial S(\vec{p},t_i,t) + \omega_q t}{\partial t} = 0 \tag{2.27}$$

which gives

$$\omega_q = I_p + \frac{\left(\vec{p}+e\vec{A}(t)\right)^2}{2} = I_p + E_k \tag{2.28}$$

We here find the anticipated equation for energy conservation at recombination time t.

Deriving against $\vec{p}$, requires the 3D-derivation:

$$\vec{\nabla}_{\vec{p}}\left(S(\vec{p},t_i,t)+\omega_q t\right)=0 \tag{2.29}$$

which reads

$$-\vec{\nabla}_{\vec{p}}\int_{t_i}^{t} dt\left(I_p+\left(\vec{p}^{\,2}+2e\vec{p}.\vec{A}(t)+\vec{A}^2(t)\right)/2\right) = 0 \tag{2.30}$$

$$-\vec{\nabla}_{\vec{p}}\left[\left(I_p+\vec{p}^{\,2}\right)\left(t-t_i\right)+\int_{t_i}^{t} dt\left(2e\vec{p}.\vec{A}(t)+\vec{A}^2(t)\right)/2\right] = 0 \tag{2.31}$$

$$\vec{p}\cdot\left(t-t_i\right)+\int_{t_i}^{t} dt\, e\vec{A}(t) = 0 \tag{2.32}$$

Note that taking a derivative of the latter against the recombination time t yields

$$\vec{p}=e\vec{A}(t) \tag{2.33}$$

$$\frac{d\vec{p}}{dt}=-e\vec{E}(t) \tag{2.34}$$

which is nothing but Newton's equation of movement. This last stationary phase condition is thus related to the closure of the trajectories studied above.

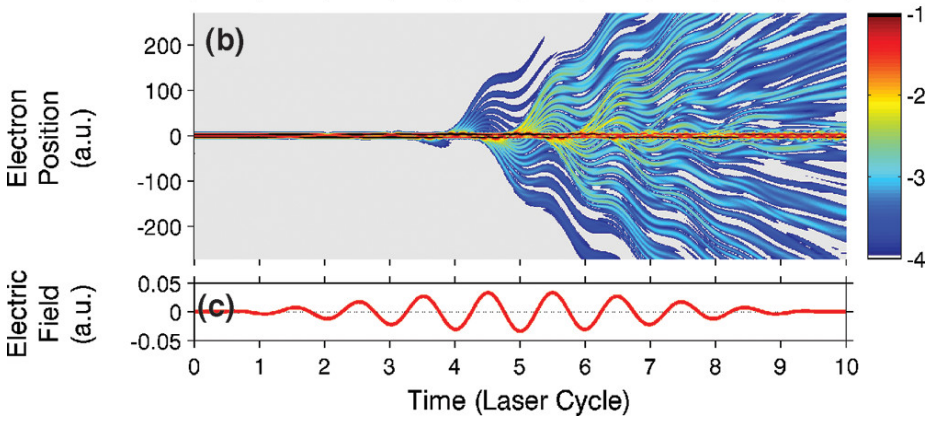

FIGURE 2.10: Quantum trajectories (with no SFA approximation), from Takemoto and Becker [2011].

Finally, one may write a stationary phase for the ionization time t_i. it reads

$$\frac{\partial S(\vec{p},t_i,t)+\omega_q t}{\partial t_i}=0 \tag{2.35}$$

which gives

$$I_p + \left(\vec{p} + e\vec{A}(t_i)\right)^2 /2 = 0 \tag{2.36}$$

It apparently leads to an impossibility: the ionization potential I_p being positive, this equation requires a negative kinetic energy term to be fulfilled. It can be solved by considering an "imaginary" velocity, $\vec{k}_s(t_i) = \vec{p}_s + e\vec{A}(t_i)$, and thus a complex "ionization time". The appearance of this complex time is linked to the tunnel nature of the process: the electron should not be able to escape the barrier in a classical world, while in the quantum world, the real part of t_i is interpreted as the time at which the electron exits the barrier (see Smirnova and Ivanov [2013], Maquet et al., 2014).

The full quantum model validates these approximations (cf. Fig. 2.10).

2.3 Polarization of the emitted harmonics

> Due to the symmetry of the problem, when the driving laser is linearly polarized, the XUV radiation is also linearly polarized, along the same axis.

This result stems from the fact that, when getting back to the ionic core, the recolliding electron excites a dipole along its propagation direction, i.e. along the linear polarization of the driving laser.

Now we can examine what happens if the driving laser is elliptically polarized (ellipticity ϵ). The second step of the model states that HHG happens when the electron recollides with the ionic core. Since the driving field has two orthogonal components, the Newton equation states that the electron may be drifted away from the core by the perpendicular component. If ϵ is large, it should never interact with it again to emit XUV photons. In practice, the electron is a quantum object, i.e. an electronic wave packet (EWP), that has a certain spatial extension around the mean propagation direction. This spreading of the EWP increases with time. Part of it can thus still interact with the ionic core, but with a reduced overlap, and therefore reduced efficiency. It is often observed that the HHG yield scales as a gaussian with the ellipticity of the driver, with a width $\epsilon_{th} \simeq 0.2 - 0.4$:

$$I(\epsilon) = e^{-\frac{\epsilon^2}{\epsilon_{th}^2}} \tag{2.37}$$

It is interesting to note that for a driving laser of ellipticity ϵ_{th}, the mean offset of the EWP along the transverse direction y is exactly equal to its spreading after propagation during the excursion time (see Strelkov et al. [2011, 2012]).

The state of polarization of the emitted harmonics in this case is not easily modeled. Again, Refs. Strelkov et al. [2011, 2012] are enlightening in that respect. In brief, the polarization is elliptical, with a main axis along the recombination angle of the trajectories. It turns out to increase linearly with the ellipticity, with opposite slopes for the short and long trajectories Strelkov [2006]. As for the ellipticity, its origin is more subtle: it relies on the fact that, due to its offset along y, the EWP has a varying and non symmetrical amplitude across the fundamental state at the recombination time. The elegant demonstration of Strelkov et al. [2012] is reproduced here.

Let us consider an even (real) fundamental wave function, $\psi_0(x,y,x) = \psi(x)\,\psi(y)\,\psi(z)$ (you may think of a s-state). We describe the recolliding wave function as $\chi(x,y,z) = f(y,z)e^{ipx}$, where $f(y,z)$ models its transverse extension, and e^{ipx} its propagation as a plain wave along x. Due to the ellipticity of the driving field, the EWP is offset along y at the recombination time. We can thus Taylor expand $f(y,z) \simeq f_0 + y f_1$. The electric dipole formed by the overlap of these two wavefunctions reads

$$\begin{aligned}\vec{d} &= \iiint dx\,dy\,dz\;\psi_0^*\vec{r}\chi(x,y,z) \\ &= \iiint dx\,dy\,dz\;\psi_0^*\vec{r}(f_0 + f_1 y)e^{ipx} \qquad (2.38)\\ & \qquad (2.39)\end{aligned}$$

For the x-component, we will have a term proportionnal to f_0 reading

$$d_x = f_0 \int dz\;\psi(z) \int dy\;\psi(y) \int dx\;x\,\psi(x)e^{ipx}; \qquad (2.40)$$

and a term proportionnal to f_1

$$f_1 \int dz\;\psi(z) \int dy\;y\psi(y) \int dx\;x\,\psi(x)\,\psi(x)e^{ipx} = 0, \qquad (2.41)$$

where we have taken into account the fact that $\psi(y)$ is considered even, and thus the integral over y of $y\psi(y)$ is zero. Similarly, for the y-component, it is the f_0 term that will vanish and we get

$$d_y = f_1 \int dz\;\psi(z) \int dy\;y^2\psi(y) \int dx\;\psi(x)e^{ipx} \qquad (2.42)$$

The Fourier transform of an even (resp. odd) real function is real (resp. imaginary). We thus observe that, due to the last integrals, the two components of the dipole along x and y are just $\pi/2$ out of phase. It yields an elliptical polarization of the emission, which scales as the offset of the EWP (f_1), i.e. with the ellipticity of the driving field.

This model is very coarse and refinements may be found in the literature. It is still a research subject for theoreticians, in particular with less conventional driving fields.

2.4 Summary of Chapter 2

In this chapter we have seen that

- In a laser field comparable to the atomic field, an atom may serve as a highly non-linear medium.
- If the field is above a certain "saturation intensity", the atom ionizes directly, which should be avoided to make attosecond pulses. If the Keldysh parameter is below 1, the system is in the tunneling regime, which should be privileged.

- An electron burst can be emitted during a very narrow time window around an extremum of the field: for a driving laser with femtosecond period, the window has a duration in the 100 as range. This is the origin of attosecond light pulses.
- This EWP will then be driven by the laser electric field and may recombine with the ionic core, with given energy at certain time. There is an almost linear relation between the energy and the emission time.
- At recombination, the energy is released as a photon. The energy of the photon is capped by the "cutoff" law, scaling linearly with the ponderomotive potential of the laser field.
- The polarization of the harmonics "follows" that of the driving field: they are linearly polarized when the driving field is linearly polarized, elliptically polarized when the driving field is elliptically polarized. However, the yield vanishes quickly with the driver's ellipticity.

CHAPTER 3

HHG WITH A MULTIPLE CYCLES LASER PULSE IN A MACROSCOPIC MEDIUM

In the previous chapter, we have focused on what was happening to a single atom, during one half cycle of the laser period, or slightly more. In most of practical situations, the lasers are lasting many optical cycles. For instance, a 20 fs long laser pulse, with λ=800 nm, corresponding to a period T=2.7 fs, corresponds to 7 full cycles of the laser beam. The first question we address here is "how successive half cycles sum up"? (Sec. 3.1). Second, to have a measurable signal, the contributions from several atoms of a macroscopic target should be summed up. This sum is detailed in Sec. 3.2.

3.1 Periodicity in time: narrow harmonics, broad harmonics, continuous spectrum

3.1.1 Continuous spectrum

The whole discussion in Chapter 2 was dealing with what happens during half a cycle of the laser field. Today, it becomes possible to synthesize a strong laser field that indeed last only half a cycle, or a few cycles. The "thresholding" effect of tunnel ionization will make the 3-step process happen only once during the pulse. We thus get a spectrum which **continuously** extend from the first frequency to the cutoff value. Why do we still call it an "harmonic spectrum"? This is an historical leftover, as explained in the next section.

3.1.2 Harmonic spectrum

The first lasers used for HHG had picosecond durations. The 3-step process could thus happen many times the laser pulse, each time the electric field reached a positive or negative extremum. The periodicity of the process was thus T/2, with T the period of the laser. In the frequency domain, it corresponds to a "periodicity" of the comb of $\Delta\omega = 2\pi \cdot \frac{2}{T}$. This is the origin of the periodicity in the spectral domain and the origin of the name "high harmonic generation".

To be more specific, let us consider a laser pulse, that is divided in n_p half cycles. Each of these n_p half cycles, the same XUV pulse is emitted, with a bell-shaped envelope $G(t)$, a central frequency ω_{xuv} and an emission time t_i. The emission start at half cycle indexed n_0, at time $n_0 T/2$. It is important to note that every half cycle, the emission is π out of phase with the preceding one. This can be visualized in Eq. (2.24). Indeed, $\vec{d}^*_{\vec{p}+e\vec{A}(t)}$ does not change sign (it does not depend on the field). $\vec{E}(t_i) \cdot \vec{d}_{\vec{p}+e\vec{A}(t_i)}$ will change sign, due to the change of sign of the driving field ($\vec{E}(t_i) = -\vec{E}(t_i + \frac{T}{2})$). The action integral remains unchanged: $\vec{p}$, which is the momentum of the electron changes sign (the electron moves on the other side of the ion), the vector potential $\vec{A}(t)$ as well, so $\left(\vec{p} + \vec{A}(t)\right)^2$ is unchanged and neither is its integral, nor $S(\vec{p}, t_i, t)$). This phase flip is taken into account by a $(-1)^n = e^{i\,n\cdot\pi}$ in the total electric field that reads:

$$E(t) = G(t)e^{i\omega_{xuv}(t_i+t)} \otimes \sum_{n=n_0}^{n_1} e^{i\,n\cdot\pi}\,\delta\left(t - n\frac{T}{2}\right) \tag{3.1}$$

where the convolution with the delta function just offsets the patterns to make a train of identical pulses. The spectrum of this field will be given by its Fourier transform:

$$\tilde{E}(\omega) = \mathcal{F}\left(G(t)e^{i\omega_{xuv}\cdot(t_i+t)}\right) \times \left[\sum_{n=n_0}^{n_0+n_p-1} e^{in\left(\omega\cdot\frac{T}{2}+\pi\right)}\right] \tag{3.2}$$

$$= e^{i\omega_{xuv}\cdot t_i} \cdot \left[\tilde{G}(\omega) \otimes \delta\left(\omega - \omega_{xuv}\right)\right] \cdot \frac{e^{in_0\left(\omega\cdot\frac{T}{2}+\pi\right)} - e^{i(n_0+n_p)\left(\omega\cdot\frac{T}{2}+\pi\right)}}{1 - e^{i\omega\cdot\frac{T}{2}+i\pi}} \tag{3.3}$$

$$= e^{i\omega_{xuv}\cdot t_i} e^{i(n_0+\frac{n_p-1}{2})\left(\omega\cdot\frac{T}{2}+\pi\right)} \cdot \tilde{G}\left(\omega - \omega_{xuv}\right) \cdot \frac{\sin\left(n_p \cdot \left(\omega\cdot\frac{T}{4} + \frac{\pi}{2}\right)\right)}{\sin\left(\omega\cdot\frac{T}{4} + \frac{\pi}{2}\right)} \tag{3.4}$$

The first terms before $\tilde{G}$ are of little importance here. $\tilde{G}(\omega - \omega_{xuv})$ is a bell shaped function, centered on ω_{xuv} as expected, with a width inversally proportional to the width of $G(t)$, i.e. of each attosecond pulse. We retrieve the fact that the width of the spectrum firstly rules its attosecond structure. The last term is a spectral comb (Fig. 3.1). It peaks whenever the denominator is zero, i.e., with $p \in \mathbb{Z}$

$$\omega\frac{T}{4} + \frac{\pi}{2} = p \cdot \pi$$

$$\omega = (2p-1)\,\frac{2\pi}{T}$$

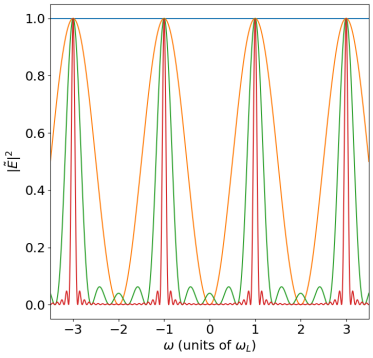

FIGURE 3.1: Plots of the last sine ratio of Eq. (3.4) for n_p= 1 pulse (blue), n_p=2 (orange), n_p=5 (green) and n_p=20 (red). The x-axis is scaled in units of the laser angular frequency, $\omega_L = 2\pi/T$.

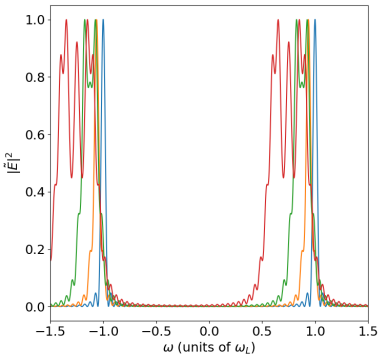

FIGURE 3.2: Same as the plot on the left, for n_p=40, but with a modulation coefficient $\alpha I_0 \left(\frac{T}{2\tau}\right)^2$ (Eq. (3.9)) of 0.0 (blue), 0.05 (orange), 0.1 (green) and 0.2 (red).

We retrieve the fact that only odd multiples of the fundamental are generated. The role of the π phase shift between successive half cycles is central: if it was not present, it would be only even multiples that would be generated. For instance, if the medium was not centro-symmetric, there would be no reason to have every successive half cycles exactly identical XUV pulses with opposite phases and even harmonics could be generated. this is a prolongation of the rule of perturbative non linear optics: in a centro-symmetric medium, only odd harmonics can be generated. For instance, second harmonic generation is strictly zero.

We now calculate the width of a peak. Since they are all identical, and the $\pi/2$ only shifts them by one unit of $2\pi/T$, without loss of generality we can temporarily remove this $\pi/2$ phase, and focus on the peak corresponding to $p = 0$, i.e. $\omega \cdot \frac{T}{4} \ll 1$. We make a Taylor expansion of it, about 0 and find

$$\begin{aligned}
\frac{\sin\left[n_p \cdot \frac{\omega T}{4}\right]}{\sin\left[\frac{\omega T}{4}\right]} &\simeq \frac{n_p \cdot \frac{\omega T}{4} - \frac{1}{6}\left(n_p \cdot \frac{\omega T}{4}\right)^3}{\frac{\omega T}{4} - \frac{1}{6}\left(\frac{\omega T}{4}\right)^3} \\
&\simeq n_p \frac{1 - \frac{1}{6}\left(n_p \cdot \frac{\omega T}{4}\right)^2}{1 - \frac{1}{6}\left(\frac{\omega T}{4}\right)^2} \\
&\simeq n_p \left[1 + \frac{1 - n_p^2}{6}\left(\frac{\omega T}{4}\right)^2\right]. \qquad (3.5)
\end{aligned}$$

The peak value is n_p. To find the FWHM of the peak, we look for locations where tthe

value is $n_p/2$. We get

$$1 + \frac{1-n_p^2}{6}\left(\frac{\omega T}{4}\right)^2 = \frac{1}{2}$$
$$\left(\frac{\omega T}{4}\right)^2 = \frac{3}{n_p^2-1}$$
$$\omega = \pm\frac{4}{T}\sqrt{\frac{3}{n_p^2-1}} \tag{3.6}$$

The width of the peak, over the "Free Spectral Range" $4\pi/T$, which is the distance between two peaks is thus

$$\frac{\Delta\omega}{4\pi/T} = \frac{2}{\pi}\sqrt{\frac{3}{n_p^2-1}} \xrightarrow[n_p\to\infty]{} \frac{1.1}{n_p} \tag{3.7}$$

This result states that the peaks are all the narrower as the number of pulses contributing increases. In other words, with a long driving laser pulses, harmonics are spectrally narrow, while they spectrally broaden as the laser pulse duration decreases. It ends, with a single half cycle contributing, covering the full free spectral range, i.e. giving a continuous spectrum. We here get the connection between the 3-step model giving a continuous spectrum, and the experimentally more common harmonic spectra. In summary:

1. Only odd harmonics are present,
2. The width of each harmonic is inversely proportional to the number of pulses contributing, i.e. the driving pulse duration.

3.1.3 Non adiabatic effects

We call non adiabatic effects, the fact that the driving electric field is not a pure sine wave, but has an envelope that may vary from one cycle to the next, or even during one single cycle for a very short pulse (should we still speak of an envelope in this case?). This has strong effects on the harmonic spectrum. For instance, let us consider that the phase is proportional to the instantaneous intensity of the field, α being the proportionality constant (Fig. 3.8). We also consider a field showing a Gaussian amplitude. HHG occurs close to the maximum of the field, where the Gaussian, of duration τ, reduces to a parabola: $I(t) = I_0(1 - \frac{t^2}{\tau^2})$. Eq. (3.1) becomes (dropping the constant phase term proportional to I_0)

$$E(t) = G(t)e^{i\omega_{xuv}(t_i+t)} \otimes \sum_{n=n_0}^{n_1} e^{i\,n\cdot\pi-\alpha I_0\left(\frac{nT}{2\tau}\right)^2}\delta\left(t - n\frac{T}{2}\right) \tag{3.8}$$

The spectrum gets

$$\tilde{E}(\omega) = \mathcal{F}\left(G(t)e^{i\omega_{xuv}\cdot(t_i+t)}\right) \times \left[\sum_{n=n_0}^{n_0+n_p-1} e^{in\left(\omega\cdot\frac{T}{2}+\pi-\alpha I_0\left(\frac{T}{2\tau}\right)^2\cdot n\right)}\right] \tag{3.9}$$

The first term is unchanged, while the last term is almost the same sum as for the pure case (compare to Eq. (3.1)), but for a common ratio of the geometrical series that changes with n. It is thus no longer strictly speaking a geometrical sum. We can readily see that this offset has the same role as the π offset in Eq. 3.4 and will therefore progressively shift the comb. It results in a broadening of the harmonics as apparent in Fig. 3.2, and a shift of the mean peak value.

Other such effects may occur in the medium, making the harmonics not falling exactly at odd multiple orders of the fundamental (See e.g. Fig. 3.10). Also, it should be noticed that observing a broad harmonic is not sufficient to conclude on having very few attosecond pulses. Such non adiabatic effects may be the reason for the broadening and a full temporal characterization should be undertaken in any case.

3.2 Macroscopic medium: influence of phase matching

3.2.1 Introduction to phase matching

As with any non-linear optical phenomena, phase matching aspects come into play in high harmonic generation (Fig. 3.3). These are crucial and especially difficult to control for HHG, due to the very broad width of the spectrum, the high absorption of the gas involved, and the number of terms that affect the phase. More precisely, HHG will occur

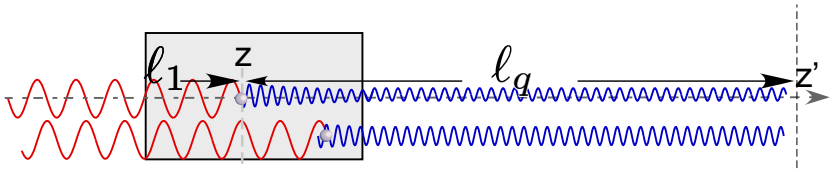

FIGURE 3.3: Phase matching principle. The incoming beam is in red. The XUV field in blue. For two atoms that may generate XUV light located at two different points, the driving laser propagate different lengths to reach the atoms, getting dephased, and so do the elementary XUV fields radiated when propagating to the detector. Phase matching is about finding the conditions in which all elementary electric fields add up coherently, hence reducing the variation of these dephasings with space and time.

in a gas medium close to the focus of a high intensity laser beam. By high intensity, one speaks of an intensity that may partially ionize the medium, as detailed in Sec. 2.1.3. Depending on the location in the medium and instant considered, there might be

1. different ions/electron densities vs neutral density ratios, hence different optical indices of the driving laser and XUV;

2. different intensities, hence giving different “3-step” responses and in particular, phases of the emission;

3. different optical phases of the driver: the medium is usually of a fraction of mm to a few mm long, not always negligible with respect to the Rayleigh length (z_R) of the beam. The Gouy phase and curvature of the beam may vary in the cell.

All of these play a role in phase matching.

3.2.2 A (fairly) simple model of phase matching

We over simplify the situation by considering an infinite long and large driving pulse, having all of its half cycles equal in time and space in the generating medium (Fig. 3.4), i.e. a plane monochromatic wave. In addition, we consider that the ionization of

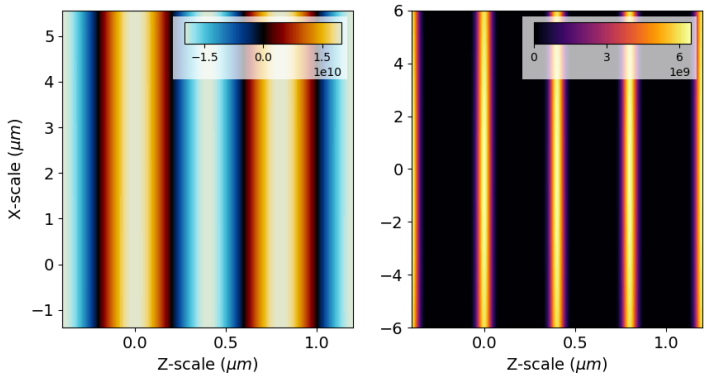

FIGURE 3.4: (left) Electric field of the driving laser for the phase matching model. The beam is propagating along z. The peak electric field is 4 10^{10}V/m, corresponding to half the saturation field for Argon. (right) Corresponding values of the ADK ionization rates in Argon.

the medium does not change with time. This is absolutely wrong: once it is ionized, an atom will not be refreshed by any gas flow during the time a regular femtosecond light pulse passes in the medium. And consequently, every half cycle the ionization of the medium is increasing. However, these hypothesis allow to define non spatial nor time dependent indices of refraction for both the XUV and IR field. It makes the model analytically tractable, while still giving insights into the relevant parameters.

The analytical representation associated to the plane monochromatic laser electric field reads, at location $\vec{r}$ and time t

$$\mathcal{E}_L(\vec{r},t) = \mathcal{E}_0 e^{i\omega_1 t - \vec{k}_1 \cdot r} \tag{3.10}$$

where we have noted ω_1 and $\vec{k}_1$ its angular frequency and wave vector. The latter is along the z axis (unit vector $\hat{z}$). It forms a series of positive and negative large stripes (Fig. 3.4 (left)). Applying the ADK formula to these stripes yields (Fig. 3.4 (right))

a series of very narrow stripes centered about the extrema of the field. The center of stripe n, corresponding to $\omega_1 t - \vec{k}_1 \cdot \vec{r} = -n\pi$ is located around

$$\vec{r}_n = \left(n\frac{\lambda_1}{2} + ct \right) \cdot \hat{z}. \tag{3.11}$$

Every even (resp. odd) n corresponds to a positive (resp. negative) field. HHG will occur around these regions. We define a bell-shaped function (for instance a Gaussian) describing the electric field generated by an atom located about this maximum $G(\vec{r})$. It has a width of a fraction of λ_1, and could be complex to take into account some intensity or driving phase dependence of the HHG signal. The elementary electric field detected on a screen at $\vec{r}_s$, generated with a wavevector $\vec{k}_q$, angular frequency $\omega_q = q\omega_1$, from a given location ($\vec{r}$) within stripe n reads:

$$e_{\text{xuv}}(\vec{r}, t) = e^{iq\left(\omega t - \vec{k}_1 \cdot \vec{r}\right)} \cdot e^{-i\vec{k}_q \cdot (\vec{r}_s - \vec{r})} \cdot \left[G(\vec{r}) \otimes \delta(\vec{r} - \vec{r}_n) \right]. \tag{3.12}$$

Here we need not consider q to be an integer. The first exponential just states that the phase of the outgoing radiation is q times the phase of the incoming driving radiation, like in any non linear optical phenomenon. The second exponential is simply the phase accumulated by the XUV radiation from $\vec{r}$ towards the observation point propagation at $\vec{r}_s$. With a convolution, the G function is translated to the right stripes to give the "3-step" answer, concentrated around the extrema of the stripes. This equation can be rewritten

$$e_{\text{xuv}}(\vec{r}, t) = e^{i\left(\omega_q t - \vec{k}_q \cdot \vec{r}_s\right)} \cdot e^{i\left(\vec{k}_q - q\vec{k}_1\right) \cdot \vec{r}} \cdot G(\vec{r} - \vec{r}_n) \tag{3.13}$$

$$= e^{i\left(\omega_q t - \vec{k}_q \cdot \vec{r}_s\right)} \cdot e^{-i\Delta\vec{k}_q \cdot \vec{r}} \cdot G(\vec{r} - \vec{r}_n) \tag{3.14}$$

where we introduced the phase mismatch:

$$\boxed{\Delta\vec{k}_q = q\vec{k}_1 - \vec{k}_q} \tag{3.15}$$

To get the contribution of a given stripe n to the far-field, we introduce the atomic density ρ, supposed to be homogeneous and sum over space:

$$E_n(\Delta\vec{k}_q) = e^{i\left(\omega_q t - \vec{k}_q \cdot \vec{r}_s\right)} \cdot \iiint \rho d^3\vec{r} e^{-i\Delta\vec{k}_q \cdot \vec{r}} \cdot G(\vec{r} - \vec{r}_n) \tag{3.16}$$

Making a change of variable $\vec{r'} = \vec{r} - \vec{r}_n$ we get

$$E_n(\Delta\vec{k}_q) = \rho e^{i\left(\omega_q t - \vec{k}_q \cdot \vec{r}_s\right)} \cdot e^{i\Delta\vec{k}_q \cdot \vec{r}_n} \cdot \iiint d^3\vec{r'} \cdot G(\vec{r'}) \cdot e^{-i\Delta\vec{k}_q \cdot \vec{r'}}$$

$$= \rho e^{i\left(\omega_q t - \vec{k}_q \cdot \vec{r}_s\right)} \cdot e^{i\Delta\vec{k}_q \cdot \vec{r}_n} \cdot \tilde{G}(\Delta\vec{k}_q). \tag{3.17}$$

where we have noted $\tilde{G}(\Delta\vec{k}_q)$ the 3D Fourier transform of $G(\vec{r})$. Only the second term depends on the stripe's number. The total field is the sum of all these contributions.

Using Eq. (3.11), we get

$$E_q(\Delta\vec{k}_q) = \sum_{\text{medium}} E_n(\Delta\vec{k}_q) \tag{3.18}$$

$$= \rho e^{i\left(\omega_q t - \vec{k}_q\cdot\vec{r}_s\right)} \cdot \tilde{G}(\Delta\vec{k}_q) \cdot \sum_{\text{medium}} e^{i\Delta\vec{k}_q\cdot\vec{r}_n} \tag{3.19}$$

$$= \rho e^{i\left(\omega_q t - \vec{k}_q\cdot\vec{r}_s\right)} \cdot \tilde{G}(\Delta\vec{k}_q) \cdot e^{i\Delta\vec{k}_q\cdot\hat{z}ct} \cdot \sum_{\text{medium}} e^{in\cdot\Delta\vec{k}_q\cdot\hat{z}\frac{\lambda_1}{2}} \tag{3.20}$$

The last sum extends for n spanning the generating gas cell/jet. We denote L_{med} the medium's length. Since the periodicity of the stripes is $\frac{\lambda_1}{2}$, we can choose to label n from 0 to $N = 2\frac{L_{med}}{\lambda_1}$. We write $\Delta\vec{k}_q \cdot \hat{z} = \Delta k_q^z$. We thus have

$$E_q(\Delta\vec{k}_q) = \rho e^{i\left(\omega_q t - \vec{k}_q\cdot\vec{r}_s\right)} \cdot \tilde{G}(\Delta\vec{k}_q) \cdot e^{i\Delta k_q^z ct} \cdot \sum_{\text{n=0}}^{N} e^{in\cdot\left(\Delta k_q^z\cdot\frac{\lambda_1}{2}\right)} \tag{3.21}$$

$$= \rho e^{i\left(\omega_q t - \vec{k}_q\cdot\vec{r}_s\right)} \cdot \tilde{G}(\Delta\vec{k}_q) \cdot e^{i\Delta k_q^z ct} \cdot \frac{1 - e^{iN\cdot\left(\Delta k_q^z\cdot\frac{\lambda_1}{2}\right)}}{1 - e^{i\cdot\left(\Delta k_q^z\cdot\frac{\lambda_1}{2}\right)}} \tag{3.22}$$

$$= \rho e^{i\left(\omega_q t - \vec{k}_q\cdot\vec{r}_s\right)} \cdot \tilde{G}(\Delta\vec{k}_q) \cdot e^{i\Delta k_q^z ct} \cdot \frac{1 - e^{i\Delta k_q^z\cdot L_{med}}}{1 - e^{i\frac{\Delta k_q^z\cdot\lambda_1}{2}}} \tag{3.23}$$

Due to the absorption in the medium, Δk_q^z is usually complexed valued. We introduce the coherence length and absorption length of the medium as

$$\Delta\vec{k}_q \cdot \hat{z} = \Delta k_q^z = \frac{\pi}{L_{coh}} + i\frac{1}{L_{abs}} \tag{3.24}$$

As we will see below, these lengths are usually of the order of the medium length, $L_{med} \gg \lambda_1$. The denominator can thus be Taylor expanded and the intensity of this

radiation reads

$$I_q(\Delta\vec{k}_q) = \rho^2 \left|\tilde{G}(\Delta\vec{k}_q)\right|^2 \cdot \left| \frac{1 - e^{-\frac{L_{med}}{L_{abs}}} \cdot e^{i\frac{\pi L_{med}}{L_{coh}}}}{1 - e^{-\frac{\lambda_1}{2L_{abs}}} \cdot e^{i\frac{\pi\lambda_1}{2L_{coh}}}} \right|^2 \tag{3.25}$$

$$\simeq \rho^2 \left|\tilde{G}(\Delta\vec{k}_q)\right|^2 \cdot \left| \frac{1 - e^{-\frac{L_{med}}{L_{abs}}} \cdot e^{i\frac{\pi L_{med}}{L_{coh}}}}{-\frac{\lambda_1}{2L_{abs}} + i\frac{\pi\lambda_1}{2L_{coh}}} \right|^2 \tag{3.26}$$

$$= \frac{\rho^2}{4\lambda_1^2} \left|\tilde{G}(\Delta\vec{k}_q)\right|^2 \cdot \frac{1}{\frac{\pi^2}{L_{coh}^2} + \frac{1}{L_{abs}^2}} \cdot \left[1 + e^{-2\frac{L_{med}}{L_{abs}}} - 2e^{-\frac{L_{med}}{L_{abs}}} \cdot \cos\left(\frac{\pi L_{med}}{2L_{coh}}\right)\right] \tag{3.27}$$

$$= \frac{(\rho \cdot L_{med})^2}{4\lambda_1^2} \left|\tilde{G}(\Delta\vec{k}_q)\right|^2 \cdot \frac{1}{\frac{\pi^2 L_{med}^2}{L_{coh}^2} + \frac{L_{med}^2}{L_{abs}^2}} \cdot \left[1 + e^{-2\frac{L_{med}}{L_{abs}}} - 2e^{-\frac{L_{med}}{L_{abs}}} \cdot \cos\left(\frac{\pi L_{med}}{2L_{coh}}\right)\right] \tag{3.28}$$

This is the famous formula found in Constant et al. [1999]. Interestingly, apart from the three step model response summarized in $\tilde{G}(\Delta\vec{k}_q)$, the phase matching term only depends on 4 lengths: the wavelength, the length of the medium, the coherence length and the absorption lengths, through their ratios. The two latter are influenced by all phase matching parameters introduced in the first section. Before turning to the discussion, let us examine a few limit cases.

Short medium limit

If the ratios $\frac{L_{med}}{L_{abs}} \ll 1$ and $\frac{L_{med}}{L_{coh}} \ll 1$, we are in the limit of a short medium. In this case Eq. 3.28 reduces to

$$I_q(\Delta\vec{k}_q) = \frac{(\rho \cdot L_{med})^2}{4\lambda_1^2} \left|\tilde{G}(\Delta\vec{k}_q)\right|^2 \cdot \frac{1}{\frac{\pi^2 L_{med}^2}{L_{coh}^2} + \frac{L_{med}^2}{L_{abs}^2}} \cdot 2\left[1 - \cos\left(\frac{\pi L_{med}}{2L_{coh}}\right)\right] \tag{3.29}$$

$$= \frac{(\rho \cdot L_{med})^2}{4\lambda_1^2} \left|\tilde{G}(\Delta\vec{k}_q)\right|^2 \cdot \frac{4\sin^2\left(\frac{\pi L_{med}}{2L_{coh}}\right)}{\frac{\pi^2 L_{med}^2}{L_{coh}^2} + \frac{L_{med}^2}{L_{abs}^2}} \tag{3.30}$$

$$= \frac{(\rho \cdot L_{med})^2}{4\lambda_1^2} \left|\tilde{G}(\Delta\vec{k}_q)\right|^2 \cdot \frac{1}{1 + \frac{L_{coh}^2}{\pi^2 L_{abs}^2}} \tag{3.31}$$

The intensity of the harmonics is ruled by the product of three terms:

- The single atom response $\left|\tilde{G}(\Delta\vec{k}_q)\right|^2$,

- $\frac{1}{1+\frac{L_{coh}^2}{\pi^2 L_{abs}^2}}$ which will vary little with the parameters of the experiment,
- $(\rho \cdot L_{med})^2$. If it is multiplied by the square of the transverse surface of the beam, which was supposed to be infinite (but is in the "transverse" Fourier transforms of $G(\vec{r})$), we get the "number of atoms generating" squared. In other words, the signal scales quadratically with the gas pressure or the volume of the target cell. Also, it can be equivalent to have a very dense and short target, or a long and very dilute target.

It is often given as a proof of being in the "single atom response" regime, or short medium length limit, to show a quadratic dependence of the yield with pressure.

Perfect phase matching

We consider a limit $L_{coh} \gg L_{med}, L_{abs}$ and $L_{med} \simeq L_{abs}$. The formula becomes

$$I_q(\Delta\vec{k}_q) = \frac{(\rho \cdot L_{abs})^2}{\lambda_1^2} \left|\tilde{G}(\Delta\vec{k}_q)\right|^2 \left[1 - e^{-\frac{L_{med}}{L_{abs}}}\right]^2. \tag{3.32}$$

For short media, we retrieve the quadratic variation with the medium length. For media getting longer than L_{abs}, the leading term become $(\rho \cdot L_{abs})^2$: it does not help to increase indefinitely the medium beyond the absorption length. The harmonics generated at the entrance of the medium will be in any case absorbed on their way out and will not increase the overall signal. For long enough medium, everything is like a medium "limited by the absorption length".

Non absorbing medium

We consider a limit $L_{abs} \gg L_{med}, L_{coh}$ and $L_{med} \simeq L_{coh}$. The formula can be derived almost like Eq. 3.30:

$$I_q(\Delta\vec{k}_q) = \frac{(\rho \cdot L_{med})^2}{\lambda_1^2} \left|\tilde{G}(\Delta\vec{k}_q)\right|^2 \cdot \frac{4\sin^2\left(\frac{\pi L_{med}}{2L_{coh}}\right)}{\frac{\pi^2 L_{med}^2}{L_{coh}^2}}. \tag{3.33}$$

For long media, the yield oscillates like a sinc function, alike usual formulas of phase matching in crystals. The coherence length is interpreted as the length over which the emission from the different atoms build up. If the medium is longer, the next emitters are radiating with an opposite phase compared to the first, and the yield decreases. This is the origin of this oscillatory behavior. The medium should not be longer than the coherence length.

General case

The general formula 3.28, without the atomic response, is plotted in Fig. 3.5. The interest of increasing the coherence length and the absorption length is clear, as the signal gets more intense and stable. The cut is given for L_{med}=4 mm. For an absorption length comparable to the medium length, there is no further evolution of the intensity, making an increase of the "involved atoms" through a medium length increase useless. For the coherence length we observe a stabilisation at about $L_{med}/\pi \simeq 1.3$ mm.

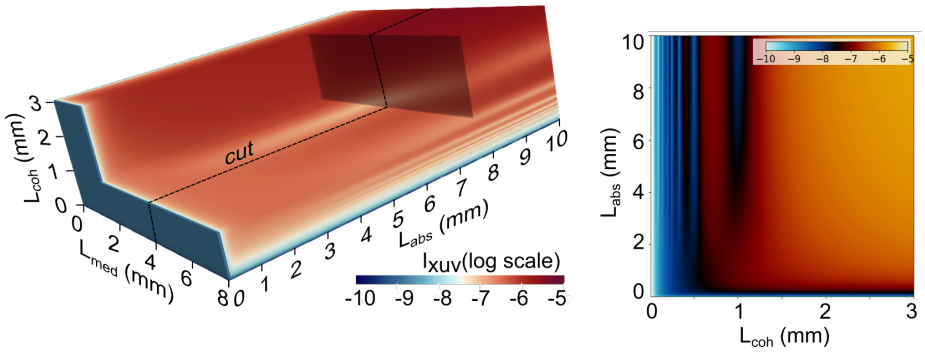

FIGURE 3.5: (left)

We can put the problem in a reverse form: for given laser intensity, focusing conditions and medium density, we get a given state of the ionization of the medium and given absorption and coherence lengths. In this case, the optimal medium length is about the absorption length and 3 times the coherence length. If we can make the coherence and absorption lengths equal, the two conditions are enforced at once.

> The coherence and absorption lengths should be maximized, i.e. phase mismatched minimized, to get the higher HHG yield.

This simple model gives very nice interpretation of phase matching. However, it is by far oversimplified: the ionization rates are not homogeneous in space, and vary in time (Figs. 3.6 & 3.7), the medium might not be uniformly dense, the laser may get reshaped as it propagates.... Full models are extremely CPU demanding, but exist. They remain tractable on personal machines only when symmetries are invoked, for instance a cylindrical symmetry of the beam. Otherwise, for a few mm long cell, the computation time can be several days on some working stations (more powerful than PC's but not supercomputers). Keeping these limitations in mind, we can still make considerations on local phase matching in a medium and extrapolate that regions of the generating medium where the coherence and absorption lengths are maximized will be those contributing the more to the macroscopic signal.

In particular, when we wrote the initial equation 3.12, we did not considered the details of the optical indices, i.e. the sources of phase slips, making up $\Delta\vec{k}_q$. If a complex

field representation reads $\mathcal{E}(t,z) = \mathcal{E}_0 e^{i(\omega t - kz + \varphi(z))}$, its phase may be approximated by

$$\omega t - kz + \varphi(z) \simeq \omega t - \left(k - \frac{\partial \varphi}{\partial z}\right) z \tag{3.34}$$

$$\simeq \omega t - (k - \delta k)\, z \tag{3.35}$$

with $\delta k = \partial\varphi/\partial z$. So any spatially varying phase may be interpreted as a change of "effective" wavevector, that should be taken into account to model phase matching. It can find its origin in the structure of the beam (e.g. Eq. (3.36)) or in space varying optical indices. In the remaining of this chapter, we will discuss such terms contributing to $\Delta\vec{k}_q$, whose contributions are small enough to sum up linearly.

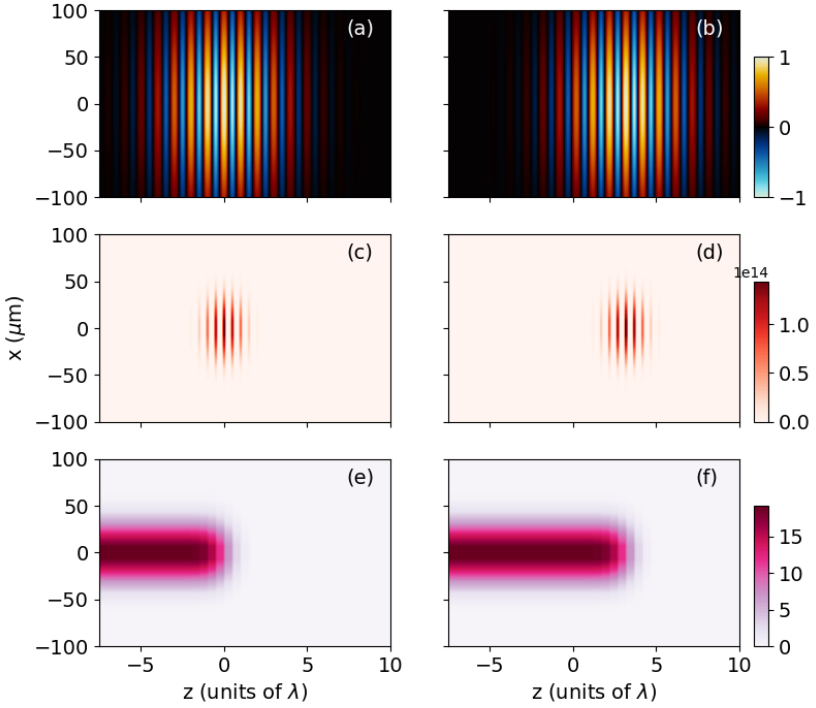

FIGURE 3.6: (a-b) Snap shots of the electric field of a 10 fs long laser pulse, 100 μm waist, at about 3 periods delay. (c-d) Instantaneous ADK ionization rates. (e-f) Ionization of the medium at this two times.

Main contributions to phase mismatch

Gouy phase

The Gouy phase of a Gaussian beam reads (with the convention $e^{i(\omega t - kz + \varphi_{Gouy})}$ for the phases).

$$\varphi_{Gouy} = arctan\left(\frac{z}{z_R}\right) \tag{3.36}$$

where

$$z_R = \frac{\pi\omega_0^2}{\lambda}. \tag{3.37}$$

with ω_0 the waist of the laser. This phase significantly varies close to the focus of the laser beam, which is precisely where we tend to position the HHG medium. The z-dependent phase may be written

$$-kz + \varphi_{Gouy} \simeq -\left(k + k_{Gouy}\right) z \tag{3.38}$$

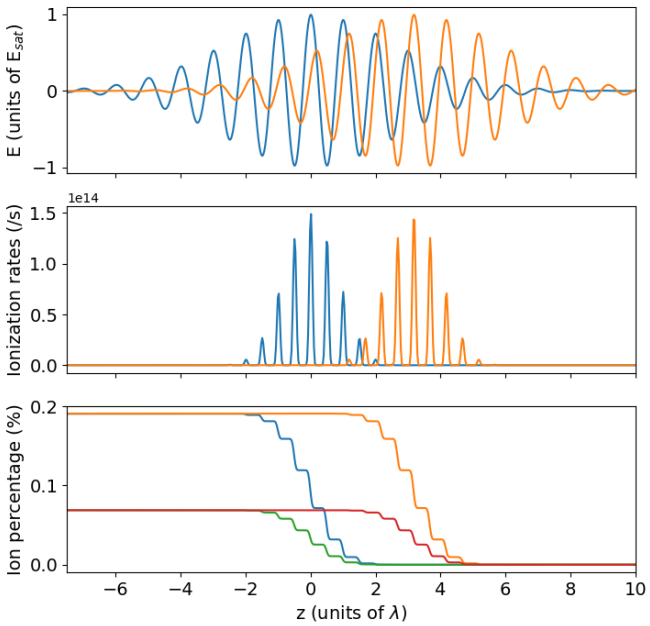

FIGURE 3.7: (top) cuts at x=0 of the electric field displayed in Fig. 3.6. (middle) Ionization rates from the ADK formula. (bottom) Integrated ionisation of the medium over time.Blue and orange: on axis, respectively at time 0 and time 0+3T. Green and red: at 25 μm off axis, same timings.

$$\text{with } k_{Gouy} = -\frac{d\varphi_{Gouy}}{dz} = -\frac{1}{1+\frac{z^2}{z_R^2}} \cdot \frac{1}{z_R} \simeq -\frac{1}{z_R} \tag{3.39}$$

This term leads to a phase matching condition (q is the harmonic order)

$$\Delta\vec{k}_{Gouy} = qk_{Gouy}(\omega_f) - k_{Gouy}(\omega_q) = -\frac{1}{z_R}(q-1)\,. \tag{3.40}$$

It is a term that is always negative. And naturally does not depend on any ionization/composition of the medium. It is all the more important as the Rayleigh length is small, i.e as the numerical aperture is large, or the beam tightly focused.

Neutral dispersion

It arises from the fact that the neutral atoms do not show the same optical indices for harmonic q and the fundamental beam. It should be noted that importantly, even if this part of the dispersion is usually not dominant, the corresponding imaginary part of the optical index, responsible for the absorption by the neutral atoms plays a very important role. The phase mismatch here reads

$$\Delta\vec{k}_n = qk_n(\omega_f) - k_n(\omega_q) = \frac{2\pi q}{\lambda_f}\left(n(\omega_f) - n(\omega_q)\right) \tag{3.41}$$

The refractive index is in general higher for the IR pulse than for the XUV field, yielding a positive contribution. Note that the index itself, for dilute gases, is proportional to the density of gas. Ionization, which depletes progressively the medium as the pulse passes thus may modify this term (see. Figs. 3.6&3.7). It is thus a dynamical term.

Electronic dispersion

It is quite common to use media that end up, after the IR pulse propagation, with an ionization of a few percent (Fig. 3.7). Some of these electrons result from the non recombining events in the 3-step model. In this case, the electronic dispersion becomes non negligible and must be taken into account. The index associated to the electrons reads

$$n_{plasma}(\omega) = \sqrt{1-\frac{\omega_p^2}{\omega^2}} \tag{3.42}$$

with the plasma frequency defined as

$$\omega_p = \sqrt{\frac{e^2 N_e}{\varepsilon_0 m_e}} \tag{3.43}$$

and N_e the electronic density. A typical target density is in the 10^{16} atoms/cm^3, which gives a plasma frequency way below usual high harmonics. A Taylor expansion thus gives

$$n_{plasma}(\omega) \simeq 1 - \frac{\omega_p^2}{2\omega^2} \tag{3.44}$$

We then get, for the phase mismatch

$$\Delta\vec{k}_e = qk_e(\omega_f) - k_e(\omega_q) = \frac{2\pi q}{\lambda_f}\left(n(\omega_f) - n(\omega_q)\right) = -\frac{2\pi q\omega_p^2}{2\lambda_f}\left(\frac{1}{\omega_f^2} - \frac{1}{q^2\omega_f^2}\right) \tag{3.45}$$

$$\Delta\vec{k}_e = -\frac{2\pi q\omega_p^2}{2\lambda_f\omega_f^2}\left(\frac{q^2-1}{q^2}\right) = -\frac{\omega_p^2}{2c\omega_f}\left(\frac{q^2-1}{q}\right) \tag{3.46}$$

This contribution is always negative. It should be noted that it linearly depends on the electrons density through ω_p^2. It thus varies spatially and temporally during the pulse.

Dipole phase

As seen above, the phase of the emitted dipole depends dramatically on the shape of the electric driving field through

$$\varphi = \omega_q t - \int_{t_i}^{t} dt\left(I_p + \left(\vec{p} + e\vec{A}(t)\right)^2/2\right) \tag{3.47}$$

An intensity dependent phase is thus added. As a first approximation (cf. Fig. 3.8) it remains linear with the intensity ($\varphi = \alpha I$) with an α coefficient negative, whose magnitude is much larger for the long trajectory than for the short. It is also very different depending on the photon energy, and on the laser wavelength. Assuming a quadratic

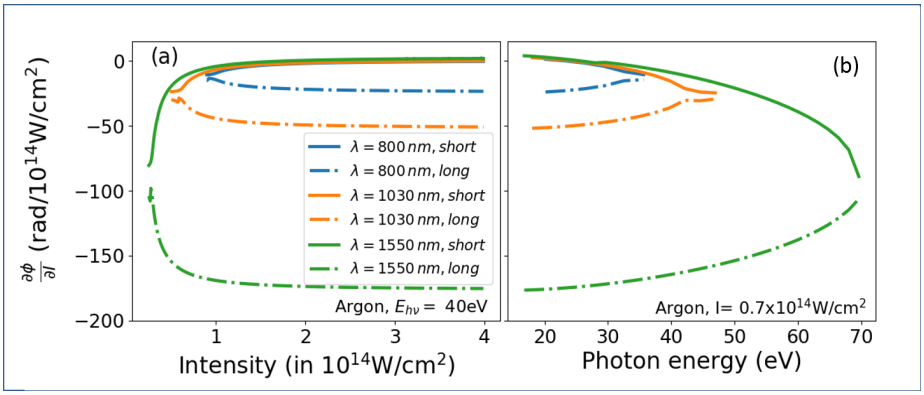

FIGURE 3.8: Dipolar phase due to variations in intensity of the pump laser, for different driving wavelengths. We note the quasi-constant value for intensities above 10^{14}W/cm^2, which is the relevant range of intensity for HHG to occur.

intensity profile of the laser in the radial direction (first-order approximation of a Gaussian), we note that this phase corresponds to that of a spherical wave: the second trajectory diverges more than the first.

Furthermore, this corresponds to an additional wave vector $-\alpha\vec{\nabla}I$ which should be considered when the condition of phase matching is written. It has both a radial and

longitudinal component. Its sign changes with the position relative to the focus. This let envision different behaviors when focusing before or after a focus.

Contribution		Sign	Depends on...
$\Delta\vec{k}_{Gouy}$	Gouy phase	< 0	focusing condition, position of the jet/cell
$\Delta\vec{k}_{n}$	Refraction index of neutral	> 0	Pressure, density, ionization level
$\Delta\vec{k}_{e}$	Refraction index of electrons	< 0	Pressure, density, ionization level
$\Delta\vec{k}_{ions}$	refraction index of ions	> 0, negligible	Pressure, density, ionization level
$\Delta\vec{k}_{at}$	HHG process phase (single atom)	< 0 for z < 0 > 0 for z> 0	local intensity, wavelength

TABLE 3.1: Phase matching components.

3.2.3 Phase matching of short and long trajectories

To give some more insight into phase matching, we here put all these contributions together, discussing the wave-vector mismatches in typical conditions. But as a preliminary remark, let us note that the ions densities are not homogeneous in space, and vary in time. This is apparent in Figure 3.6, where we calculated the ADK ionization rate for a field peaking at its saturation value in Argon. The ionization is much thinner than the beam waist, and lasting much less time. The ionization of the medium just increases as time passes, making phase matching a "dynamical" notion. In other words, if phase matching is good at some time and location in the medium, it may be poor nearby or at another time.

This is also apparent in the cuts displayed in Fig. 3.7. It shows that a non negligible fraction of the medium is ionized, reaching a few percent at least. Also, the typical steps of ionization on the leading edge are apparent, corresponding to peaks of the E-field. This points have to be kept in mind when we make general considerations about phase-matching: it all depends on time and space. However, we can still make some general remarks that are usually verified experimentally.

When putting together the phase mismatch vectors, it is observed that the phase matching condition is quite naturally observed when placing the jet after the focus (Fig. 3.9). In these conditions, the atomic phase associated to short trajectories can help compensating the Gouy phase (See Table 3.1). On the contrary, when placing the jet before the focus, it is extremely hard to phase match the harmonics on axis (Fig. 3.9). However, these can be phase matched off-axis. In this case, the wavevector associated to the atomic phase, which is proportional to the gradient of the intensity, is not collinear and harmonics are emitted off axis.

All these effects depend on the location of the gas jet with respect to the focus, the density of the gas medium, the nature of the gas, the intensity of the laser.... In particular, we can see stringent effects in Fig. 3.10, where only the pressure is changed. Either the long trajectories are phase matched off-axis, giving strong outer rings, or the short one on axis, giving strong central spot. For applications, this situation is often priviledged. Also, we can note that harmonics are not always at integral harmonic orders, as discussed in Sec. 3.1.

It should be finally noted finally, that, in general, the HHG process clamps to efficiencies of about $10^{-5} - 10^{-6}$ with a λ =800 nm laser; due to both phase matching and single atom response. Smart combination of gas cell/fiber/jet and laser parameters are still actively studied to increase this yield.

In a laboratory, you will often see more experienced persons optimizing an HHG source by changing the size of an iris placed on the beam driving HHG. The HHG spectrum will most likely dramatically change with little variations of the iris. What is changing when you act on such an iris? Plenty of parameters. First, the amount of

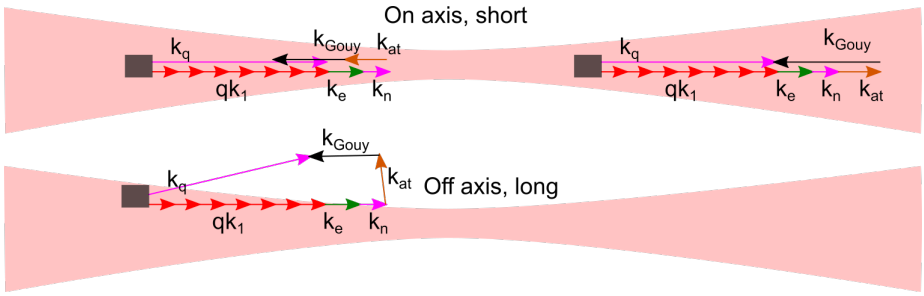

FIGURE 3.9: Sum of wavevectors to assess good phase matching. Top: we consider two locations, on opposite sides of the focus (a fraction of the Rayleigh range), on axis, and a small atomic phase corresponding to the short trajectory. Bottom: we consider a large atomic contribution, off axis, corresponding to the long trajectory.

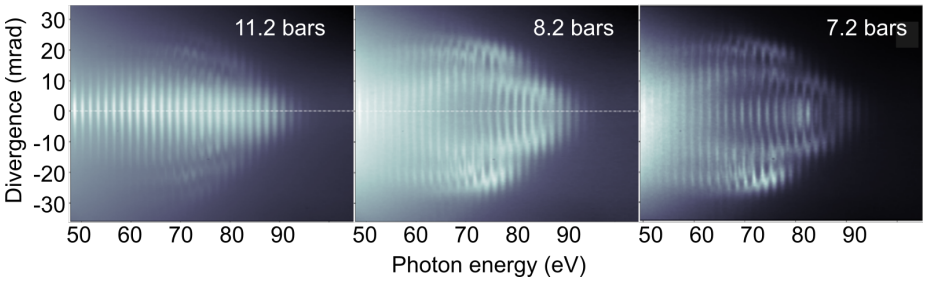

FIGURE 3.10: HHG spectra recorded on a source fed by a λ=1550 nm laser, for different backing pressure of the gas jet. The grating acts as a cylindrical lens: the vertical dimension is not focused, while the horizontal one is, and spread upon wavelength.

energy coupled in the experiment changes, so the peak intensity as well. And the cutoff law states that the cutoff should change. But you also change the numerical aperture of the beam, so the diameter of the focus. Again, this changes the peak intensity. But it also changes the wavefront curvature in the neighborhood of the focus, where the gas target is positioned. So the divergence of the HHG should change. You also change the ionization rates. So phase matching is altered, and the shape of the spectrum may change. In particular, with too large an iris, you may see "messy" harmonics profiles, which is a signature of a too high ionization rate that make phase matching uneven in the medium ("overdriven" regime). You also change the Gouy phase, and so the related phase matching term…HHG is thus a multiparameters problem, and it may be sometimes difficult to find an overall optimum of generation, while local optima may be found.

As an exercise, you may carry out the same analysis for i) a scan of the focusing lens position, ii) a change of its focal length, iii) a change of the laser's compressor settings, iv) a change of generating gas or any parameter that is available in your own setup…

3.3 Summary of chapter 3

- The periodicity in time of HHG, which occurs every half cycles, leads to a spectral structure primarily taking the form of a comb of odd harmonics of the fundamental. It gets a continuous spectrum when only one half cycle generates XUV light.
- Time-variation of phases during the driving laser pulse may shift the harmonic comb, making the rule of "odd harmonics only" not very strict.
- To get a macroscopic signal, contributions from various atoms should be summed up. The sum is optimal when all contributions have the same phase. This is generally not the case. A phase mismatch exists.
- Phase matching terms include the geometry of the beam, but also the driving intensity, the duration of the beam, and the nature of the gas. In particular in highly depends on the ion/electron densities at a certain point and time. These densities vary in time and space as the driving pulse progresses through the medium, making phase matching a "dynamical" notion for HHG.

CHAPTER 4

ATTOSECOND PULSE MEASUREMENT

4.1 Introduction to temporal measurements

Due to the high frequency of the electric field of light pulses, all sensors used to detect them are integrating over time (e.g. photodiodes, micro channels plates (MCP), XUV cameras…). To get the temporal profiles of light pulses, the measurement chain must then include at least one non-stationary filter and one stationary filter in order to slice them temporally. As a counter-example, let us consider an autocorrelator used in the visible range (Fig. 4.1). Two replica of the pulse to be characterized are delayed by τ and overlapped in a nonlinear medium (usually a doubling crystal). They create a signal (second harmonic) which reads

$$I(\tau) = \int_{-\infty}^{+\infty} dt\, |\mathcal{E}(t) + \mathcal{E}(t-\tau)|^2 \tag{4.1}$$

$$= 2\int_{-\infty}^{+\infty} dt\, |I(t)| + 2\int_{-\infty}^{+\infty} dt\, \left[\mathcal{E}(t)\mathcal{E}^*(t-\tau)\right] \tag{4.2}$$

This signal highly depends on the temporal overlap of the two replica of the pulse. The filter is therefore non-stationary. However, this kind of measurement does not give

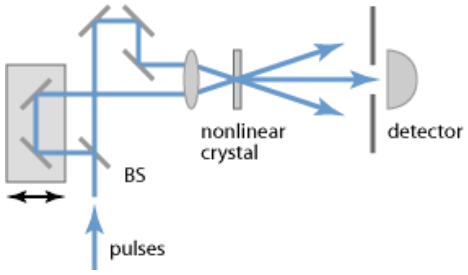

FIGURE 4.1: Principle of an intensity autocorrelator. Copied from www.rp-photonics.com.

access to the spectral phase of the pulse. Indeed, the interference term in Eq. 4.2 reads

$$\int_{-\infty}^{+\infty} dt \left[\mathcal{E}(t)\mathcal{E}^*(t-\tau)\right] = \int_{-\infty}^{+\infty} dt \left[\mathcal{E}(t)\cdot\left(\mathcal{E}^*(t)\otimes\delta(t-\tau)\right)\right] \tag{4.3}$$

$$= \int_{-\infty}^{+\infty} d\omega \left[\tilde{\mathcal{E}}(\omega)\tilde{\mathcal{E}}^*(\omega)e^{i\omega\tau}\right] \tag{4.4}$$

$$= \int_{-\infty}^{+\infty} d\omega \left|\tilde{\mathcal{E}}(\omega)\right|^2 \cdot e^{i\omega\tau} \tag{4.5}$$

No spectral phase is measured, so the temporal profile cannot be deduced. However, it yields the spectrum, and, assuming a certain shape of the pulse, the duration can be estimated.

> An autocorrelation technique is not able to determine the temporal profile of an unknown arbitrary pulse. In the best case, it gives the duration if the pulse's shape is preliminary known.

To get the actual spectral phase of a pulse, and hence its temporal shape, refined autocorrelation techniques, putting at play **modified replica** of the pulse to be characterized, are required. Two main approaches, FROG and SPIDER techniques, are currently used in the visible/IR domain.

RABBIT and FROG-CRAB, which for what?

We will first detail the SPIDER technique which was adapted to the attosecond domain giving the RABBIT technique, and second the FROG technique which was adapted to the attosecond domain, giving the FROG-CRAB technique[1]. They are both based on a cross correlation of the attosecond pulse to be measured and a side laser pulse called **"dressing beam"**, which are overlapped in a photoionizing target gas. This gas plays the role of the non-linear medium. The first method, RABBIT, is very popular to

[1]This genealogy may be questioned by some authors who prefer to make a parallel between RABBIT and FROG. For an introductory lecture, we adopted this convenient version.

measure attosecond pulse trains while the second is used to retrieve any attosecond pulse structure, including single attosecond pulses. It is remarkable that the setups for both techniques are almost the same, but for a change of intensity of the dressing beam. It is much higher for FROG-CRAB than RABBIT: $10^{10\text{-}11}$W/cm^2 for RABBIT, 10^{13}W/cm^2 for FROG-CRAB.

> RABBIT uses a weak dressing field and measures attosecond pulse trains; FROG-CRAB (or streaking) use a stronger dressing field, and is able to retrieve single attosecond pulses.

RABBIT and FROG-CRAB to study photoionization?

These approaches were first developped to access the temporal profiles of attosecond pulses. However, instead of deducing the laser pulse properties from the gas photoionization signal, **the point of view can be reversed to investigate the properties of the gas, if the pulses are characterized beforehand**. So understanding the temporal characterization method is also extremely useful to understand a wealth of applications, in particular the investigations of photoionization time delays. The measurement consists in timing the arrival time of electrons on a detector, after ionization by a single XUV photon. The presence of the potential of the ion, that may be undergoing some dynamical rearrangement, and the energy of the electron, affect the time the electron takes to escape. It is an extremely vivid and active field of research nowadays.

One of the emblematic measurement of such delays was first carried out with FROG-CRAB in Neon gas (Schultze et al. [2010]). Theoretical predictions over almost ten years could not accurately predict the exact values measured, while the trend was there. This discrepancy was finally resolved in 2017 by repeating the experiment with the RABBIT technique (Isinger et al. [2017]). It was shown that the strong dressing field required for FROG-CRAB was slightly altering the results. Understanding carefuly the characterization methods is thus extremely important.

4.2 Reminder about SPIDER

SPIDER is an acronym for Spectral Phase Interferometry for Direct Electric-Field Reconstruction.

The principle of SPIDER is to create two replicas of the pulse to be characterized and compare, two by two its spectral components through interferences between the replicas (Fig. 4.2). Let us consider a pulse to be characterized which electric field reads $\mathcal{E}(t)$ and $\mathcal{E}(\omega)$ in the temporal and spectral domains. Two replicas of it are prepared, and delayed by a time τ, reading $\mathcal{E}_1(t) = \mathcal{E}(t)$ and $\mathcal{E}_2(t) = \mathcal{E}(t-\tau) = \mathcal{E}_1(t) \otimes \delta(t-\tau)$. The corresponding fields in the spectral domain thus read $\mathcal{E}_1(\omega)$ and $\mathcal{E}_2(\omega) = \mathcal{E}_1(\omega)e^{i\omega\tau}$. Moreover, we have at hand a highly chirped pulse in the same frequency domain $\mathcal{E}_3(\omega)$. Both replicas are mixed with the elongated pulse $\mathcal{E}_3(\omega)$ in a doubling crystal. Due to the delay τ, the two replicas mix up with different part of the chirped pulse, hence with different frequencies. The doubled spectra obtained are thus slightly shifted spectrally, by a quantity Ω. Apart from this shift, they are just copies of one another and thus read

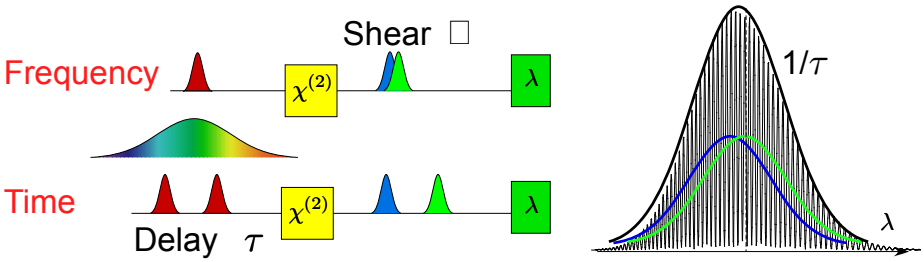

FIGURE 4.2: Principle of the SPIDER technique. The frequency components of the pulse to be characterized are compared in pairs in the spectral domain.

$\mathcal{E}'_1(\omega)$ and $\mathcal{E}'_2(\omega) = \mathcal{E}'_1(\omega-\Omega)e^{i\omega\tau}$. These two quasi doubled replicas are brought to interfere on an optical spectrometer. For sake of demonstration, let us first consider that the delay is zero. The total signal at a given frequency in the spectrometer, which is the coherent sum of the two corresponding doubled frequency components of the replica reads

$$\left|\mathcal{E}'_1(\omega)+\mathcal{E}'_1(\omega-\Omega)\right|^2 = \left|\mathcal{E}'_1(\omega)\right|^2 + \left|\mathcal{E}'_1(\omega-\Omega)\right|^2 + 2\left|\mathcal{E}'_1(\omega)\right|\cdot\left|\mathcal{E}'_1(\omega-\Omega)\right|\cdot\cos\left[\phi(\omega)-\phi(\omega-\Omega)\right]. \quad (4.6)$$

It can be maximum or minimum depending on the relative phase of the two components involved. This reads out on the spectrum envelope which may show a bump or a dip. In principle, just comparing the envelope of the sum of the pulses to the direct spectrum of one replica is enough to get an approximation of the spectral phase derivative $\frac{\partial\varphi(\omega)}{\partial\omega}$.

However, the spectra are usually not very regular, making this determination cumbersome. If we now consider that the delay is non zero, a modulation of the interference pattern will appear and make the phase differences show up on a carrier frequency.

$$\begin{aligned} S(\omega) &= \left|\mathcal{E}_1(\omega)+\mathcal{E}_1(\omega-\Omega)e^{i\omega\tau}\right|^2 \quad (4.7)\\ &= I(\omega)+I(\omega-\Omega)+\sqrt{I(\omega)I(\omega-\Omega)}\cos\left(\phi(\omega)-\phi(\omega-\Omega)+\omega\tau\right)\end{aligned}$$

The spectrum is now modulated with the "frequency" τ, and the phase of these fringes gives an approximation of $\frac{\partial\varphi(\omega)}{\partial\omega}$. Since the measurement of the spectrum is straightforward, this is exactly what is needed to retrieve the pulse temporal profile. The technique relates to the Lock-In detection technique, in which the signal of interest is "sent" on a carrier frequency, in a spectral range in which the noise density is reduced.

4.3 Attosecond pulse measurements with RABBIT

The previous technique is difficult – if not impossible, to implement in the XUV domain. Indeed it requires

1. To prepare replicas, which is most conveniently achieved using amplitude beamsplitters

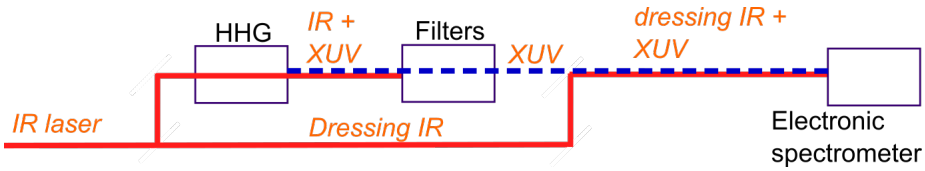

FIGURE 4.3: Principle of the RABBIT measurement. The main laser is split in two, a weak part employed for the dressing (bottom) and a more intense part (top) used for HHG. Once HHG is done, the remaining of the driving IR laser beam is filtered out. In a final step, the two beams, XUV and dressing IR are recombined and focused in an electronic spectrometer. Several variants of this principle exist. In particular, the two beams, dressing and driving beams can be made collinear before the HHG chamber, reducing the lengths of the arms of the interferometer. However, this asks for "tricks" to remove the remaining driving laser. A popular method is to use an annular beam for HHG: at focus it will show an almost Gaussian profile, generating XUV on axis, while in the far field it will recover its annular shape, making its filtering easy with a simple iris. This method was implemented in the original paper about RABBIT (Paul et al. [2001]). Other methods playing on time delays may also be implemented.

2. To have non linear crystals,

3. To have high enough a flux to induce non linear effects.

In the XUV domain, neither beamsplitters, nor non linear crystals exist. And HHG flux remain usually modest. The turn around for these difficulties is to make a cross correlation between the XUV pulse to be characterized and an IR synchronous field in a gas target (Fig. 4.3). The non linear medium is here a well known atomic gas that gets ionized by the attosecond XUV field. More precisely, the Strong Field Approximation formalism may be used to describe the measurement. The probability to get an ionized electron with energy ω when the two fields (XUV and IR) are present with a delay τ reads

$$a(\vec{p}_f, \tau) = -i \int_{-\infty}^{\infty} dt\ \vec{d}\left(\vec{p}_f + e\vec{A}(t)\right) \cdot \vec{\mathcal{E}}_{xuv}(t-\tau) e^{i\frac{S(t,\tau,\vec{p})}{\hbar}} \tag{4.8}$$

with

$$S(t, \tau, \vec{p}) = \int_{t_i}^{\infty} dt \left(I_p + \left(\vec{p} + \vec{A}(t)\right)^2 /2\right) \tag{4.9}$$

As for HHG, this expression has a straightforward interpretation in two steps: dipole transition to a continuum state at time t, and second, a phase modulation of the electronic wave packet emitted by the infrared field. The latter is just given by the action integral phase accumulated by the electron with energy $I_p + E_k$.

To make it clear, let us first consider that the IR field is zero. In that case we get

$$S = I_p t + \frac{v^2}{2m} t \tag{4.10}$$

$$a(\vec{p}_f, \tau) = \mathcal{F}(\vec{d}.\vec{\mathcal{E}}_{xuv}(t)) \simeq \mathcal{F}(\vec{\mathcal{E}}_{xuv}(t)) \tag{4.11}$$

where the later approximation considers a flat cross section of the ionizing gas. The electronic distribution is here simply a copy of the XUV spectrum. This is the principle of an electron spectrometer (see Sec. 4.4).

We now consider the case when the dressing IR field is also present. The vector potential associated to this field may be approximated by

$$\vec{A} = \vec{A}_0(t) \cdot \cos(\omega_L t).$$

The phase in Eq. (4.9) gets modulated as:

$$e^{i\frac{S(t,\tau,\vec{p})}{\hbar}} = e^{\frac{i}{\hbar}\left(I_p + \frac{p_f^2}{2m}\right)t} e^{i\phi_{IR}(\vec{p}_f,t)} \tag{4.12}$$

with

$$\phi_{IR}(\vec{p}_f,t,z) = -\frac{1}{2m\hbar}\int_t^\infty dt' \left(2e\vec{p}_f \cdot \vec{A}(t',z) + e^2\vec{A}(t',z)^2\right) \tag{4.13}$$

$$= -\frac{1}{2m\hbar}\int_t^\infty dt' \left(2e\vec{p}_f \cdot \vec{A}_0(t) \cdot \cos(\omega_L t) + \frac{e^2\vec{A}_0^2(t)}{2} \cdot \left[\cos(2\omega_L t) + 1\right]\right) \tag{4.14}$$

If the envelope $\vec{A}_0(t)$ varies slowly compared to the laser angular frequency ω_L, i.e

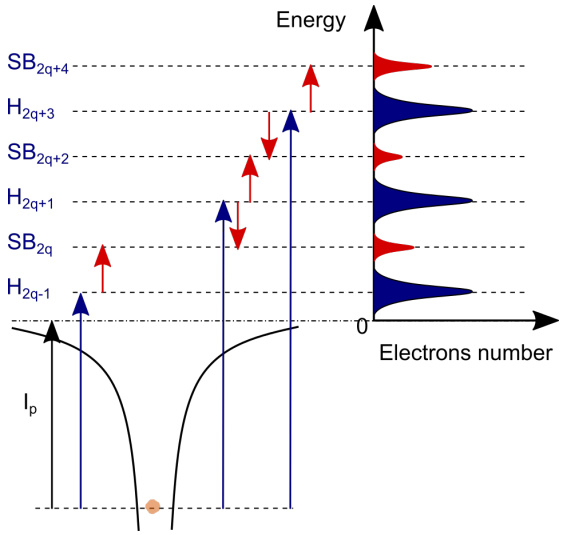

FIGURE 4.4: Photoelectron spectrum ionized by a comb of odd harmonics of a fundamental laser, in the presence of an infrared "dressing" field with the same frequency as the fundamental laser beam. In blue: main harmonics lines, in red: sidebands.

$\partial\vec{A}_0(t)/\partial t \ll \vec{A}_0(t)\omega_L/2\pi$, it can be integrated by part, yielding, for the first term on

the right hand side:

$$\phi^1_{IR}(\vec{p}_f,t,z) = -\frac{e\vec{p}_f}{m\hbar}\left(\left[\vec{A}_0(t)\cdot\frac{\sin(\omega_L t)}{\omega_L}\right]_t^\infty - \int_t^\infty dt'\frac{\partial\vec{A}_0(t)}{\partial t}\cdot\frac{\sin(\omega_L t)}{\omega_L}\right)$$
$$\simeq \frac{e\vec{p}_f}{m\hbar\omega_L}\vec{A}_0(t)\sin(\omega_L t)\hat{=}\varphi^{(1)}\cdot\sin(\omega_L t). \quad (4.15)$$

where we have used the slowly varying enveloppe approximation to neglect the second term, and, for the first term upper bond, the fact that at infinite time, the pulse is gone and the vector potential is zero. Proceeding with the second terms on the right hand side of Eq. (4.14), we will get a term linear in t (integration of a constant), which will just sum up with the other ones isolated in Eq. (4.12); and a term oscillating at the second harmonic, denoted $\varphi^2\cdot\sin(2\omega_L t)$[2]. This phase modulation thus reads

$$\phi_{IR}(\vec{p}_f,t,z) = \varphi^0(\vec{p}_f,t,z)+\varphi^{(1)}(\vec{p}_f,t,z)\cdot\sin(\omega_L t)+\varphi^{(2)}(\vec{p}_f,t,z)\cdot\sin(2\omega_L t). \quad (4.16)$$

with

$$\varphi^0(\vec{p}_f,t,z) = \frac{i}{\hbar}\left(I_p+\frac{p_f^2}{2m}+\frac{e^2\vec{A}_0^2(t)}{4m}\right)t \quad (4.17)$$

When entered in Eq. (4.8), the two last terms will modify the Fourier transform, making sidebands appear. We will make use of the Jacobi-Anger expansion (Wikipedia link):

$$e^{iz\sin(\omega t)} = \sum_{-\infty}^{\infty} J_n(z)e^{in\omega t}. \quad (4.18)$$

where z is the modulation depth, which in our case is set by the amplitude of the "dressing" IR field. We thus have, in Eq. (4.8)

$$e^{i\frac{S(t,\tau,\vec{p})}{\hbar}} = e^{i\varphi^{(0)}(\vec{p}_f,t,z)}\cdot e^{i\varphi^{(1)}(\vec{p}_f,t,z)\cdot\sin(\omega_L t)}\cdot e^{i\varphi^{(2)}(\vec{p}_f,t,z)\cdot\sin(2\omega_L t)} \quad (4.19)$$
$$= e^{i\varphi^{(0)}(\vec{p}_f,t,z)}\cdot$$
$$\sum_{-\infty}^{\infty} J_n\left(\varphi^{(1)}(\vec{p}_f,t,z)\right)e^{in\omega t}\cdot\sum_{-\infty}^{\infty} J_n\left(\varphi^{(2)}(\vec{p}_f,t,z)\right)e^{i2n\omega t} \quad (4.20)$$

The amplitudes of $\varphi^{(1)}(\vec{p}_f,t,z)$ and $\varphi^{(2)}(\vec{p}_f,t,z)$ are ruled by the magnitude of the vector potential, the former varying linearly, the latter quadratically with A_0. We set this value small, i.e. we make the dressing beam not very intense, so that $\varphi^{(1)}(\vec{p}_f,t,z)\ll 1$ and $\varphi^{(2)}(\vec{p}_f,t,z)\ll 1$. About the origin, the Bessel functions are just decreasing with n; their value being close to one for J_0, close to zero for $n\neq 0$. We can thus cut the Taylor expansion in Eq. (4.20) at its first positive and negative terms. Due to $\varphi^{(1)}(\vec{p}_f,t,z)$, the action integral in Eq. (4.10) is thus modified as

$$S = I_p t+\frac{v^2}{2m}t\pm\omega_L t. \quad (4.21)$$

[2]The full calculation which is a bit technical is available in http://dx.doi.org/10.1051/uvx/201301014.

where we have neglected the $A^{(2)}(t)$ term compared to I_p and $v^2/2m$. The amplitude of these Taylor expansion terms are rules by $J_{\pm 1}\left(\varphi^{(1)}(\vec{p}_f, t, z)\right)$. Along the terminology used in Frequency Modulation radio (FM), they are call **sidebands**. In the remaining of this paragraph, we will show that the spectral phase of an harmonic comb can be read out of the intensity of these sidebands.

Let us consider that we have a comb of harmonics generated through HHG, with angular frequencies $\omega_{2q+1} = (2q+1)\omega_L$ where ω_L is the angular frequency of the driving laser, $\mathcal{E}^0_{2q+1}$ being its amplitude and φ_{2q+1} its spectral phase. The electric field of harmonic $2q+1$ thus reads

$$\mathcal{E}^0_{2q+1} e^{i(2q+1)\omega_L t + i\varphi_{2q+1}}. \tag{4.22}$$

In Eq. (4.8), taking into account Eq. (4.21), we thus have a phase varying like

$$\Psi^{\pm}_{2q+1}(t,\tau) = I_p t + \frac{v^2}{2m} t \pm \omega_L t + (2q+1)\omega_L(t-\tau) + \varphi_{2q+1}, \tag{4.23}$$

where we have taken into account the fact the the leading E-field is $\mathcal{E}(t-\tau$. The oscillating terms have $2q\omega_L$ and $(2q+2)\omega_L$ periodicities, with a phase φ_{2q+1}. The amplitude of these terms will be proportional to $|d.\mathcal{E}^0_{2q+1}|$. The same derivation for harmonic $2q-1$ would give sidebands at frequencies $(2q-2)\omega_L$ and $2q\omega_L$. We thus have two contributions reaching the $2q\omega_L$ component: either issued from harmonic 2q-1 or 2q+1. These two electron wave packet interfere. The reasoning developed for the SPIDER technique applies: if the two neighboring harmonics are in phase, this sideband should be strong. On the contrary, if they are out of phase, it should be zero. In summary, alike in SPIDER, by shearing the spectrum we make neighboring spectral components "talk" to one another and get in a position to retrieve their relative phase through interferences. The phase difference between two pathways leading to SB 2q reads

$$\Psi^{\pm}_{2q+1}(t,\tau) - \Psi^{\pm}_{2q-1}(t,\tau) = 2\omega_L\tau + \varphi_{2q+1} - \varphi_{2q-1}. \tag{4.24}$$

The intensity of the sideband reads

$$I^{2q}_{sb} \propto I_{2q-1} + I_{2q+1} + \sqrt{I_{2q+1} I_{2q-1}} \cos\left(2\omega_L\tau + \varphi_{2q+1} - \varphi_{2q-1}\right) \tag{4.25}$$

with I_{2q+1}, I_{2q-1} the intensities of the neighboring harmonics. Alike spider again, temporal fringes may be introduced by scanning the delay τ between the IR and the XUV attosecond beam, easing the determination of the phase.

An exemple of a RABBIT trace (Reconstruction of attosecond beating by interference of two photon transitions) is shown in Fig. 4.5. The sidebands are clearly identified due to their oscillations. The position of the min/max of successive sidebands informs on the relative phase of the interfering harmonics.

It should be noted that

1. It is only valid when there are only odd harmonics of the fundamental
2. It measures an average pulse in the train. Indeed, all half cycles add up to form the total signal.

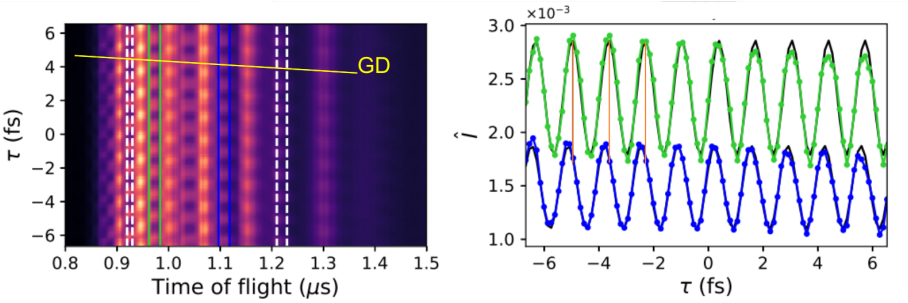

FIGURE 4.5: (left) Example of a RABBIT trace. Abscissa is the time of flight of photoelectrons collected in a TOF-MBES, the vertical axis is the delay between the XUV beam and the "dressing" IR beam. The most intense lines correspond to harmonics while weaker oscillating ones are sidebands (for instance between the green and blue cursors). We can notice that the peaks are unevenly spaced. This is due to the square root law between energy of the electrons and Time of flight (See Eq. (4.26) below). Harmonics are also oscillating (not described in the text), but out of phase with the sidebands. It can be simply interpreted as a depletion of harmonics line to populate sidebands: when its neighboring SB are high, an harmonic line is weak and *vice versa*. The phases of the SB are progressively shifting, as apparent with the yellow line pointing their maximum. This is reminiscent of a lack of synchronization of the harmonics (Group delay dispersion, Fig. 2.9). (right) Lineouts of two sidebands. We observe a very sinusoidal oscillation, whose phase depends on the selected SB. The orange lines show the systematic dephasing on a few periods. The phase of the oscillation, together with the spectral amplitude, allow to reconstruct temporal profiles, such as those displayed in Fig. 5.6. HHG and detection were both performed in Argon, on ATTOLAB FAB10 laser, LIDYL laboratory, CEA-Saclay.

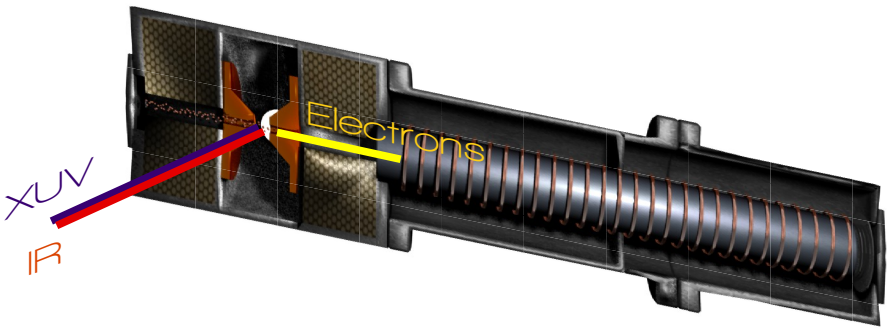

FIGURE 4.6: Sketch of a Time-of-Flight Magnetic Bottle Electron Spectrometer.

This technique is widely spread in the community. It has the great advantage to be quite straightforward to implement, quick and require a low "dressing" energy. It is becoming fairly common with 1D electronic spectrometers (see below) while remaining challenging with 3D detectors requiring long acquisition times over which the interferometric stability should be preserved. Due to the limitations enumerated above, it is not universal. In particular, it does not work for single attosecond pulses. In that case, a variant of the FROG technique is usually implemented.

4.4 Parenthesis on electronic detectors

A standard way to implement this technique is to use a Time-of-Flight Magnetic Bottle Electron Spectrometer (TOF-MBES, see Fig. 4.6). It is composed of a sensitive region (left in Fig. 4.6) where a high magnetic field ($\simeq 1$ T) exists and where some gas is injected (usually a noble gas). The XUV field will ionize this gas. The emitted electrons, which can fill a 4π sr solid angle, are collected by the magnetic field and driven through a hole in a flight tube. There is a smooth transition from the region with a high magnetic field towards this flight tube where a low magnetic field is set. Guided by the magnetic field, the electrons then fly away over a distance L, which, depending on the required spectral resolution, ranges from tens of centimeters to meters. Finally these electrons are detected on a micro channel plate detector with a nanosecond time resolution. Considering a gas with an ionization potential I_p and an XUV photon with energy E_{XUV}, the electrons leave the high field region with a kinetic energy $E_k = E_{XUV} - I_p$. They will therefore take a time

$$t = \frac{L}{\sqrt{\frac{2E_k}{m}}} \tag{4.26}$$

to reach the detector, where m is the electron mass. In practice the arrival times span a few hundred nanoseconds to a few microseconds for meter long TOF and few tens of eV of photon energy. It can thus be resolved by fast acquisition card/oscilloscopes having a

GHz band pass. Recording the amount of electrons versus time gives a measurement of the number of XUV photons vs. energy, provided the ionization cross section is known. This is called a 1D detector, as it gives a spectral intensity vs. Energy.

2D detectors, in which two components of the momentum of the electron are resolved are also widely used. They are called Velocity Map Imaging Spectrometers (VMI, or VMIS). In that case the collection of the electrons is ensured by strong electric fields (kV applied on electrodes a few cm apart). 3D detectors, in which all three components of the momentum are measured also exist. They are called COLTRIMS (COLd Target Recoil Ion Momentum Spectrometer). They are firstly based on electrodes as well, but additional weak magnetic fields may be used in some configurations, to enhance the collection efficiency. The main advantage of these detectors is that, under proper operation mode, and if a dissociating process is investigated in which the linear recoil approximation is valid, one may get all momenta coordinates of both the ion and electron, including the initial orientation of the molecule before ionization. In this operation mode, the main disadvantage of these detectors is that they can only detect one electron per laser pulse, making them attractive mainly on high rep-rate lasers (above 5 kHz at least). But when used, they give much more information than 1D or 2D detectors about the photoionization process.

4.5 Reminder about FROG

FROG is an acronym for "Frequency Resolved Optical Gating". The principle is the gating of the pulse to be characterized ($\mathcal{E}(t)$) by a delayed field ($g(t-\tau)$). In its most intuitive version, $g(t-\tau)$ is a proper amplitude gate, that slices $\mathcal{E}(t)$ in little portions that will be spectrally resolved. Such a spectrum is recorded for a series of time delays τ and we finally get a 2D-map:

$$I(\tau,\omega) \propto \left| \int_{-\infty}^{\infty} dt \mathcal{E}(t) \cdot g(t-\tau) e^{-i\omega t} \right|^2 \tag{4.27}$$

We may note that the gate should not be too narrow. In the limit case in which $g(t) = \delta(t)$ Eq. (4.27) yields

$$I(\tau,\omega) \propto \left| \int_{-\infty}^{\infty} dt \mathcal{E}(t) \cdot \delta(t-\tau) e^{-i\omega t} \right|^2 = |\mathcal{E}(\tau)|^2 . \tag{4.28}$$

The signal does not depend on the spectral phase, and the pulse profile cannot be determined. Indeed, as already stated earlier, the point behind any spectral phase measurement is to get the different spectral components to "talk" to one another, i.e. to interfere with one another. In the FROG technique, it is the Fourier transform that plays this role: it mixes up different spectral components; provided the gate has selected several of them. In the case when the gate is extremely narrow as treated in Eqs. (4.28), only one component is selected and thereby not brought to interfere with any other by the Fourier transform. It is thus reasonable that no temporal information is finally retrieved. At variance with SPIDER, it should be notice that here many spectral components are

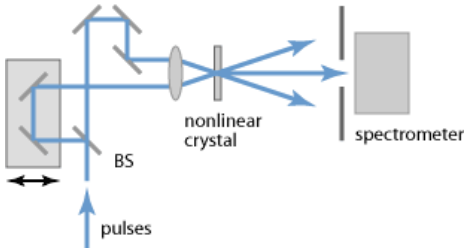

FIGURE 4.7: Principle of a frog measurement. Copied from www.rp-photonics.com.

mixed at once with the Fourier transform, while it is only two for the SPIDER. This makes the retrieval more complicated for FROG than for SPIDER.

For a FROG to work, the gate should be long enough to select several components. One very popular gate is the pulse itself, squared and the autocorrelation in Eq. (4.27) is performed using a 3rd order non linearity. The intensity then reads

$$I(\tau,\omega) \propto \left| \int_{-\infty}^{\infty} dt \mathcal{E}_{sig}(t,\tau) e^{-i\omega t} \right|^2 \tag{4.29}$$

with

$$\mathcal{E}_{sig}(t,\tau) = \mathcal{E}(t) \cdot |\mathcal{E}(t-\tau)|^2 . \tag{4.30}$$

Introducing the Fourier transform of $\mathcal{E}_{sig}(t,\tau)$ along τ:

$$\mathcal{E}_{sig}(t,\tau) = \int_{-\infty}^{\infty} d\Omega \tilde{\mathcal{E}}_{sig}(t,\Omega) e^{-i\Omega\tau} \tag{4.31}$$

we get

$$I(\tau,\omega) \propto \left| \int_{-\infty}^{\infty} \int_{-\infty}^{\infty} d\Omega \, dt \tilde{\mathcal{E}}_{sig}(t,\Omega) e^{-i\omega t - i\Omega\tau} \right|^2 . \tag{4.32}$$

This is nothing but a double Fourier transform of $\tilde{\mathcal{E}}_{sig}(t,\Omega)$ for which we only measure the amplitude squared. Fortunately algorithms exist to solve this equation known as 2D-phase retrieval problem. At first glance, it may appear surprising that the underlying phase may be retrieved out of an intensity map. The point is that the information is here highly redundant. The inputs are two 1D fields, i.e. 2n points, if the discretization is performed over n temporal points while the FROG map may be $n \times n$ points. The optimization algorithm thus searches for a solution best fitting all these autocorrelations at once and the solution is usually unique[3] These algorithms may run on reasonably sized desk computers, implementing for instance the PCGPA (Principle Componenent Generalized Projections Algorithm) algorithm. It takes a few tens of Python/Matlab lines for the core of the algorithm. However, the preliminary conditioning of the signal can be more demanding!

[3]The similarity between this problem and Coherent diffraction imaging is striking: in both cases, whereas only amplitudes are retrieve in 2D, one is able to reconstruct both the phase and the amplitude of the underlying field.

We thus consider that, with such an algorithm, we have retrieved $\tilde{\mathcal{E}}_{sig}(t,\Omega)$. Retrieving $\mathcal{E}(t)$ is then straightforward:

$$\begin{aligned}
\tilde{\mathcal{E}}_{sig}(t,\Omega) &= \int_{-\infty}^{\infty} d\tau \mathcal{E}_{sig}(t,\tau) e^{i\Omega\tau} && (4.33)\\
&= \int_{-\infty}^{\infty} d\tau \mathcal{E}(t)\cdot g(t-\tau) e^{i\Omega\tau} && (4.34)\\
&= \mathcal{E}(t)\cdot \int_{-\infty}^{\infty} d\tau g(t-\tau) e^{i\Omega\tau} && (4.35)\\
&= \mathcal{E}(t)\cdot G(\Omega) e^{i\Omega t} && (4.36)
\end{aligned}$$

with

$$G(\Omega) = \int_{-\infty}^{\infty} d\tau g(\tau) e^{i\Omega\tau} \quad (4.37)$$

We thus have

$$\mathcal{E}(t) = \frac{\tilde{\mathcal{E}}_{sig}(t,0)}{G(0)} \quad (4.38)$$

Interestingly the gate needs not be an amplitude gate, but can also be a phase gate. The point is that it should simply multiply the signal to be determined by a non stationary value. For the attosecond version, it is a phase gate that is used.

4.6 Attosecond pulse measurements with the FROG-CRAB technique

FROG-CRAB means "Frequency Resolved Optical Gating for Complete Reconstruction of Attosecond Beatings". It was proposed in CEA-Saclay by Yann Mairesse and Fabien Quéré. In the literature, it may also appear as the "streaking" technique, which has been employed very early, in particular by the group of Vienna (now Garching) to measure the first isolated, or single attosecond pulses in 2001[4]. The principle is a FROG, but applied in the XUV domain. The setup is the same as for RABBIT. Inspecting Eq. (4.8) it is clear that the spectrum measured through the cross correlation is a FROG trace, where the phase is modulated. The standard retrival algorithm may thus be applied. This FROG-CRAB technique presents several advantages:

1. It reconstructs the actual pulse or series of pulses profile(s) (not a mean pulse),
2. It also works with continuous spectra, thus for isolated pulses.

Exemple of FROG-CRAB spectrograms are shown in Fig. 4.8. On the left, the dressing pulse is probably 5 to 7 femtosecond long. Both on the left and right extremities (delays $= \pm 6$ fs) we observe a continuous spectrum centered around 70 eV. This is the central wavelength of the attosecond pulse. Now, when the IR beam arrives it may completely

[4] A discussion may arise upon the fact that streaking does not use exactly the same analysis approach as FROG-CRAB. However, the principles of the measurements are very similar.

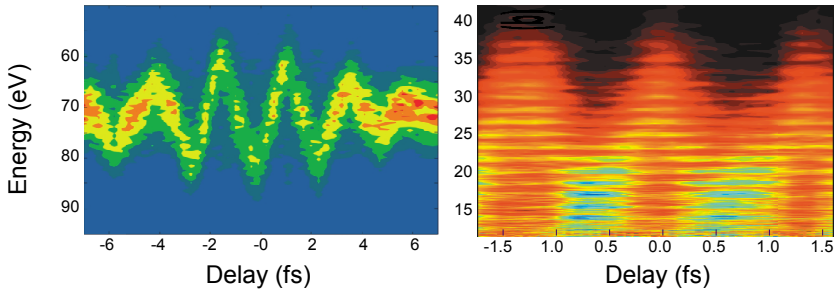

FIGURE 4.8: Exemple of cross correlation traces (FROG-CRAB traces) in the case of a single attosecond pulse (left) and a train of attosecond pulses (right). (Adapted from Schultze et al. [2007] and Johnsson et al. [2005] respectively).

deplete the spectrum and shift it up or down depending on its phase with respect to the IR. This may be interpreted as a RABBIT at very high IR intensities. The large value of the IR intensity allows the creation of sidebands with high orders (almost a 10 eV shift is observed). However, the description with the RABBIT formalism becomes cumbersome and it is preferable to use the description proposed by Quéré & Mairesse: the photoionization frees an electron in the continuum which is then submitted to the remaining IR electric field. Alike what we used for the 3-step model describing HHG, the Newton equation of movement may be written, taking advantage of the large value of the A-field to neglect the ionic core. It gives:

$$\frac{d\vec{p}}{dt} = e\vec{\mathcal{E}} = -e\frac{\partial\vec{A}}{dt} \tag{4.39}$$

which leads, once integrated and taking into account that at infinite times the field is zero to

$$\vec{p}_f = \vec{p}_i + e\vec{A}(t_i) \tag{4.40}$$

A certain energy (momentum) distribution of electrons at time of ionization is just shifted in the spectral domain by a value equal to the vector potential *at the time of ionization*. This is illustrated in Fig. 4.9. So what we see in Fig. 4.8 is just the oscillation of the electrons momentum linked to the changing value of the potential vector at the time of ionization when the delay is scanned. It is also reminiscent of the dressing IR pulse profile. This streaking of the spectrum can be processed to retrieve the pulse profile using standard FROG algorithms. On the right of the figure the same technique is applied to a train of attosecond pulses. Here the harmonic structure remains apparent. It is just superimposed to the streaking pattern.

These two techniques, RABBIT and FROG-CRAB are, by far, the most widely spread ones to measure temporal profiles of attosecond pulses. However, they both have limited validity domains and a significant amount of work is currently done to extend them into more powerful techniques.

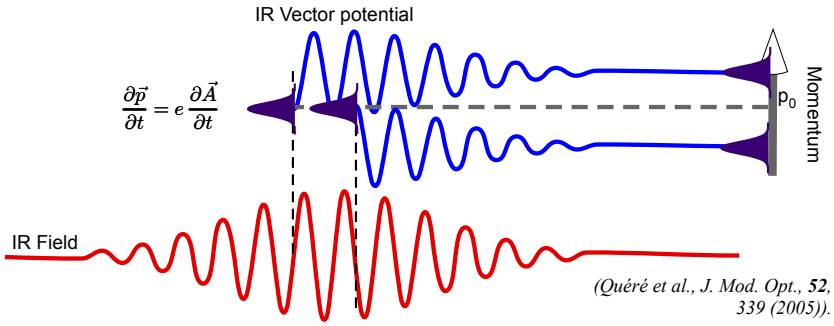

FIGURE 4.9: Trajectories in momentum space of electron wave packets injected in the continuum at different times during the IR field.

CHAPTER 5

A FEW ATTOSECOND SOURCES

5.1 Introduction

The number of laboratories operating attosecond light sources based on HHG is continuously growing worldwide. Some commercial solutions are just becoming available now, but most of them are tailor made ones, for specific applications. We could not list all their specifities and originalities. However, we will list a few of them to illustrate a few general principles about making such sources, and reinvest the knowledges of Chapters 2&3. Their specificity can be characterized by their

- duration (shape of the spectrum plus spectral phase)
- central frequency
- short or long train, single attosecond pulse, repetition rate, polarization...
- Flux.

The control means are

- the target
- the pump beam (energy, λ, polarization...)
- the periodicity of the pump
- the duration of the pump

5.2 Sources based on ultrashort lasers (3-10 fs)

Nowadays, ultrashort lasers may reach durations of 1-2 optical cycles, may it be around 800 nm (T=2.7 fs) or in the MidIR range ($\simeq 1.5-2\mu$m, T=5-8 fs). With these durations becoming comparable to the electric field period, an important parameter comes in the game: the carrier envelope phase (CEP, Fig. 5.1). Indeed, it is clear that the number

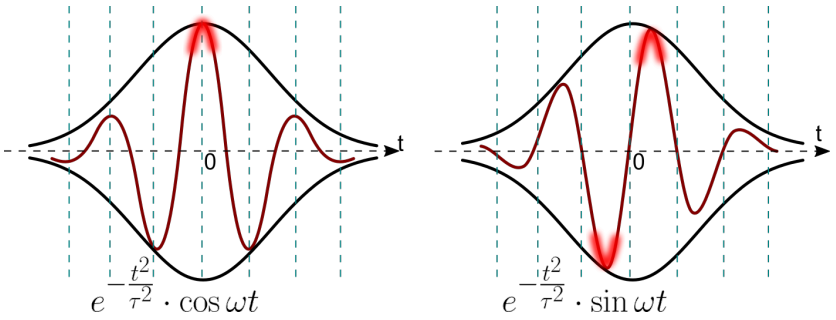

FIGURE 5.1: Two ultrashort pulses with carrier envelope phases shifted by $\pi/2$. The black line is the enveloppe of the pulse, identical for both. The red line is the electric field. The red blurred zones are the single extremum of the cosine field, and the two extrema of the sine field.

of equivalent maxima, and their value changes dramatically while changing the CEP with such ultra short pulses. In the first case, the tunnel ionization may occur just once, while it may occur equivalently twice in the other case. This results in the emission of one or two attosecond pulses depending on the CEP.

An example of attosecond pulses generated with such an ultrashort laser is displayed in Fig. 5.2. First, it must be noticed that the spectrum is almost continuous (see Sec. 3.1). However, it may be noticed that there are a few residual modulations on the spectrum. This is probably the remaining of a second little attosecond pulse that is not completely killed by the decrease of the field during one half cycle. In other words, this is the remaining of the harmonic structure that is obtained with long driving pulses.

Getting hands on so short lasers is nothing easy. In particular, keeping a stable CEP during dozens of minutes remains a technical challenge that is solved today in just a few laboratories worldwide, at least at the level of energy required for HHG. To lift the requirements on the duration of the laser while keeping the generation of a single attosecond pulse, several techniques have been demonstrated. Instead of playing on the first step of the model (ionization step), the popular polarization gating technique acts on the second step (excursion in the continuum). The point is to tailor the field so that the electronic wavepacket (EWP) is not driven back to the ionic core during any half cycles but one. This is achieved by making the polarization of the IR field variable in time: it starts circular, gets shortly linear in the middle of the pulse and ends circular again. Naturally, when the electric field is circular the EWP is driven away from the core and does not recollide. To shape the pulse in such a way, the most common approach is to play on the difference between the group and phase velocity of waves in birefringent

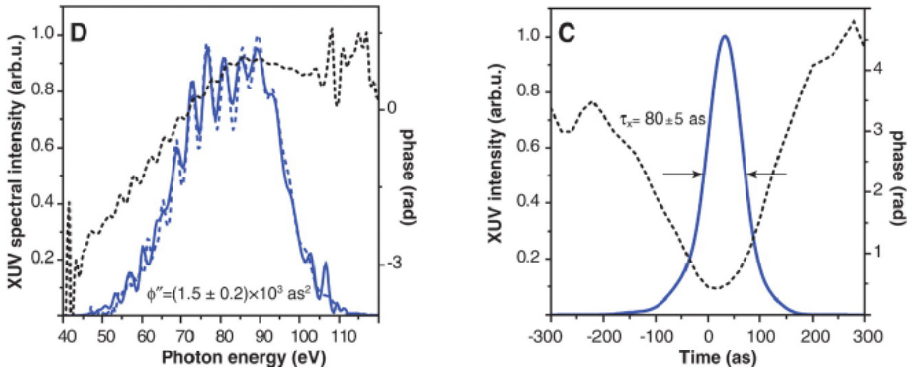

FIGURE 5.2: Exemple of single attosecond pulse obtained in Garching (Germany), filtering with a zirconium filter Goulielmakis et al. [2008]. Is that a cosine or sine driving pulse ?

crystals (Chap. 1).

Propagation of an ultrashort pulse in a transparent birefringent crystal

Let us consider an ultrashort gaussian laser pulse which electric field reads

$$\vec{\mathcal{E}}(t) = \vec{\mathcal{E}}_0 e^{-\sigma^2 t^2} e^{i\omega_0 t}. \tag{5.1}$$

We further consider a birefringent plate of thickness d, with indices for the ordinary and extraordinary axis given by n_o and n_e. We will use the neutral axis of the crystal as a reference frame and denote $\mathcal{E}_o(t)$ (resp. $\mathcal{E}_e(t)$) the projection of $\vec{\mathcal{E}}(t)$ on these axis. The field once propagated through this plate writes

$$\mathcal{E}_o(t) = \mathcal{E}_0 e^{-\sigma^2 (t - d/v_o^g)^2} e^{i\omega_0 (t - n_o d/c)} \tag{5.2}$$

$$\mathcal{E}_e(t) = \mathcal{E}_0 e^{-\sigma^2 (t - d/v_e^g)^2} e^{i\omega_0 (t - n_e d/c)} \tag{5.3}$$

with the group velocity given, for the two orthogonally polarized components

$$v_{e,o}^g = \frac{c}{n_{e,o}(\omega) - \omega \frac{\partial n_{e,o}}{\partial \omega}} \tag{5.4}$$

It should be noticed that we have taken into account a phase velocity (given by the optical index) that is not the same as the group velocity (altered by its derivative) (see Sec. 1.3.1). If the thickness is very large, the two real exponential have no overlap, and we will have a temporal separation of the two orthogonally polarized components. The initial single pulse is split in two pulses, delayed from one another and linearly polarized at 90 degrees from one another. If the thickness goes to zero, naturally nothing happens: the pulse remains linearly polarized and single.

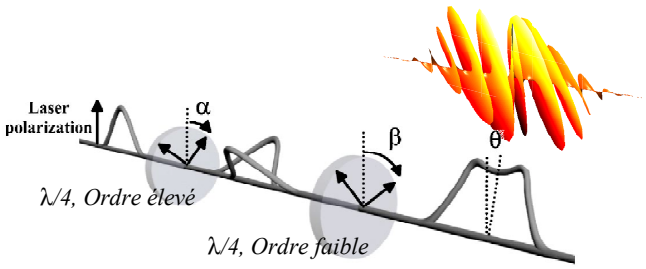

FIGURE 5.3: Principle of polarization gating

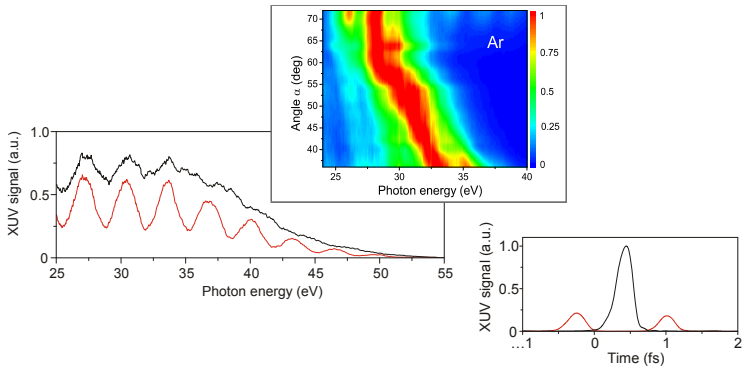

FIGURE 5.4: Attosecond pulses obtained in Milan using a polarization gate (aluminum filter), adapted from G Sansone and Nisoli [2008].

In between these two extreme cases, the two pulses overlap. If in addition the thickness corresponds to a dephasing between the two axis of half a period (thick quarter wave plate), the polarization is linear, getting gradually circular during the temporal overlap, and finally linear again. To get to the right combination, a second thin quarter wave plate shifts this to circular, linear and circular again. Although fairly ancient (late 90's), this proposition was only tested successfuly in 2006 by a consortium putting together Milan and Bordeaux's groups. Their results are reproduced in Fig. 5.4. It shows that

1. There is a large spectral tunability

2. The CEP remains important, and allows to go from one to two pulses, i.e. an almost continuous spectrum to a fringed spectrum,

3. One may get a single attosecond pulse in the plateau, where XUV fluxes are higher.

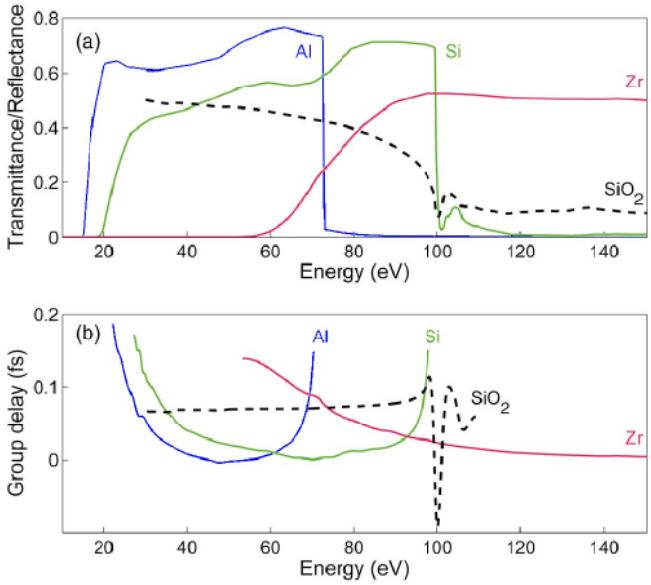

FIGURE 5.5: Examples of complex transmittances of metallic filters used in attosecond physics (From Gustafsson et al. [2007]).

5.3 Sources based on long laser pulses (20-50 fs)

Without any further filtering (and this is also true for attosecond pulses issued from short lasers described in Sec. 5.5.2) the spectra are naturally dominated by their low energy parts: third, fifth, seventh harmonics which are generated in the perturbative regime are usually way more intense than the HHG part of the spectrum. The duration of these harmonics will be femtosecond and longer. It is thus crucial to filter out these harmonics to get an attosecond pulse. One very standard way to achieve this function is to use metallic foils placed on the beam. These usually have a thickness of a hundred to a few hundreds nanometers, making them exaggeratedly fragile. The transmittance of a few common filters is reported in Fig. 5.5. They show a "cut on" in a range going from 15 eV to 60 eV, perfectly suited to filter out the low order harmonics while keeping those from the plateau. In addition, due to usual Kramers-Kronig relations, right after the "cut on" the dispersion shows a negative group delay. This is exactly opposite to the natural group delay of the harmonics, induced by the excursion in the continuum (Fig. 2.9). These filters can thereby also fulfill a second function: compressing temporally the pulses. An exemple of such a compression is shown in Fig. 5.6 for a spectrum generated in argon filtered by an aluminum filter. On the same laser, now generating in neon and using a zirconium filter, one may obtain the completely different pulse displayed in Fig. 5.7. The basis spectrum is naturally larger (see chapter 2), allowing more tuning opportunities. In conclusion, using metallic filters, one may

1. Adjust the spectral band,

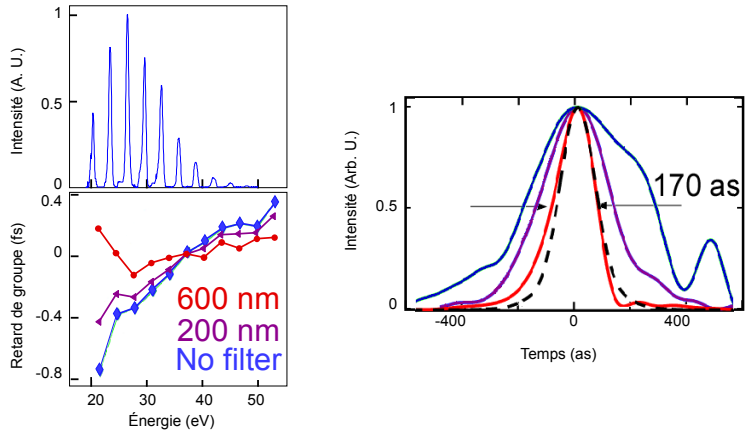

FIGURE 5.6: (left) Spectrum and group delay for a harmonic radiation unfiltered or filtered by increasing aluminum thicknesses. (right) corresponding time profiles (from López-Martens et al. [2005]).

2. Adjust the group delay.

It may be noted that this group delay control may also be achieved by XUV chirp mirrors. For instance the group of Franck Delmotte and Sébastien De Rossi at Institut d'Optique could design mirrors with a reflectivity higher than 10 % compensating for half of the group delay of a typical Argon harmonic source (see Fig. 5.8). This hold great promises. Indeed, the mirrors are made of alternating layers of several materials

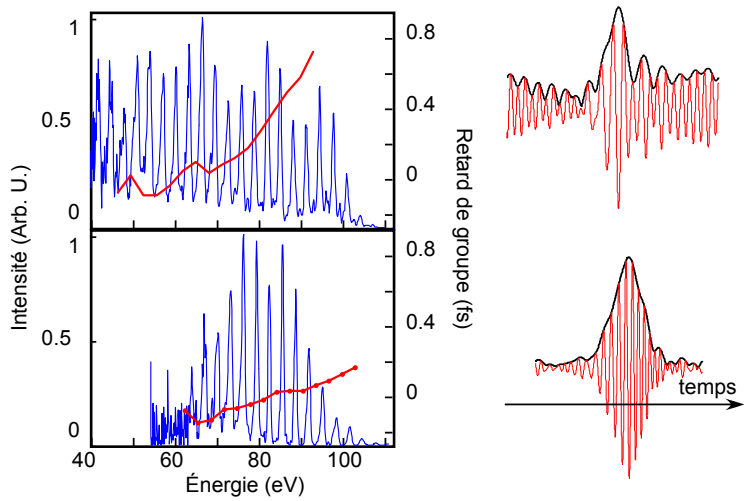

FIGURE 5.7: (top) unfiltered harmonic radiation. (down) After passing through a zirconium filter (from Gustafsson et al. [2007]).

with optimized thicknesses to fill a given target function. Varying the thickness and the nature of the material may completely change the mirrors properties, allowing to really "tune" a mirror to a given source. It is much more flexible than the metallic foils that are not tunable at all.

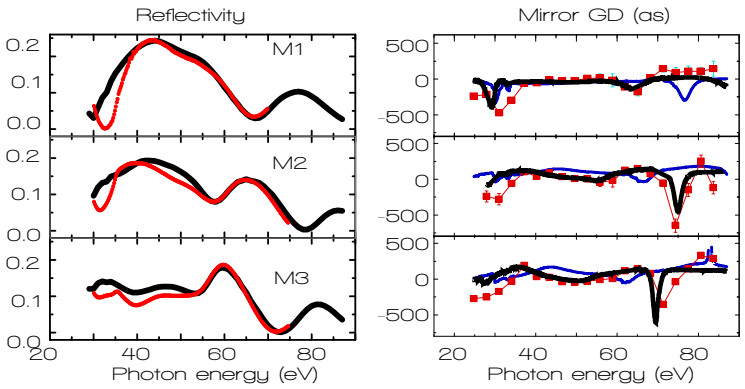

FIGURE 5.8: (left) reflectivities of three attosecond mirrors calculated and deposited at Institut d'Optique in Palaiseau (France). (Right) Group delay calculated and measured on these mirrors (adapted from Bourassin-Bouchet et al. [2011].

The use of filters is however simple and straightforward. Placed in front of an HHG source it yields right away an attosecond pulse train ready for use.

5.4 Sources with non typical shapes

In this section, we will describe a few non conventionnal harmonic sources. In particular, we will see how one can generate even harmonics together with the odd ones, how one can make circularly polarized HHG sources, and finally, how one can separate angularly the successive beamlets emitted from each half cycle of the source.

5.4.1 Source with even harmonics

The first question that may be asked is: even harmonics, what for? The answer is fairly straightforward when thinking about streaking experiments (see Fig. 4.9). Apart from Magnetic Bottle Time of Flight spectrometers, which just give the kinetic energy distribution of electrons, other detectors resolve the electronic momentum in 2D or 3D (Sec. 4.4). In that case, when dressing the electrons with an IR field, it is noticed (Fig. 4.9) that the electrons are directed towards opposite directions every other cycle. In particular, if one wants to study the rescattering of the electron on the ionic core, the image is somewhat blurred due to the superposition of these two electron wave packets evolving in opposite directions. To avoid this situation, a source with one attosecond pulse per laser period would be ideal. It corresponds to having both odd and even harmonics.

It may also be interesting to have odd and even harmonics when a denser harmonic comb helps targeting specific spectral regions. For instance, Iron shows a resonance

around 52.8 eV, which is often used to deduce the magnetic state of the sample. It is 3 eV wide. It may be completely missed by an odd harmonic comb from a Ti:Sapphire laser which has harmonics spaced by $\simeq 3$ eV.

As a side effect, it may be beneficial to gate the attosecond emission: if the periodicity is now T instead of T/2 in standard cases, the pulse duration required to get a single attosecond pulse gets longer. Say instead of requiring a 4 fs laser pulse, it can now be roughly 7 fs. Combining that with the polarization gating technique, Chang and collaborators could even demonstrate single attosecond pulses starting from 20 fs laser pulses. Several good reasons can thus justify efforts to get odd and even harmonics from an HHG source.

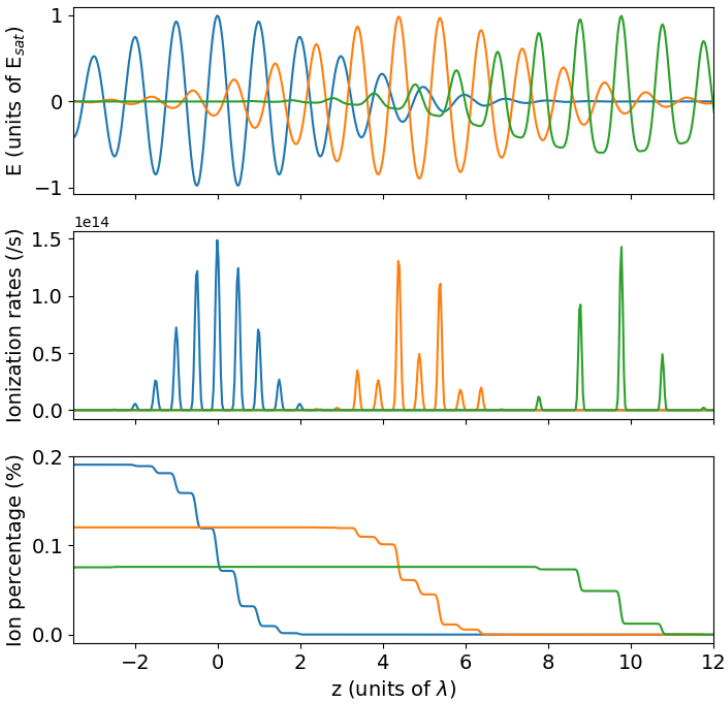

FIGURE 5.9: (top) Electric field of a light pulse with a Gaussian envelope, a wavelength λ =800 nm, a duration of 10 fs and a peak amplitude E_{sat} of Argon (blue). (orange) Same, but with an amplitude 0.95 E_{sat}, and the superposition of the second harmonic at λ =400 nm with an amplitude 0.05 E_{sat}, same duration. (green) Same as orange, but with amplitudes of respectively 0.8 E_{sat} and 0.2 E_{sat}. The fields are offset horizontally for sake of clarity. (middle) Corresponding ionization rates, computed with the ADK formula. (Bottom) Corresponding ionization ratios.

The usual approach to get odd and even harmonics is to play on the ionization step. Superimposing to the main laser beam, a second beam with much less energy but twice its frequency, every other half cycle the extremum may be lowered (Fig. 5.9). The tunnel ionization is thus killed and the attosecond emission occurs just once per cycle. Exemples of HHG spectra obtained with such a field are shown in Fig. 5.10. The temporal structure of such sources could be confirmed using FROG-CRAB/Streaking experiments. Indeed, RABBIT is inapplicable due to the presence of even harmonics where SB should sit, or at the price of a more convolved analysis. Streaking traces clearly show that the periodicity of the spectrum modulation is now T, and not $T/2$, as it is the case when only odd harmonics are present (Fig. 5.11).

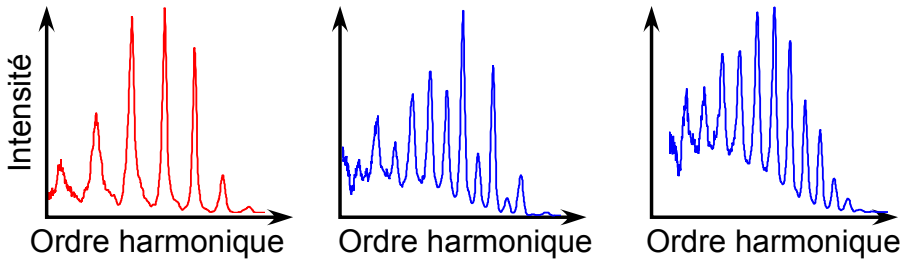

FIGURE 5.10: HHG spectra obtained with (left) a 35 fs pulse centered at 800 nm (middle and right) the same pulse on which is superimposed a fraction of second harmonic (400 nm) for two different 800 nm / 400 nm phases (Spectra from Lund University, Sweden).

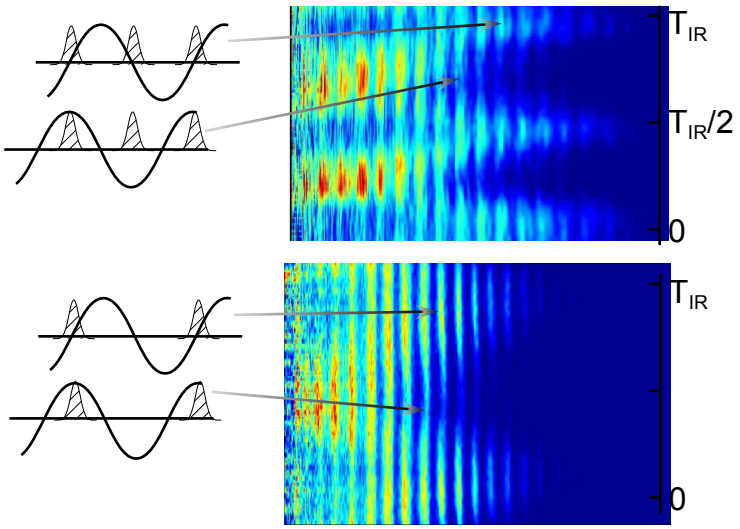

FIGURE 5.11: "Streaking" traces obtained with (top) and without (bottom) the second harmonic present in the generation laser.

Finally, it should be noted that adding a second field at another frequency is not the only way to dissymetrize the system and get both odd and even harmonics. Using an anistropic generating method is another alternative. In particular, this was recently investigated in gas jet of oriented little molecules to probe their dynamics under strong fields.

5.4.2 Circularly polarized harmonic sources

We have already seen that the direction of emission of HHG is govern by phase matching terms, that are firstly determined by the wavevector of the main driving beam about its focus. In brief, $\vec{k}_q \simeq q\vec{k}_1$ Now, if instead of using a single beam to generate harmonics, we use two non collinear beams of equal intensities and wavelengths crossing in the gas target, in which directions are the harmonics emitted? The answer may be given writing down the total field, neglecting the envelopes of the two crossing beams. We write $\vec{k}_1$ and $\vec{k}_2$ the wave vectors of the two beams, and ω their common angular frequency. They are linearly polarized along x. At a certain time and position $\vec{r}$ in the medium, the total electric field reads:

$$\mathcal{E}_x(\vec{r},t) = \mathcal{E}_1 e^{i\omega t - i\vec{k}_1\cdot\vec{r}} + \mathcal{E}_1 e^{i\omega t - i\vec{k}_2\cdot\vec{r}} \tag{5.5}$$

$$= \mathcal{E}_1 e^{i\omega t - i\frac{\vec{k}_1+\vec{k}_2}{2}\cdot\vec{r}} \left(e^{-i\frac{\vec{k}_1-\vec{k}_2}{2}\cdot\vec{r}} + e^{i\frac{\vec{k}_1-\vec{k}_2}{2}\cdot\vec{r}} \right) \tag{5.6}$$

$$= \mathcal{E}_1 e^{i\omega t - i\frac{\vec{k}_1+\vec{k}_2}{2}\cdot\vec{r}} \cos\left(\frac{\vec{k}_1 - \vec{k}_2}{2} \cdot \vec{r} \right) \tag{5.7}$$

The wavefront is given by the plane orthogonal to $\vec{k}_t = \frac{\vec{k}_1+\vec{k}_2}{2}$, while the intensity is modulated as $\cos\left(\frac{\vec{k}_1-\vec{k}_2}{2} \cdot \vec{r} \right)$. At first sight, the emission should be directed along $\vec{k}_t$. However, the appearance of an intensity modulation creates an amplitude grating. Along the transverse direction $\Delta\vec{k} = \frac{\vec{k}_1-\vec{k}_2}{2}$, we observe zones of high intensities, generating harmonics, and zones of low intensity, not generating anything. Like a regular grating, these different sources will interfere in the distance and about the main direction $\vec{k}_t$, we will observe secondary peaks corresponding to the successive diffraction orders of the grating. In general, many orders may be lit on.

Now, what if the two beams are circularly polarized, with opposite helicities? The same equations may be written for the two orthogonal linear polarizations separately, taking into account the dephasing of the components. For instance, we consider the x components to be in phase. The above equation is identical for this component. The y component of the left circularly beam is $\pi/2$ ahead of phase, while the second is lagging $\pi/2$ behind. So for the total y component, we have

$$\mathcal{E}_y(\vec{r},t) = \mathcal{E}_1 e^{i\omega t - i\vec{k}_1\cdot\vec{r} + \frac{\pi}{2}} + \mathcal{E}_1 e^{i\omega t - i\vec{k}_2\cdot\vec{r} - \frac{\pi}{2}} \tag{5.8}$$

$$= \mathcal{E}_1 e^{i\omega t - i\frac{\vec{k}_1+\vec{k}_2}{2}\cdot\vec{r}} \sin\left(\frac{\vec{k}_1 - \vec{k}_2}{2} \cdot \vec{r} \right) \tag{5.9}$$

The vectorial electric field thus reads

$$\vec{\mathcal{E}}(\vec{r},t) = \mathcal{E}_1 e^{i\omega t - i\frac{\vec{k}_1+\vec{k}_2}{2}\cdot\vec{r}} \cdot \begin{pmatrix} \cos\left(\Delta\vec{k}\cdot\vec{r}\right) \\ \sin\left(\Delta\vec{k}\cdot\vec{r}\right) \end{pmatrix} \tag{5.10}$$

The total field thus have a wavefront orthogonal to $\vec{k}_t$, and is linearly polarized. However, its linear polarization progressively goes from x to y direction as we progress in the medium along $\Delta\vec{k}$. Its intensity, given by $|\vec{\mathcal{E}}(\vec{r},t)|^2$ is the same everywhere. HHG will be just as efficient at any location in the medium. We write the amplitude of harmonic q $\mathcal{E}_q e^{iq\omega t - iq\frac{\vec{k}_1+\vec{k}_2}{2}\cdot\vec{r}}$. Its polarization, following that of the driving laser, will progressively turn. We thus have in the near field, close to focus, an XUV electric field reading

$$\vec{\mathcal{E}}_{XUV}(\vec{r},t) = \mathcal{E}_{XUV} e^{iq\omega t - iq\frac{\vec{k}_1+\vec{k}_2}{2}\cdot\vec{r}} \cdot \begin{pmatrix} \cos\left(\Delta\vec{k}\cdot\vec{r}\right) \\ \sin\left(\Delta\vec{k}\cdot\vec{r}\right) \end{pmatrix} \tag{5.11}$$

$$= \frac{\mathcal{E}_{XUV}}{2} e^{iq\omega t - iq\frac{\vec{k}_1+\vec{k}_2}{2}\cdot\vec{r}} \cdot \begin{pmatrix} e^{i\Delta\vec{k}\cdot\vec{r}} + e^{-i\Delta\vec{k}\cdot\vec{r}} \\ \frac{1}{i}\left(e^{i\Delta\vec{k}\cdot\vec{r}} - e^{-i\Delta\vec{k}\cdot\vec{r}}\right) \end{pmatrix} \tag{5.12}$$

The distribution of the far field is given by the Fourier transform of this near field

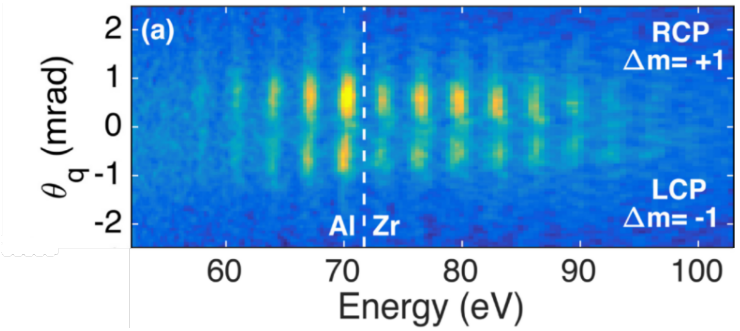

FIGURE 5.12: Spatially resolved spectrum generated with two non collinear beams. The vertical axis is the spatial dimension, the horizontal is the photon energy. Two series of harmonics are observed, propagating either above, or below the mean direction defined by $\frac{\vec{k}_1+\vec{k}_2}{2}$. These two series of dots show opposite helicities. (Adapted from Ellis et al. [2017])

(Fresnel propagation). Writing z the distance to the far field, and r' the coordinate on

this observation screen, we will thus have

$$\vec{\mathcal{E}}_{XUV}^{\text{far-field}}(\vec{r'},t) = \mathcal{E}_{XUV}e^{iq\omega t}\cdot\begin{pmatrix} \delta\left(\left(q\frac{\vec{k}_1+\vec{k}_2}{2}+\Delta\vec{k}\right)-\frac{qr'}{\lambda z}\right)+\delta\left(\left(q\frac{\vec{k}_1+\vec{k}_2}{2}-\Delta\vec{k}\right)-\frac{qr'}{\lambda z}\right) \\ -\frac{1}{i}\delta\left(\left(q\frac{\vec{k}_1+\vec{k}_2}{2}+\Delta\vec{k}\right)-\frac{qr'}{\lambda z}\right)+\frac{1}{i}\delta\left(\left(q\frac{\vec{k}_1+\vec{k}_2}{2}-\Delta\vec{k}\right)-\frac{qr'}{\lambda z}\right)\end{pmatrix} \tag{5.13}$$

$$= \mathcal{E}_{XUV}e^{iq\omega t}\cdot\delta\left[\left(q\frac{\vec{k}_1+\vec{k}_2}{2}+\Delta\vec{k}\right)-\frac{qr'}{\lambda z}\right]\begin{pmatrix}1\\ i\end{pmatrix} \tag{5.14}$$

$$+\mathcal{E}_{XUV}e^{iq\omega t}\cdot\delta\left[\left(q\frac{\vec{k}_1+\vec{k}_2}{2}-\Delta\vec{k}\right)-\frac{qr'}{\lambda z}\right]\begin{pmatrix}1\\ -i\end{pmatrix} \tag{5.15}$$

We will thus have in the far field two spots, offset about the mean wavefront $q\frac{\vec{k}_1+\vec{k}_2}{2}$, with opposite circular polarization. This scheme was implemented successfully by Ellis et al. [2017] (Fig. 5.12). In particular, the two harmonics of opposite helicities are progressively getting closer to one another as q increases, in agreement with Eq. (5.15). Variations with different colors, non perfectly equal fields, or collinear fields exist [1]

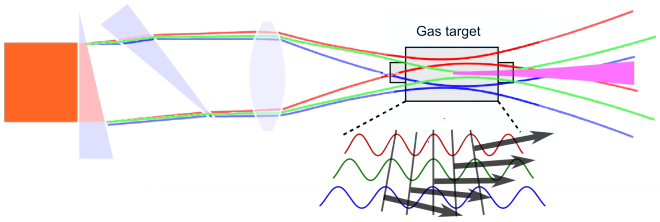

FIGURE 5.13: Principle of the "Attosecond lighthouse" technique. The different spectral components are slightly spread spatially at focus. Joining the equivalent extrema of the field shows a wavefront that is progressively tilted as time advances.

5.4.3 Sources with a spatial spreading

To finish this little exploration of unconventional light sources, it is enlightening to present the so-called "attosecond lighthouse" approach. Here, a single short laser beam is used (no longer than 10 fs). But instead of making one's best to prepare a perfect laser with perfect flat phase front at focus, on the contrary, one inserts two wedges in the beam right before the focusing stage, the second being tilted (Fig. 5.13). The effect of these prisms is to spread continuously the different spectral components of the driving laser at focus. The result is a wavefront that remains flat, but is progressively tilted for successive half cycles of the laser (Fig. 5.13).

[1] The latter, called MAZEL-TOV, relies on a different interpretation, based on a subcycle shaping of the field forming a 3-foil. It uses two harmonics wavelengths. The interpretation is less straightforward and this is why we did not presented it. However, it is currently more popular to generate circularly polarized harmonics.

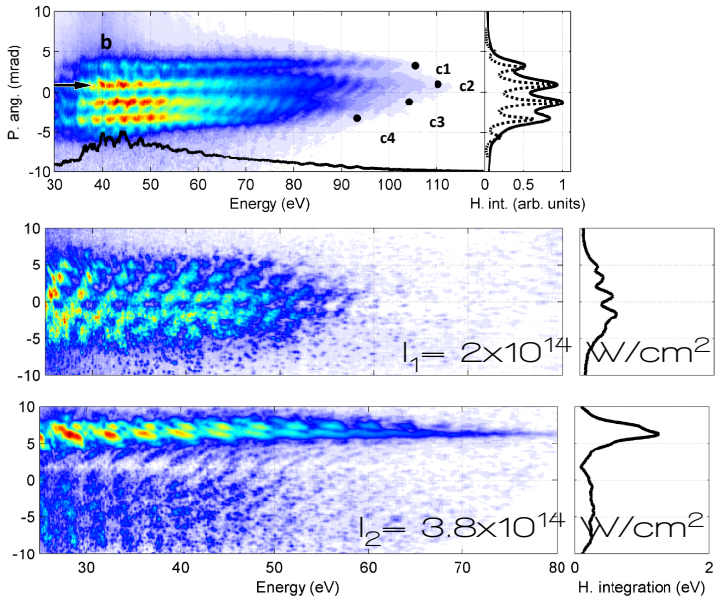

FIGURE 5.14: Spectra obtained when a wavefront rotation is set at the focus of the generating laser. Abcissa is the energy, vertical axis is the harmonic divergence. (top) Generation in neon, 7 fs laser, many shots average. (middle) Generation in N2, single shot, fairly low intensity. (bottom) Generation in N2, single shot, about the saturation intensity. Adapted from Kim et al. [2013].

The duality microscopic response/macroscopic response of HHG is beautifully illustrated on this example. Each half cycle, the three step process occurs. We can guess a temporal cutoff law for instance, that will change from one half cycle to the next due to the change of peak intensity as the pulse progresses. On its hand, the macroscopic emission is favored along the normal to the wavefront, as phase matching conditions are firstly governed by the sum of the fundamental wave vector. We thus conclude that we should have several beamlets emitted at progressively changing angles, each of them carrying a signature of the current parameters of the microscopic response at its emission time. This is indeed what is observed in Fig. 5.14, top panel. We can see a series of horizontal quasi continuous spectra, whose cutoff progressively increases at time passes (from the bottom beamlet to the top one). It finally decreases towards the top, as the amplitude of the electric field of the pulse decreases. This technique holds promises to generate perfectly synchronized sets of attosecond pulses, which could be used to perform attosecond pump/attosecond probe experiments. It is also extremely promising as a diagnostic technique of HHG, resolving all half cycles.

As a second illustration, the middle and bottom panels in Fig. 5.14 give insights in another gating technique. The middle panel shows HHG in N_2 with a reasonably low intensity while the bottom panel shows the same with a much higher intensity. Clearly the spectrum changes: while in the middle panel one may observe 4-5 attosecond pulses, in the lower panel, just one is still visible. This is due to ionization that is much more rapid in the second case and quickly kills any attosecond emission after the first efficient cycle. Again, we see here the importance of phase matching and ionization level of the medium, that is able to kill or not attosecond emission. Interestingly, over-driving HHG here yields an isolated attosecond pulse. This is so called the “ionization gating” approach towards single attosecond pulses.

CHAPTER 6

CONCLUSION

Laser progress

The availability and demand of stable and reliable sources of attosecond pulses is ever increasing around the world. In parallel, their development remains a subject of intense research. If the physics of high harmonic generation is fairly well understood in simple cases, and their characterization getting more and more reliable, it still reveals unexpected features. This progress is partially driven by technological progress of high power laser technologies. Over the last decade the attosecond community has accompanied two crucial breakthroughs. First, Optical Parametric (Chirp Pulse) Amplifiers (OPA and OPCPA) have allowed to down convert popular Ti:Sapphire lasers oscillating at λ=800 nm, to the MidIR range, in the λ=1-4 μm range, with significant efficiency and output power. Second, the maturity of doped fiber lasers, in particular Ytterbium doped Fiber Lasers (YDFL), and thin-disk lasers have increased the average power available. While it is limited to 20-40 W for Ti:Sapphire, it may reach a few hundred watts with this new technology. The tendency is to split this total power within more frequent pulses. Thus, while Ti:Sapphire have a repetition rate of a few 10's of Hz to 10kHz with pulse energies of 100 mJ down to 2 mJ, the new generation of doped fiber lasers reaches 100 kHz to MHz, with pulse energies of 1 mJ to 100μJ. The YDFL has a central wavelength λ=1.03 μm. The price to pay with this technology is thus less energy per pulse, but also a longer duration of the pulses (150 fs - few ps), the latter being coped with by a post-compression downstream through propagation in a gas-filled fiber. These lasers can also serve as a pump for OPCPA and OPA's, thus offering MidIR sources with a high repetition rate.

Attosecond sources developments

These laser developments have fed a race towards "very" high harmonics, lying in the few hundred eV range. Indeed the cutoff law indicates a scaling with λ^2. A factor of 4 on the wavelength (from λ=800 nm to λ=3200 nm) should thus extend the cutoff by a factor of 16 for the same peak intensity. Nowadays, in a few laboratories, sources extending well within the water window, i.e. 270-545 eV, are becoming available. In this range, photons are not absorbed by Oxygen, but are by Carbon, making organic targets in water possible objects of investigation. With specific schemes, keV energies were even reached.

As the energy per pulse of these new lasers is reduced, the geometry of HHG has to be adapted, and a stronger focusing is required to reach I_{sat}. HHG in strong focusing conditions is a matter of intense investigations, to design very dense and short targets (in comparison to the Rayleigh length), but also to control phase matching. In particular, as the wavelength increases, so does the excursion time, and the spread of the recombination times. In other words, the α atomic constant gets huge and phase matching not trivial to handle. The change of wavelength also raises specific questions to optimize the yield of HHG, as it scales as $\simeq 1/\lambda^7$. Their characterization and handling over such a large spectral range is nothing easy. For instance, usual spectrometers do not have the resolution to see harmonic structures spaced by 0.8 eV over 100's of eV, and most of the published spectra look continuous in this region, while they should not! All these aspects are intensively investigated currently.

Besides, this reduced energy and extended wavelength was found to be extremely valuable for HHG in solids, and in particular in crystals. Some fairly high order harmonics were generated and the 3-step model adapted to targets with a band structure and anisotropies. At this point, we should remark that starting with a λ=3200 nm laser, the photon energy is 0.39 eV, and its 11th harmonic is about λ=280 nm, i.e. in the UV range. It should be kept in mind that harmonic numbers are no longer a good indication that the spectrum extends far in the XUV, where attosecond pulses can be generated. However, continuous progress is observed towards higher photon energies from HHG in solids.

Not directly linked to progress of laser technology, we could also mention a recent trend towards more and more control on the polarization state of the harmonics emitted. In particular, beams highly circularly polarized are becoming available. But more exotic beams were also lately produced, for instance carrying an Orbital Angular Momentum, which shows an annular profile, or showing a structured radial polarization, or combination of both.

Finally, we can also observe a trend towards the establishment of mid-scale to large-scale facilities (e.g. ELI's infrastructures in Europe), which promises reliable and stable operation of sources of attosecond light pulse for applications.

Arising applications

As for applications, it would be endless to list them all. But while they were highly concentrated on simple gas samples initially, we observed lately a trend towards the investigations of i) more complex molecules with more than 25-20 atoms, and ii) solid

targets.

For molecules, the idea is to be able to follow the electronic dynamics initiated by either the removal of an electron by the XUV attosecond pulse, or by an IR excitation. In particular, this may influence the time the electron takes to escape (photoionization delay), but also the subsequent photoionization distributions, as measured in a VMIS or COLTRIMS. The monitoring of so-called charge migration in medium sized molecules is becoming a hot topic. At this point, it could be noticed that the more complex the molecule, the more complex the photoionization possibilities, and the more detailed should be the information retrieved from the detector. Progress in the stability of sources, together with higher repetition rate, is just making coincidence measurements accessible on attosecond sources, which should drive this trend. But generally speaking, a trend is to multiply the observations: photoionization diagrams in the molecular frame, transient absorption spectroscopy, dichroisms... The more complete the picture, the more chances to decipher electronic dynamics in the complex systems.

As for solid state applications, although the first experiments were carried out in the 2000's, the scene is less advanced. A few RABBITT/Streaking traces on solids where published, but photoemission investigations are mainly concentrated on the femtosecond regime up to now (See e.g. Rutherford/Artemis facility). In absorbance/reflection, the first demonstration of pump-dependent signal were published and some more interesting materials are now getting investigated with tailored attosecond sources (wavelength, polarization,...). In particular, a trend may be noticed towards the extension of visible multidimensionnal spectroscopy to the attosecond/XUV regime. Although still lagging being the gas phase community, the solid state physics community is rapidly adopting these sources that advantageously complement their more common Synchrotron or sometime FEL experiments.

A final word

With this list of recent developments and applications, we clearly understand that the attosecond community is very vivid and exponentially growing. Although not cheap (an installation probably costs around 2M€), it is a technology that remains reasonably accessible for a laboratory of a few persons, who can run it on their own. This may partially explain its expansion. This growth also means that newcomers specialize early. By writing this lecture, we both aimed at helping newcomers to make their first steps in the attosecond community, but also to give limited but sufficient information to those who are only becoming users of attosecond sources.

BIBLIOGRAPHY

Jason M. Eichenholz, Mingwei Li, Ian Read, Stefan Marzenell, Philippe Féru, Rich Boggy, and Jim Kafka. Future trends and applications of ultrafast laser technology. In Hanna J. Hoffman and Ramesh K. Shori, editors, *Solid State Lasers XV: Technology and Devices*. SPIE, feb 2006. doi: 10.1117/12.661032. 9

A. McPherson, G. Gibson, H. Jara, U. Johann, T. S. Luk, I. A. McIntyre, K. Boyer, and C. K. Rhodes. Studies of multiphoton production of vacuum-ultraviolet radiation in the rare gases. *J. Opt. Soc. Am. B*, **4**:595, 1987. 19

M. Ferray, A. L'Huillier, X. F. Li, G. Mainfray, and C. Manus. Multiple-harmonic conversion of 1064 nm radiation in rare gases. *J. Phys. B*, **21**:L31, 1988. 19

K. C. Kulander, K. J. Schafer, and J. L. Krause. Dynamics of short-pulse excitation, ionization and harmonic conversion. In Bernard Piraux, Anne L'Huillier, and Kazimierz Rzążewski, editors, *Super-Intense Laser-Atom Physics*, pages 95–110, Boston, MA, 1993. Springer US. ISBN 978-1-4615-7963-2. doi: 10.1007/978-1-4615-7963-2_10. URL https://doi.org/10.1007/978-1-4615-7963-2_10. 20

P. B. Corkum. Plasma perspective on strong-field multiphoton ionization. *Phys. Rev. Lett.*, **71**:1994, 1993. 20

M. Lewenstein, Ph. Balcou, M.Yu. Ivanov, A. L'Huillier, and P. B. Corkum. Theory of high-order harmonic generation by low-frequency laser fields. *Phys. Rev. A*, 49: 2117, 1994. 20, 32

M. Y. Kuchiev. Atomic antenna. *Soviet Journal of Experimental and Theoretical Physics Letters*, 45:404, April 1987. 20

Alexandra S. Landsman and Ursula Keller. Attosecond science and the tunnelling time problem. *Physics Reports*, 547:1–24, 2015. ISSN 0370-1573. doi: https://doi.org/10.1016/j.physrep.2014.09.002. URL http://www.sciencedirect.com/science/article/pii/S0370157314003159. 25, 26

Dror Shafir, Hadas Soifer, Barry D. Bruner, Michal Dagan, Yann Mairesse, Serguei Patchkovskii, Misha Yu. Ivanov, Olga Smirnova, and Nirit Dudovich. Resolving the

time when an electron exits a tunnelling barrier. *Nature*, 485(7398):343–346, may 2012. doi: 10.1038/nature11025. 25

Nicolas Camus, Enderalp Yakaboylu, Lutz Fechner, Michael Klaiber, Martin Laux, Yonghao Mi, Karen Z. Hatsagortsyan, Thomas Pfeifer, Christoph H. Keitel, and Robert Moshammer. Experimental evidence for quantum tunneling time. *Physical Review Letters*, 119(2), jul 2017. doi: 10.1103/physrevlett.119.023201. 25

Anatoli S Kheifets. The attoclock and the tunneling time debate. *Journal of Physics B: Atomic, Molecular and Optical Physics*, 53(7):072001, mar 2020. doi: 10.1088/1361-6455/ab6b3b. 26

L. D. Landau and L. M. Lifshitz. *Quantum Mechanics Non-Relativistic Theory, Third Edition: Volume 3*. Butterworth-Heinemann, 3 edition, January 1981. ISBN 0750635398. URL http://www.worldcat.org/isbn/0750635398. 27

A. M. Perelomov, V. S. Popov, and M. V. Terent'ev. Ionization of Atoms in an Alternating Electric Field. *Soviet Journal of Experimental and Theoretical Physics*, 23: 924, November 1966. 27, 29

MV Ammosov, NB Delone, and VP Krainov. Tunnel ionization of complex atoms and atomic ions in a varying electromagnetic-field. *Zhurnal Eksperimentalnoi i Teoreticheskoi Fiziki*, 91(6):2008–2013, dec 1986. ISSN 0044-4510. 27, 29

X. M. Tong, Z. X. Zhao, and C. D. Lin. Theory of molecular tunneling ionization. *Phys. Rev. A*, 66(3):033402, Sep 2002. doi: 10.1103/PhysRevA.66.033402. 27

X M Tong and C D Lin. Empirical formula for static field ionization rates of atoms and molecules by lasers in the barrier-suppression regime. *Journal of Physics B: Atomic, Molecular and Optical Physics*, 38(15):2593–2600, jul 2005. doi: 10.1088/0953-4075/38/15/001. 27

O. Smirnova and M. Ivanov. Multielectron High Harmonic Generation: simple man on a complex plane. *ArXiv e-prints*, April 2013. 32, 34

Norio Takemoto and Andreas Becker. Visualization and interpretation of attosecond electron dynamics in laser-driven hydrogen molecular ion using bohmian trajectories. *The Journal of Chemical Physics*, 134(7):074309, feb 2011. doi: 10.1063/1.3553178. 33

V. V. Strelkov, A. A. Gonoskov, I. A. Gonoskov, and M. Yu. Ryabikin. Origin for ellipticity of high-order harmonics generated in atomic gases and the sublaser-cycle evolution of harmonic polarization. *Physical Review Letters*, 107(4), jul 2011. doi: 10.1103/physrevlett.107.043902. 34

V. V. Strelkov, M. A. Khokhlova, A. A. Gonoskov, I. A. Gonoskov, and M. Yu. Ryabikin. High-order harmonic generation by atoms in an elliptically polarized laser field: Harmonic polarization properties and laser threshold ellipticity. *Physical Review A*, 86 (1), jul 2012. doi: 10.1103/physreva.86.013404. 34

V. V. Strelkov. Theory of high-order harmonic generation and attosecond pulse emission by a low-frequency elliptically polarized laser field. *Physical Review A*, 74(1), jul 2006. doi: 10.1103/physreva.74.013405. 34

E. Constant, D. Garzella, P. Breger, E. Mével, Ch. Dorrer, C. Le Blanc, F. Salin, and P. Agostini. Optimizing High Harmonic Generation in Absorbing Gases: Model and Experiment. *Phys. Rev. Lett.*, 82:1668, 1999. 45

M. Schultze, M. Fiess, N. Karpowicz, J. Gagnon, M. Korbman, M. Hofstetter, S. Neppl, A. L. Cavalieri, Y. Komninos, Th. Mercouris, C. A. Nicolaides, R. Pazourek, S. Nagele, J. Feist, J. Burgdorfer, A. M. Azzeer, R. Ernstorfer, R. Kienberger, U. Kleineberg, E. Goulielmakis, F. Krausz, and V. S. Yakovlev. Delay in photoemission. *Science*, 328(5986):1658–1662, 2010. doi: 10.1126/science.1189401. URL http://www.sciencemag.org/content/328/5986/1658.abstract. 57

M. Isinger, R. J. Squibb, D. Busto, S. Zhong, A. Harth, D. Kroon, S. Nandi, C. L. Arnold, M. Miranda, J. M. Dahlström, E. Lindroth, R. Feifel, M. Gisselbrecht, and A. L'Huillier. Photoionization in the time and frequency domain. *Science*, 358(6365): 893–896, nov 2017. doi: 10.1126/science.aao7043. 57

P. M. Paul, E. S. Toma, P. Breger, G. Mullot, F. Augé, Ph. Balcou, H. G. Muller, and P. Agostini. Observation of a Train of Attosecond Pulses from High Harmonic Generation. *Science*, **292**:1689, 2001. 59

M Schultze, E Goulielmakis, M Uiberacker, M Hofstetter, J Kim, D Kim, F Krausz, and U Kleineberg. Powerful 170-attosecond xuv pulses generated with few-cycle laser pulses and broadband multilayer optics. *New Journal of Physics*, 9(7):243, 2007. URL http://stacks.iop.org/1367-2630/9/i=7/a=243. 68

P. Johnsson, R. López-Martens, S. Kazamias, J. Mauritsson, C. Valentin, T. Remetter, K. Varjú, M. B. Gaarde, Y. Mairesse, H. Wabnitz, P. Salières, Ph. Balcou, K. J. Schafer, and A. L'Huillier. Attosecond Electron Wave Packet Dynamics in Strong Laser Fields. *Phys. Rev. Lett.*, 95:013001, 2005. 68

E. Goulielmakis, M. Schultze, M. Hofstetter, V. S. Yakovlev, J. Gagnon, M. Uiberacker, A. L. Aquila, E. M. Gullikson, D. T. Attwood, R. Kienberger, F. Krausz, and U. Kleineberg. Single-cycle nonlinear optics. *Science*, 320(5883):1614–1617, 2008. doi: 10.1126/science.1157846. URL http://www.sciencemag.org/cgi/content/abstract/320/5883/1614. 73

C Vozzi S Stagira G Sansone, E Benedetti and M Nisoli. Attosecond metrology in the few-optical-cycle regime. *New Journal of Physics*, 10(2):025006, 2008. 74

E. Gustafsson, T. Ruchon, M. Swoboda, T. Remetter, E. Pourtal, R. López-Martens, Ph. Balcou, and A. L'Huillier. Broadband attosecond pulse shaping. *Opt. Lett.*, 32(11):1353–1355, 2007. URL http://ol.osa.org/abstract.cfm?URI=ol-32-11-1353. 75, 76

R. López-Martens, K. Varjú, P. Johnsson, J. Mauritsson, Y. Mairesse, P. Salières, M. B. Gaarde, K. J. Schafer, A. Persson, S. Svanberg, C.-G. Wahlström, and A. L'Huillier. Amplitude and Phase Control of Attosecond Light Pulses. *Phys. Rev. Lett.*, 94: 033001, 2005. 76

C. Bourassin-Bouchet, Z. Diveki, S. de Rossi, E. English, E. Meltchakov, O. Gobert, D. Guénot, B. Carré, F. Delmotte, P. Salières, and T. Ruchon. Control of the attosecond synchronization of xuv radiation with phase-optimized mirrors. *Opt Express*, 19(4):3809–3817, Feb 2011. doi: 10.1364/OE.19.003809. URL http://www.opticsexpress.org/abstract.cfm?URI=oe-19-4-3809. 77

Jennifer L. Ellis, Kevin M. Dorney, Charles G. Durfee, Carlos Hernández-García, Franklin Dollar, Christopher A. Mancuso, Tingting Fan, Dmitriy Zusin, Christian Gentry, Patrik Grychtol, Henry C. Kapteyn, Margaret M. Murnane, and Daniel D. Hickstein. Phase matching of noncollinear sum and difference frequency high harmonic generation above and below the critical ionization level. *Optics Express*, 25 (9):10126, apr 2017. doi: 10.1364/oe.25.010126. 81, 82

K. T. Kim, C. Zhang, T. Ruchon, J.-F. Hergott, T. Auguste, D. M. Villeneuve, P. B. Corkum, and F. Quéré. Photonic streaking of attosecond pulse trains. *Nature Photonics*, 7:651–656, August 2013. doi: 10.1038/nphoton.2013.170. 83